JANUARY 2020

Ph.D. in Engineering Physics

UYGAR ŞAŞMAZ

REPUBLIC OF TURKEY

GAZİANTEP UNIVERSITY

GRADUATE SCHOOL OF NATURAL & APPLIED SCIENCES

MEASUREMENT OF THE INCLUSIVE PRODUCTION OF THE D^{*0}(2007) MESON IN HADRONIC Z DECAYS WITH THE ALEPH DETECTOR AT THE LEP COLLIDER

Ph.D. THESIS

IN

ENGINEERING PHYSICS

BY

UYGAR ŞAŞMAZ

JANUARY 2020

MEASUREMENT OF THE INCLUSIVE PRODUCTION OF THE D^{*0}(2007) MESON IN HADRONIC Z DECAYS WITH THE ALEPH DETECTOR AT THE LEP COLLIDER

Ph.D. Thesis
in
Engineering Physics
Gaziantep University

Supervisor
Prof. Dr. Ahmet BİNGÜL

Co-Supervisor
Asst. Prof. Dr. Andrew BEDDALL

by

Uygar ŞAŞMAZ

January 2020

© 2020 [Uygar ŞAŞMAZ]

REPUBLIC OF TURKEY
GAZİANTEP UNIVERSITY
GRADUATE SCHOOL OF NATURAL & APPLIED SCIENCES
ENGINEERING PHYSICS

Name of the Thesis	:	Measurement of The Inclusive Production of The D^{*0}(2007) Meson in Hadronic Z Decays with The Aleph Detector at The LEP Collider
Name of the Student	:	Uygar ŞAŞMAZ
Exam Date	:	31.01.2020

Approval of the Graduate School of Natural and Applied Sciences.

Prof. Dr. A. Necmeddin YAZICI
Director

I certify that this thesis satisfies all the requirements as a thesis for the degree of Doctor of Philosophy.

Prof. Dr. Ramazan KOÇ
Head of Department

This is to certify that we have read this thesis and that in our opinion it is fully adequate, in scope and quality, as a thesis for the degree of Doctor of Philosophy.

Asst. Prof. Dr. Andrew BEDDALL
Co-Supervisor

Prof. Dr. Ahmet BİNGÜL
Supervisor

Examining Committee Members:	Signature
Prof. Dr. Hüsnü AKSAKAL	....
Assoc. Prof. Dr. Sertaç ÖZTÜRK	....
Assoc. Prof. Dr. Mustafa YILMAZ	....
Prof. Dr. Ayda BEDDALL	....
Prof. Dr. Ahmet BİNGÜL	....

I hereby declare that all information in this document has been obtained and presented in accordance with academic rules and ethical conduct. I also declare that, as required by these rules and conduct, I have fully cited and referenced all material and results that are not original to this work.

Uygar ŞAŞMAZ

ABSTRACT

MEASUREMENT OF THE INCLUSIVE PRODUCTION OF THE D*^{0}(2007) MESON IN HADRONIC Z DECAYS WITH THE ALEPH DETECTOR AT THE LEP COLLIDER

ŞAŞMAZ, Uygar
Ph.D. in Engineering Physics
Supervisor: Prof. Dr. Ahmet BİNGÜL
Co-Supervisor: Asst. Prof. Dr. Andrew BEDDALL
January 2020
119 pages

A measurement of the inclusive production rate of the charmed $D^{*0}(2007)$ meson in hadronic Z decays is performed using data from the ALEPH detector at the LEP collider. A total of 3,239,746 hadronic events are selected from data recorded by ALEPH from the 1991 to 1995 running periods. Decays of $D^{*0} \rightarrow D^0\pi^0$ are reconstructed for $x_E \geq 0.3$ where $x_E = E_{D^{*0}}/E_{beam}$. The average D^{*0} multiplicity per hadronic event is evaluated to be:

$$\langle N_{D^{*0}} \rangle = 0.289 \pm 0.031 \pm 0.067 \pm 0.009$$

where the first error is statistical and the second is systematic. The third error is from the extrapolation to $x_E = 0$. The rates and differential cross-sections are compared with Monte Carlo model predictions. The signal significance is improved explicitly by applying machine learning algorithms based on Multi Variate classification methods of artificial intelligence applications.

Key Words: D*^{0} Production Rate, ALEPH, LEP, Hadronic Z Decays, TMVA, Artificial Intelligence, Machine Learning, Boosted Decision Trees

ÖZET

LEP ÇARPIŞTIRICISI ÜZERİNDEKİ ALEPH DEDEKTÖRÜNDE, HADRONİK Z BOZUNUMLARINDAKİ D*0(2007) MEZONU ÖLÇÜMÜ

ŞAŞMAZ, Uygar
Doktora Tezi, Fizik Mühendisliği
Danışman: Prof. Dr. Ahmet BİNGÜL
İkinci Danışman: Dr. Öğr. Üyesi Andrew BEDDALL
Ocak 2020
119 sayfa

LEP çarpıştırıcısı üzerindeki ALEPH dedektörü verileri kullanılarak, hadronik Z bozunumlarındaki cazibe kuark içeren $D^{*0}(2007)$ mezonunun üretim hızı ölçümleri yapılmıştır. ALEPH dedektörü ile 1991 ve 1995 yılları arasında kaydedilmiş veri-lerden, toplamda 3,239,746 hadronik olay seçilmiştir. $D^{*0} \rightarrow D^0\pi^0$ bozunumları $x_E \geq 0.3$ olacak şekilde imar edilmiştir. Burada, $x_E = E_{D^{*0}}/E_{demet}$ olarak alınmıştır. Hadronik olay başına ortalama D^{*0} mezonu bolluğu:

$$\langle N_{D^{*0}} \rangle = 0.289 \pm 0.031 \pm 0.067 \pm 0.009$$

olarak hesaplanmıştır. Buradaki birinci hata, istatistiksel, ikinci hata sistematik hatadır. Üçüncü ise $x_E = 0$ bölgesi için yapılan uzatma işleminden gelen hatadır. Üretim hızı ve diferansiyel tesir kesiti ölçümleri, Monte Carlo tahminleri ile karşılaştırılmıştır. Çoklu değişken sınıflandırma analinize dayanan yapay zeka uygulamalarından makina öğrenimi algoritmalarının, sinyal saflığında bariz bir biçimde iyileşme sağladığı tespit edilmiştir.

Anahtar Kelimeler: D*0 Üretim oranı, ALEPH, LEP, Hadronik Z Bozunumu, TMVA, Yapay Zeka, Makina Öğrenimi, Karar Ağaçları

I dedicate this study to my family for being ceaselessly supportive.

ACKNOWLEDGEMENTS

I would like to express my greatest appreciation and thank to my supervisor Prof. Dr. Ahmet BİNGÜL for being not only a tremendous mentor, but also a supportive acquaintance because of his ability to make me feel always powerful enough to achieve success.

My sincere thanks are for my co-supervisor Asst. Prof. Dr. Andrew BEDDALL for supporting and directing me for the unique achievements and success. I would like to extend my gratitude for Prof. Dr. Ayda BEDDALL for insightful constructive comments and providing me priceless opportunities.

I would also like to mention about my gratefulness to Prof. Dr. Serkant Ali ÇETİN for his immense reliance and precious guidance.

And finally, we wish to thank the ALEPH Collaboration for access to the archived data since the closure of the collaboration.

TABLE OF CONTENTS

LIST OF TABLES

LIST OF FIGURES

LIST OF SYMBOLS

γ	Photon
e^-	Electron
e^+	Positron
$K^\pm$	Kaon
$\pi^\pm$	Pion
π^0	Neutral Pion
μ	Muon
D^0	Neutral D-meson
$D^\pm$	D-meson
D^{*0}	Neutral excited D-meson
$D^{*\pm}$	Excited D-meson
σ	Cross-section
$\mathcal{E}$	Efficiency
$\mathcal{P}$	Purity

LIST OF ABBREVIATIONS

MC	Monte Carlo (simulation)
DA	Recorded Data (real)
LEP	Large Electron-Positron Collider
ALEPH	Apparatus for LEP pHysics
TMVA	ROOT Multi-Variate Analysis
MLP	Multilayer Perceptron
BDT	Boosted Decision Trees

CHAPTER 1

INTRODUCTION

In elementary particle physics, the standard model consists of quarks and leptons which interacts by the exchange of photons and intermediate vector bosons, as described by the Glashow-Weinberg-Salam standard model of weak interactions [1–3]. Additionally, quarks interact strongly as described by quantum chromodynamics (QCD) [4].

The area of interest for this analysis is the transformation of quarks and gluons into perceptible hadrons in high energy reactions. This transformation is governed by QCD which is predictive in high energy processes. However, the final stage of the transformation occurs at low energy, therefore phenomenological models are constructed to describe the hadronisation. Hence, cross-section measurements for the inclusive particle production improve the definition of the hadronisation process.

The Large Electron Positron Collider (LEP) provides a clean environment by the process $e^+e^- \to Z \to q\bar{q}$ with little contamination from background processes. The analysis presented here mainly focuses on inclusive particle production. Various particles have been measured in previous e^+e^- annihilation experiments and Monte Carlo programs have been tuned so that the measured rates were reproduced. A comprehensive compilation of experimental data on inclusive particle production in e^+e^- interactions can be found in [5].

In the area of resonant states, some progresses have been made since the construction of LEP as a Z boson factory. Compared to previous experiments, LEP obtained higher statistics as illustrated by the Figure 1.1, which shows larger hadronic cross-section than low energy colliders. Since 1989, ALEPH, DELPHI, L3 and OPAL experiments collected several million hadronic Z decays each.

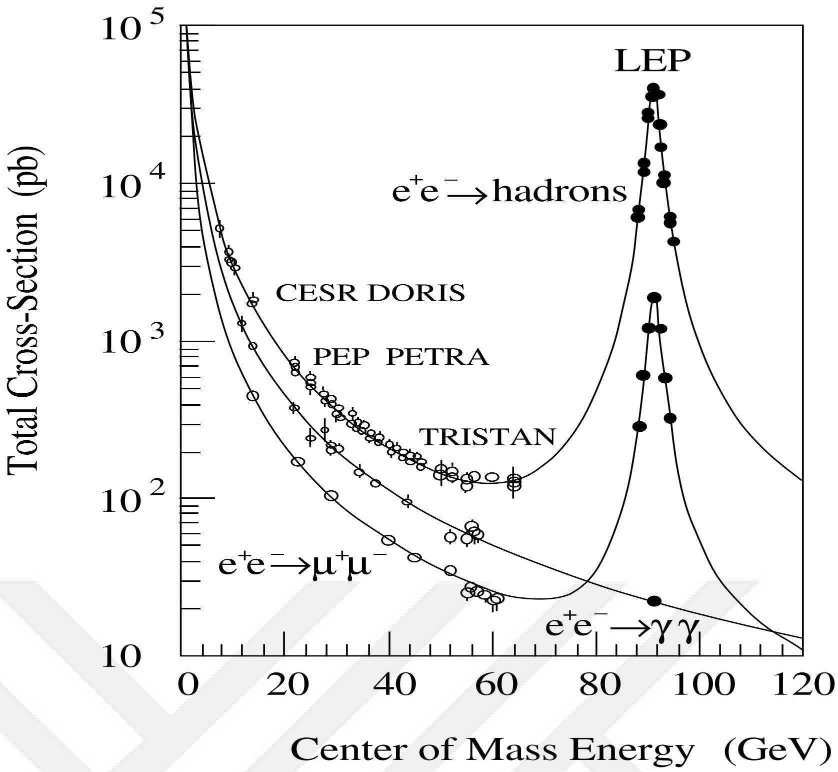

Figure 1.1 Total cross-section for e^+e^- annihilation into hadrons and muon pairs as function of the centre-of-mass energy. Also given is the two-photon cross-section. Experimental data are compared with predictions from the standard model.

This study presents the ALEPH measurement[1] of the measured rate and differential cross-section of the D^{*0} meson as a product in hadronic Z decays. Reconstruction of D^{*0} candidates is performed from the decay products $D^{*0} \rightarrow D^0\pi^0$, BR $= (64.7 \pm 0.9)\%$. The other decay channel $D^{*0} \rightarrow D^0\gamma$, BR $= (35.3 \pm 0.9)\%$, is also examined, however, its analysis is disclaimed because of the poorer signal significance.

The analysis described here is based on about 3 million selected hadronic events recorded by the ALEPH detector at center-of-mass energies about $\sqrt{s} = 91.2\,\text{GeV}$ in the running period of LEP between 1991 and 1995. Comparison of the results for the evaluated rates and the differential cross-sections with the Monte Carlo models Jetset 7.4, Pythia 8.2 and Herwig++ 2.6 are implemented.

This thesis includes a short summary of the Standard Model, a theoretical description of the fragmentation models and a brief information about

[1] See ref [6] for "Statement on the use of Aleph data for long-term analyses".

the experimental apparatus including the data acquisition system, event reconstruction, and detector simulation. The analysis is presented in Chapters 5 to 8, and the results with conclusions are given in Chapter 9.

CHAPTER 2

THEORY

2.1 The Standard Model

The Standard Model is an attempt to describe the fundamental particles and their interactions. The model is a quantum field theory that includes the unified weak and electromagnetic interactions (electroweak) and the strong interactions (quantum chromodynamics). Gravity has not yet been included in the Standard Model; however, in the quantum world of particle interactions the effects of gravity are insignificant.

In the Standard Model the most fundamental particles in nature are divided into two groups: fermions and bosons. The two groups are summarised in Table 2.1. The fundamental fermions are spin-$\frac{1}{2}$ particles providing the building blocks of all matter, whilst the interactions between the fermions are provided by the exchange of bosons (spin-1); the electromagnetic interaction is mediated by photons, the weak interaction by the W^+,W^- and Z bosons, and the strong interaction by gluons. In addition, a Higgs boson is required to provide mass for the fermions and the Z and $W^{\pm}$ bosons.

Fermions can be further divided into two sub-groups: leptons which interact via the electroweak interaction, and quarks which in addition interact via the strong interaction. The leptons consist of the electron, the muon, the tau, and their corresponding neutrinos. The quarks and leptons can be arranged into groups, according to their coupling to the weak current, forming three generations. The three rows of fermions in Table 2.1 represent each generation, each containing heavier particles than its predecessor.

Table 2.1 The particles and forces of the Standard Model.

Fermions (*spin* $-\frac{1}{2}$)				*Bosons* (*spin* 1)		
Quarks		*Leptons*		*em.*	*Weak*	*Strong*
u (*up*)	d (*down*)	e^-	ν_e	γ	$W^\pm$, Z	*gluons*(8)
c (*charm*)	s (*strange*)	μ^-	ν_μ			
t (*top*)	b (*bottom*)	τ^-	ν_τ			

In the early running periods of LEP, the number of generations of light neutrinos was confirmed to be three. Figure 2.1 shows for ALEPH data from 1990 and 1991 the measured hadronic cross-section around the Z resonance. The theoretical predictions for two, three, and four generations of light neutrinos are shown. The data are consistent only with the hypothesis of three generations. Combining the data from the four LEP experiments a recent value for the number of light neutrino generations is 2.994 ± 0.012 [7]. However, whilst all known neutrinos are believed to have zero or negligible mass, the measurements do not rule out a fourth generation neutrino of mass greater than $M_Z/2$.

2.2 Quantum Chromodynamics

QCD was formulated in analogy to QED as a gauge theory which describes strong interactions between quarks via exchange of massless gauge bosons, the 'gluons'. The six quark flavours (u, d, s, c, b and t) carry a quantum number called colour (red, green or blue). This is analogous to the electric charge in QED. Eight gauge bosons (the gluons) are introduced to mediate the strong interaction. An important difference between QED and QCD is that the gluons also carry the colour charge and can therefore couple directly to other gluons unlike the photons in QED which do not carry electric charge. A consequence is that strong coupling, α_s, is energy dependent. To first order, α_s is given by the equation:

$$\alpha_s(Q^2) = \frac{12\pi}{(33 - 2n_f)\ln(Q^2/\Lambda^2)} \qquad (2.1)$$

where Q^2 is the momentum transfer (on the Z peak $Q^2 = (91.2\,\mathrm{GeV})^2$), n_f is the available number of quark flavours ($n_f = 5$ at LEP), and Λ is a parameter determined by experiment. The strength of α_s therefore decreases for higher values of Q^2 (or alternatively very short interaction distances) leading to the property known as asymptotic freedom where the quarks and gluons behave like free particles. Conversely, for small values of Q^2 (large interaction distances) α_s

diverges. This can be considered as an explanation for quarks are not seen in the form of free particles.

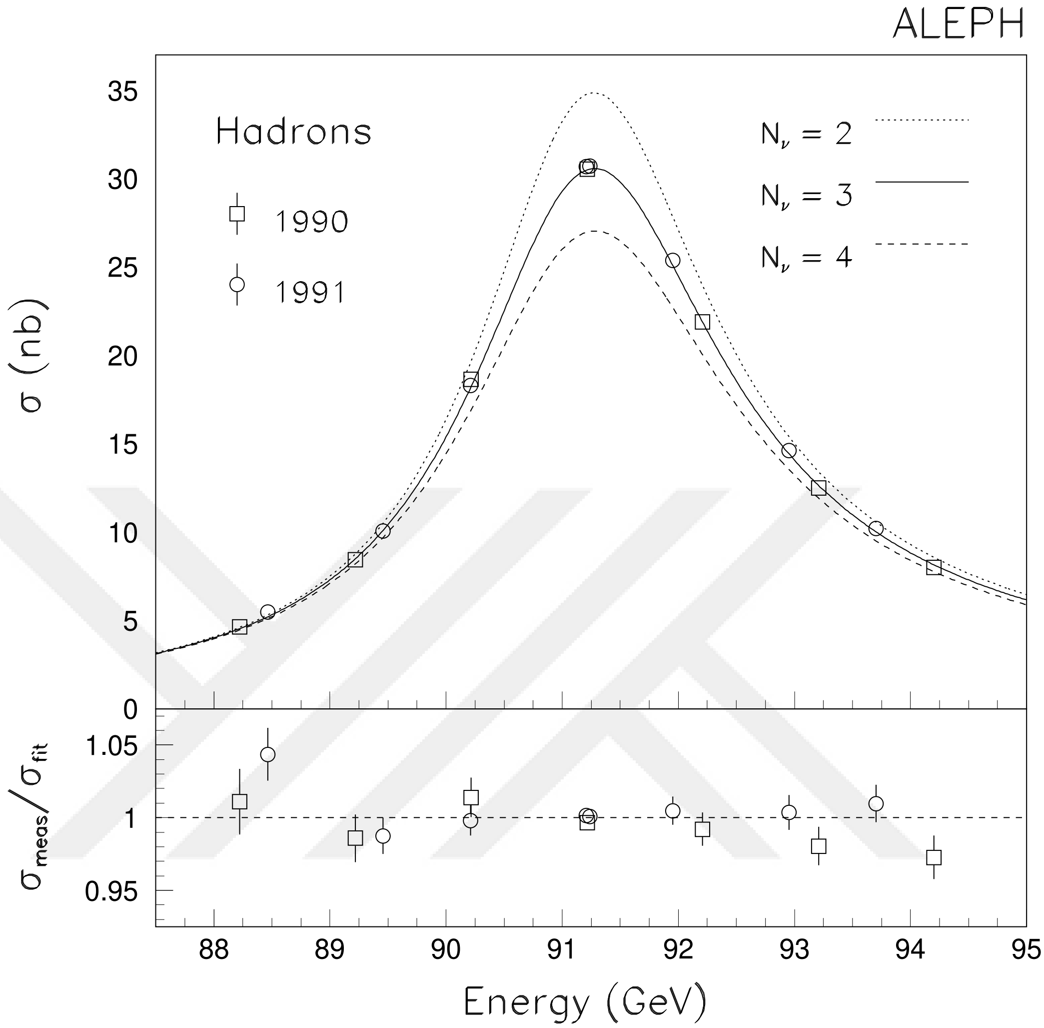

Figure 2.1 The hadronic cross-section as a function of the centre-of-mass energy. The theoretical predictions are shown for the cases of two, three, and four generations of light neutrinos. The data are consistent only with the hypothesis of three generations.

2.3 Hadron Production in Z Decays

Electron-positron annihilation at LEP energies results in the production of the Z boson which subsequently decays to a fermion-antifermion pair. The dominant decay mode is Z $\rightarrow q\bar{q}$ (branching ratio $= 69.91 \pm 0.06\%$ [7]), an illustration of the theoretical description of this reaction is shown in Figure 2.2. The development can be separated into four phases:

(1) Electroweak.

(2) Perturbative QCD.

(3) Hadronisation.

(4) Hadron decays.

The first phase describes the production of the initial hadronic partons, the remaining phases describe the fragmentation of these partons into the final state hadrons. These four phases are discussed below.

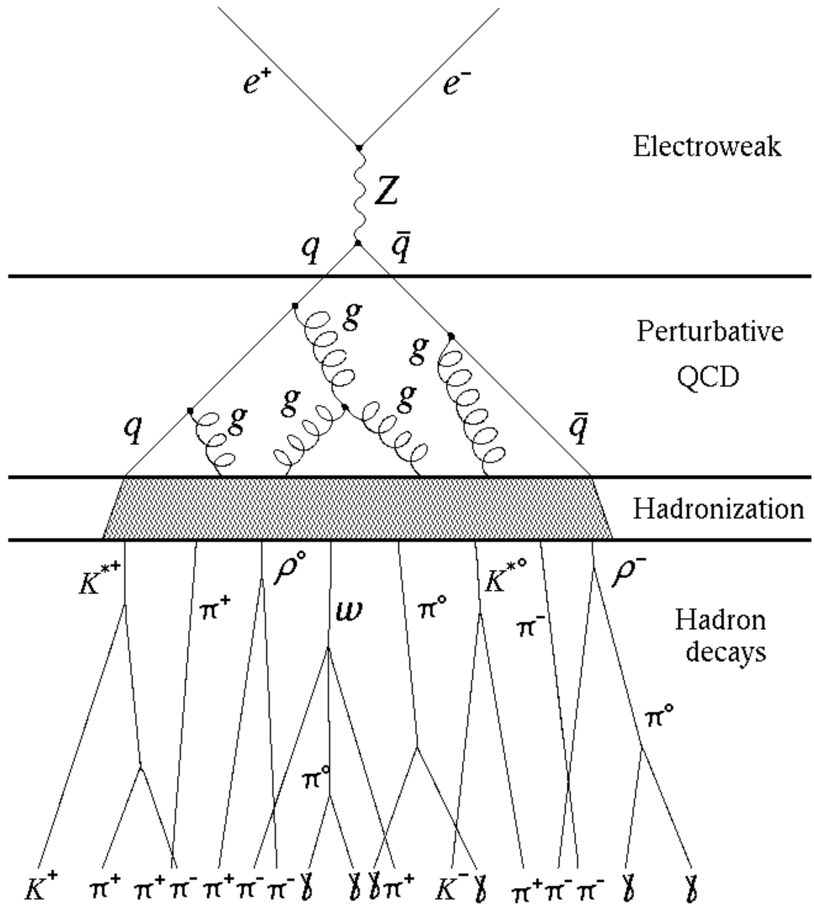

Figure 2.2 Schematic diagram of the reaction $e^+e^- \rightarrow Z \rightarrow q\bar{q}$. The development can be separated into four phases: electroweak, perturbative QCD, Hadronisation, and hadron decays.

2.3.1 The Electroweak Phase

The first phase involves the annihilation of an e^+e^- pair (with the possibility of an initial bremsstrahlung radiation) and the creation of a Z boson and its subsequent decay to a $q\bar{q}$ pair. This phase is described by the electroweak theory.

2.3.2 Perturbative QCD

The initial quark-antiquark pair move apart with a relative speed close to the speed of light, each parton having the beam energy of $\approx$ 45 GeV. These preliminary quarks radiate gluons, which can again radiate more gluons or can be divided into additional quark-antiquark pairs. The early evolution of this process can be described by perturbative QCD. In this phase, momentum transfers involved in the interactions are sufficiently large, giving rise to a small value for the strong coupling constant, for perturbation theory to be applicable. There are two approaches which can be used to model perturbative QCD: the 'matrix element' method, and the 'parton shower' method.

In the matrix elements method, available in the JETSET ME option of the Lund simulation [8], a fixed order QCD calculation is describing the perturbative phase by producing partonic latest states according to the exact elements of QCD matrix. Models of this profits that interference effects are considered properly, and that α_s is well defined. However, as the models only use calculations of the matrix elements to $O(\alpha_s^2)$, only eventual states between 2 and 4 partons can be produced. At PEP/PETRA energies, models of the matrix element are performing intimately. However, at LEP energies these do not generate final states with high enough parton multiplicity, resulting in an inability to simultaneously reproduce correctly both 3 and 4-jet rates.

In the parton shower approach the leading terms of the perturbation expansion are summed to all orders. These leading (logarithmic) terms are enhanced and correspond to infra-red or collinear parton emission. Parton shower algorithms are based upon an iterative use of the basic branchings $q \to qg$, $g \to gg$ and $g \to q\bar{q}$. Generally a primary 2, 3 or 4-parton final state is generated using the second order matrix element approach. The configuration is then allowed to shower in a tree-like fashion according to the various probabilities of the branchings given above. The process continues until the evolution variable reaches a predefined cut-off.

It is a general property of the popular shower algorithms that they produce 'coherent' showers. This is achieved, for example, by angular ordering the radiated partons such that the production angle of each parton is never more than the production angle of the radiated parton which preceded it. This angular ordering has a phenomenological implication since it can predict that the energy flow in the shower remains collimated around the direction of the initial partons. This explains why most hadronic Z decays exhibit a pronounced 2-jet structure. Furthermore, if in the initial stage of the parton shower a hard gluon is emitted at a large angle, it gives rise to a well separated jet.

The weakness of the parton shower approach, however, is that because it sums only the leading-log terms in the expansion it is limited in its predictions for wide-angle parton emission. In this case, the matrix element method is more suitable.

2.3.3 Hadronisation

Towards the end of the parton shower, the momentum transfer Q^2 becomes small and therefore the strong coupling constant becomes large rendering the predictions of perturbative QCD invalid. To model the final phase of fragmentation, i.e. the transformation of the partons into colourless hadrons (hadronisation), phenomenological models implemented as Monte Carlo programs are used. Three main models exist: independent hadronisation, string hadronisation, and cluster hadronisation. The latter two models are implemented in the JETSET and HERWIG programs respectively, and are used in the analysis presented in this thesis. The three models are described below.

Independent Hadronisation

One of the first models of the hadronisation process was the independent fragmentation model introduced in 1977 by R.D.Field and R.P.Feynman [9]. In this model, each original quark and antiquark independently transform into a jet of hadrons in the following way:

$$\begin{aligned} q_0 &\rightarrow h(q_0, \bar{q}_1) + q_1 \\ q_1 &\rightarrow h(q_1, \bar{q}_2) + q_2 \\ q_2 &\rightarrow etc., \end{aligned} \tag{2.2}$$

where q_0 is the quark from the original quark-antiquark pair. This process is illustrated in Figure 2.3. A new quark-antiquark pair $(q_1, \bar{q}_1)$ is created in the colour field of q_0 (from the vacuum) which results in q_0 and $\bar{q}_1$ combining to form a hadron $h(q_0, \bar{q}_1)$. The remaining quark q_1, which has less energy than q_0, then goes on to initiate another quark-antiquark creation $(q_2, \bar{q}_2)$ from which another hadron is formed. This process of $q \rightarrow q + hadron$ is repeated until the remaining quark has insufficient energy to form a hadron.

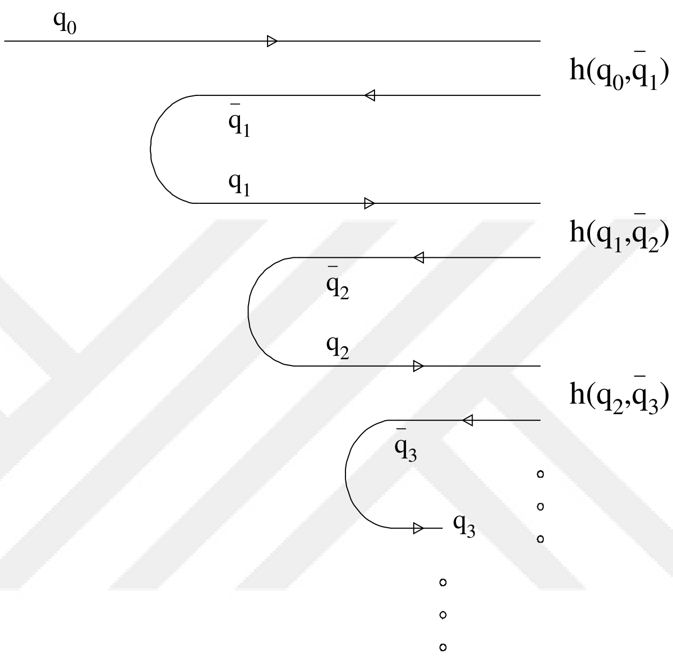

Figure 2.3 Hadron production in the Field-Feynman model.

The model involves one arbitrary function $f(\eta)$ which gives the probability that the hadron containing the original quark leaves the remaining jet a fraction η of its momentum. This ultimately determines the momentum distributions of the hadrons. Field and Feynman chose $f(\eta)$ to be of the form:

$$f(\eta) = 1 - a + 3a\eta^2 \tag{2.3}$$

where the parameter a is determined from experiment. It is assumed that this function applies to all iterations of the cascade.

In addition, three other parameters are required to determine the properties of the quark jets.

(1) The ratio of the production of strange quark to up or down quarks: Field

and Feynman assumed the quark flavours u, d and s to be produced in the ratios 2 : 2 : 1, i.e., strange quark production is suppressed due to the larger mass of the s quark.

(2) The spin of the primary mesons: Qualitatively one expects, from spin counting, the ratio of pseudoscalar to vector meson production to be 1:3 multiplied by some factor which disfavours heavier states. However, due to uncertainties in the knowledge of the quark masses the ratio cannot be calculated. Experimentally the ratio is typically one, and so in the model the two spin states are generated with equal probability.

(3) The mean transverse momentum given to the primary mesons: This is determined by requiring that the final hadrons (after decay) have a mean transverse momentum of about 330 MeV/c, to coincide with experimental observations.

To enable the production of baryons, an extension to the model was proposed by Meyer [10], in which it is assumed that occasionally two quark-antiquark pairs, instead of one, are produced from the vacuum. The quarks and antiquarks then align to form baryon-antibaryon pairs.

Although the Field-Feynman model does a reasonable job of parameterising experimental results, a number of problems prevent it from being regarded as a true theory of hadronisation. For example, the model is based on the cascade of a quark jet and so it is not obvious how one should model the cascade of a gluon jet, this is important at LEP energies where multi-jet events are a common occurrence. Also, at the end of the cascade there is always one quark and one antiquark left over, with no simple way of combining them together to form a hadron. This introduces problems with colour and energy-momentum conservation.

The Field-Feynman model has been surpassed by models with a stronger theoretical basis, two of which are the 'string model' and the 'cluster model'. A schematic illustration of these two models are given in Figure 2.4.

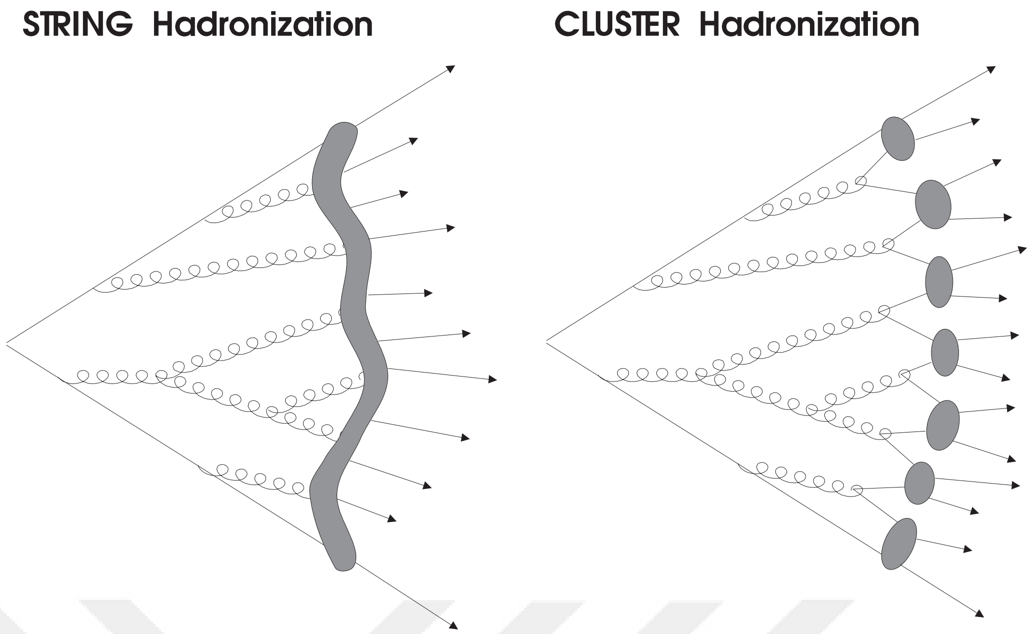

Figure 2.4 Schematic representation of the string and the cluster hadronisation models.

String Hadronisation

In the string model, hadron production is described in terms of the break-up of a one-dimensional relativistic string. This picture is motivated by the observation that due to the gluon self-coupling, the field lines of a static colour field attract each other to form a flux tube with a transverse dimension of $\sim 1\,\text{fm}$. This can be compared to the electromagnetic case in which the field lines spread out to infinity; the two cases are illustrated in in Figure 2.5. The flux tube picture is the basis for the Lund model [11].

If the tube is assumed to be uniform along its length, then this leads to a linearly rising potential and so the QCD potential grows linearly at large distances. Such large distance behaviour is supported by lattice calculations and provides a natural explanation for quark confinement.

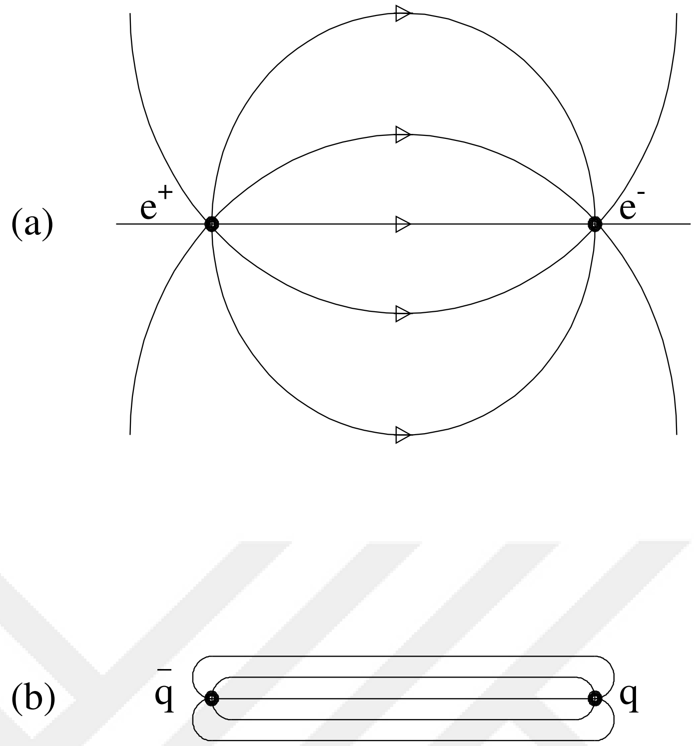

Figure 2.5 (a) The electric field lines between an electron and positron, spreading out to infinity. (b) The colour field lines between a quark and antiquark, confined in a narrow flux tube with a transverse dimension of $\sim 1\,\mathrm{fm}$.

In this string model the string is stretched between the original $q\bar{q}$ pair. As the partons move apart, the potential energy in the string increases until it breaks by the production of a new $q'\bar{q}'$ pair splitting the system into two colour-singlet systems $q\bar{q}'$ and $q'\bar{q}$. At large enough energies further breaks of the daughter-strings occur until only on-shell hadrons remain, each hadron corresponding to a small piece of string, with a quark at one end and an antiquark at the other. In this picture, gluons, having the colour structure of a quark-antiquark state, act as kinks in the original string often producing (at LEP energies) independent jets of hadrons clearly separated from the original quark and anti-quark jets.

In the Lund Monte Carlo, the $q'\bar{q}'$ pairs are generated using the idea of quantum mechanical tunnelling. This picture leads to a suppression of heavy-quark production, $u : d : s : c \approx 1 : 1 : 0.3 : 10^{-11}$. Therefore, charm (and heavier quarks) are not expected to be produced in the soft hadronisation, but only in perturbative parton shower branchings ($g \rightarrow q\bar{q}$) or in the original Z decay. Due to the uncertainty in the quark masses the suppression of $s\bar{s}$ production is left as a free parameter. As in the Field and Feynman model, vector mesons and pseudoscalar mesons are generated with equal probability, but, the ratio is left as an adjustable parameter for future tuning.

A tunnelling mechanism can also be used to explain the production of baryons. It is assumed that a break in the string can be caused by creation of a diquark-antidiquark pair. A suppression of baryon production comes from the assumption that the diquark mass is larger than the mass of a quark. However, the production of baryons still remains one of the least well understood aspects of particle production.

A spin-off of the Lund scheme has been proposed by the UCLA group [12]. In this model, all suppression of heavy hadron production enters through the hadron mass and so does not require the 'quark parameters' used in the Lund model, such as the s/u ratio. Spin counting is taken care of automatically by Clebsch-Gordan coefficients and no separate parameter for the relative production rates of vectors and pseudoscalars is introduced. The advantage of this model over Lund is therefore a reduction in the number of free parameters.

Cluster Hadronisation

In the cluster hadronisation model, the shower from the perturbative phase is stopped when the parton virtuality falls below some cut-off, $t_0 \approx 0.7\,\mathrm{GeV}$. Gluons are then split into quark-antiquark pairs. Colorless pairs of quarks which are close in phase then produces massive clusters which decay isotropically into hadrons that are visible. The fundamental parameters in this model are the virtuality cut-off, t_0, and the QCD scale parameter, Λ, which determines the scale of α_s (Equation 2.1).

In the framework of Herwig, the hadronisation process is as follows. A cluster C with flavour composition $(q_a, \bar{q}_b)$ and mass M_C is decayed into two hadrons h_1 and h_2 with flavours $(q_a, \bar{q}_r)$ and $(q_r, \bar{q}_b)$:

$$C(q_a, \bar{q}_b) \rightarrow h_1(q_a, \bar{q}_r) + h_2(q_r, \bar{q}_b) \tag{2.4}$$

The quark (or diquark) flavour 'q_r' is selected randomly, and with equal probability, from the possibilities d, u, s, c, b with the condition that

$$M_C > [m(q_a, \bar{q}_r)]_{lightest} + [m(q_r, \bar{q}_b)]_{lightest} \tag{2.5}$$

where $[m(q_i, \bar{q}_j)]_{lightest}$ is the mass of the lightest hadron in the model that has flavour composition $(q_i, \bar{q}_j)$.

The decay daughters, h_1 and h_2, are selected randomly from a list of hadrons which have the correct quark content, with a probability proportional to their spin degeneracy. For example, an a_2^+ (spin 2) is five times more likely to be selected than a π^+ (spin 0), should the flavour composition be $(u, \bar{d})$. If the sum of the masses h_1 and h_2 is greater than the mass of the decaying cluster then the combination is rejected and another selection made with the above criteria. If accepted, the common 3-momentum p_{cm} of the two daughters in the rest frame of the cluster parent is evaluated. The final probability to select a given pair of hadrons is then proportional to the phase space weight W_{decay} given by

$$W_{decay} = p_{cm} \times (2S_1 + 1) \times (2S_2 + 1) \tag{2.6}$$

where S_1 and S_2 are the spin values of the two daughters h_1 and h_2. W_{decay} then determines whether the cluster decay $C \to h_1 + h_2$ is accepted or not. In the case of rejection, the process is started again with the selection of a new quark or diquark flavour. If the decay channel is accepted, the daughters are decayed isotropically in the rest frame of the parent cluster.

The model assumes that the process of hadronisation is dominated by the clusters decaying into hadrons according to the available phase-space and the hadrons permitted. This means that phase space alone has to account for the relative production rates of mesons and their corresponding momentum distributions. For example, vector meson production is suppressed due the larger phase space available for the lower mass pseudoscalar mesons, similarly strange meson production is suppressed due to the larger mass of s quarks.

In addition to the fundamental parameters t_0 and Λ, two additional parameters are introduced for the treatment of very low and very high mass clusters: clusters with a mass above a cut-off value (default value = 3.65 GeV/c^2) are split into two clusters which are then allowed to decay isotropically into hadrons. Clusters with a very small mass are allowed to decay into a single hadron. Baryon production is achieved by introducing a probability that a gluon may branch into a diquark-antidiquark pair.

The LPHD Model

An alternative approach to the hadronisation process is taken in the Local Parton-Hadron Duality model (LPHD), where it is assumed that the properties on the parton level are closely related to the corresponding hadronic properties. This implies that certain quantities, such as inclusive distributions, may be studied without making reference to a hadronisation process.

This idea of a local parton-hadron duality has been developed in particular by the St. Petersburg group [13]. In an extreme interpretation, a one to one correspondence is assumed between partons and hadrons, event by event, with a suitable choice of partonic cut-off parameter, Q_0. A 'softer' interpretation, however, is usually favoured in which there is no absolute correspondence event by event, but only in the average behaviour and in the fluctuations around that average. A prediction of this model is that the average momentum of a particle species is dependent on the hadron mass. This is related to the fact that the cut-off, Q_0, in a parton shower is not expected to be constant but correlated to the final state hadronic mass. If the Q_0 is increased then the probability of further parton branching is reduced implying that a final state parton, in addition to having a larger effective mass, will have a greater momentum.

2.3.4 Hadron Decays

In the final phase, the primary hadrons are decayed according to measured branching ratios and lifetimes. In the versions of JETSET used in this analysis, the generators include improved bottom and charm decay tables. The particles visible at the detector level are mainly pions, most of which are the results of decays, the fraction of pions directly from hadronisation being relatively small. Conversely, the fraction of resonances originating directly from hadronisation is high, and therefore inclusive resonance studies provide information which is more closely related to the dynamics of the fragmenting partons. However, inclusive resonance distributions are sensitive to heavy flavour decay tables. The vector resonances are, in addition, sensitive to tensor production; tensors occupy phase-space which would otherwise be occupied by vectors.

In this thesis, the rate of production and the momentum distribution of the D^{*0} meson is studied, providing a test of the fragmentation process implemented in the JETSET, PYTHIA and HERWIG Monte Carlos.

CHAPTER 3

APPARATUS

3.1 Introduction

ALEPH is an abbreviation of Apparatus for LEP Physics. It was positioned with other four detectors around the collider LEP at CERN in Geneva, Switzerland [14]. LEP produced its first collisions in July 1989 and since then, millions of events have been recorded by the ALEPH particle detector. Its purpose was to explore the Standard Model of particle physics and search for manifestations of new physics. The ALEPH experiment was a large collaboration of several hundred physicists and engineers from 32 universities and national laboratories from around the world. The collaboration closed in 2004.

3.2 Large Electron-Positron Collider (LEP)

The experimental discovery of the neutral weak current in the early seventies verified the theoretical postulate of electroweak unification. In order to study the physics contained in this theoretical framework more precisely, the LEP collider was proposed, with its design parameters being more clearly defined after the discovery of the W and Z bosons by UA2 in 1983 [15, 16].

With a circumference of 27 km, the LEP collider at CERN is the largest e^+e^- collider ever built. LEP operated at the Z peak between 1989 and 1995 with e^+e^- collisions around the Z resonance (91.2 GeV center of mass) for the four LEP experiments ALEPH, DELPHI, L3 and OPAL, Figure 3.1. The collider was upgraded in 1995 and ran until 2000 in its second phase where the collision energy was doubled in order to produce pairs of on-shell $W^\pm$ bosons.

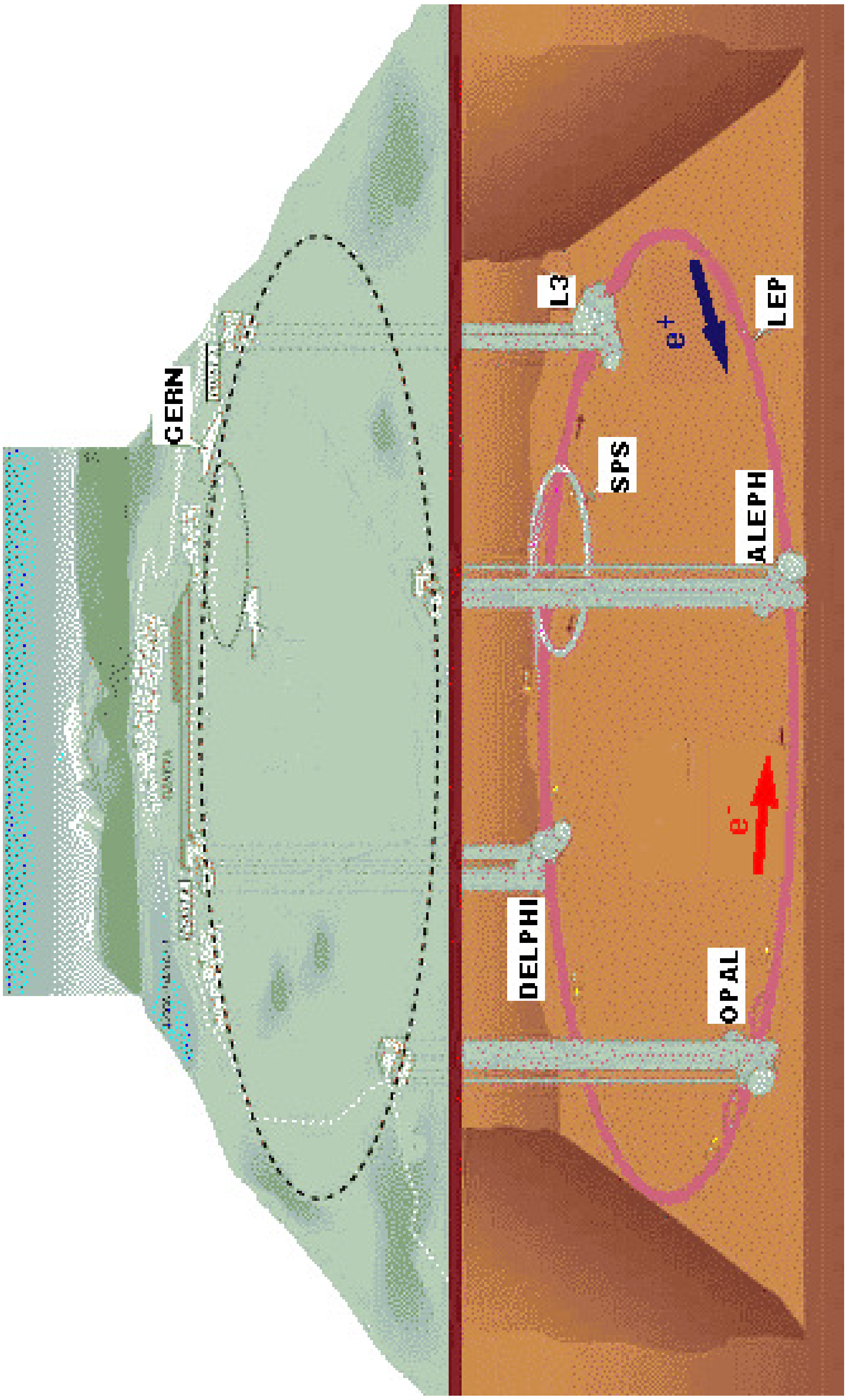

Figure 3.1 Schematic view of LEP and the four detectors described in the text. It has a circumference of 27 km and is located in an underground 3.8 m diameter tunnel at a depth varying between 50 m and 170 m.

The machine enclosed in a tunnel situated between 50 to 170 meters below ground. It consists of eight straight sections joined by eight arcs forming an octagon with rounded corners. Electrons and positrons orbited in bunches (each bunch containing $\sim 10^{12}$ particles) inside an evacuated beam pipe, the positrons orbiting clockwise (as viewed from above) and the electrons anticlockwise. The orbits are controlled by electromagnets; 1320 quadrupole and sextupole magnets focus the particles in all the sections, whilst 3392 dipoles bend the beams around the curved sections. The resultant energy loss due to synchrotron radiation is replaced by 128 copper radio frequency (RF) cavities positioned in the straight sections of LEP.

The large circumference of LEP was designed to keep the synchrotron radiation to a practical level, the rate of energy loss being inversely proportional to the radius of curvature. Under the circular acceleration, an electron emits synchrotron radiation, the energy radiated (power lost) per particle per turn being

$$P = \frac{4\pi}{3}\frac{e^2\beta^2\gamma^4}{r} \tag{3.1}$$

or expressing γ in terms of energy, E, and mass m, $\gamma = E/mc^2$

$$P = \frac{4\pi}{3}\frac{e^2\beta^2 E^4}{m^4c^8 r} \tag{3.2}$$

where r is the bending radius, β is the particle velocity, and $\gamma = (1-\beta^2)^{-1/2}$. The disadvantage of building large colliders is the very large cost; for this reason, larger circular e^+e^- colliders are not expected to be built in the future.

Originally there were 4 bunches of electrons and 4 bunches of positrons in circulation, this was increased to 8 bunches on 8 bunches in 1992, and finally running with bunch trains in 1995. In 8 bunch mode the two beams collide, at the center of each LEP detector, every $11\,\mu$s. The beams are focused by sextupoles, creating a luminous region (the beam spot) of length 18 mm (in the z-direction), and cross-section with $\sigma_x \approx 0.25$ mm, and $\sigma_y \approx 0.015$ mm (see Section 3.4.1 for a definition of the ALEPH coordinate system). The luminosity of LEP is $\sim 10^{32}\,\mathrm{cm}^{-2}\mathrm{s}^{-1}$, producing Z bosons at a rate of $\sim 1\,$Hz (on peak).

3.2.1 Beam Injection and Acceleration

For part of the injection system, LEP exploited existing CERN installations, namely the Proton Synchrotron (PS) and the Super Proton Synchrotron (SPS). Two purpose-built linear accelerators (linacs) were added to these to complete the injection system shown in Figure 3.2. Electrons (from an electron gun) and positrons (from a tungsten converter) are accelerated to 600 MeV by the LEP injection linac (LIL), and stored in the electron-positron accumulator (EPA).

Once a sufficient number of particles have been collected they are transferred to the PS and accelerated to 3.5 GeV. The particles are then injected into the SPS where they are accelerated to 20 GeV and finally injected into LEP. This cycle is repeated until enough particles have accumulated, thus completing the 'fill'. The electrons and positrons are then accelerated to collision energy by the RF cavities.

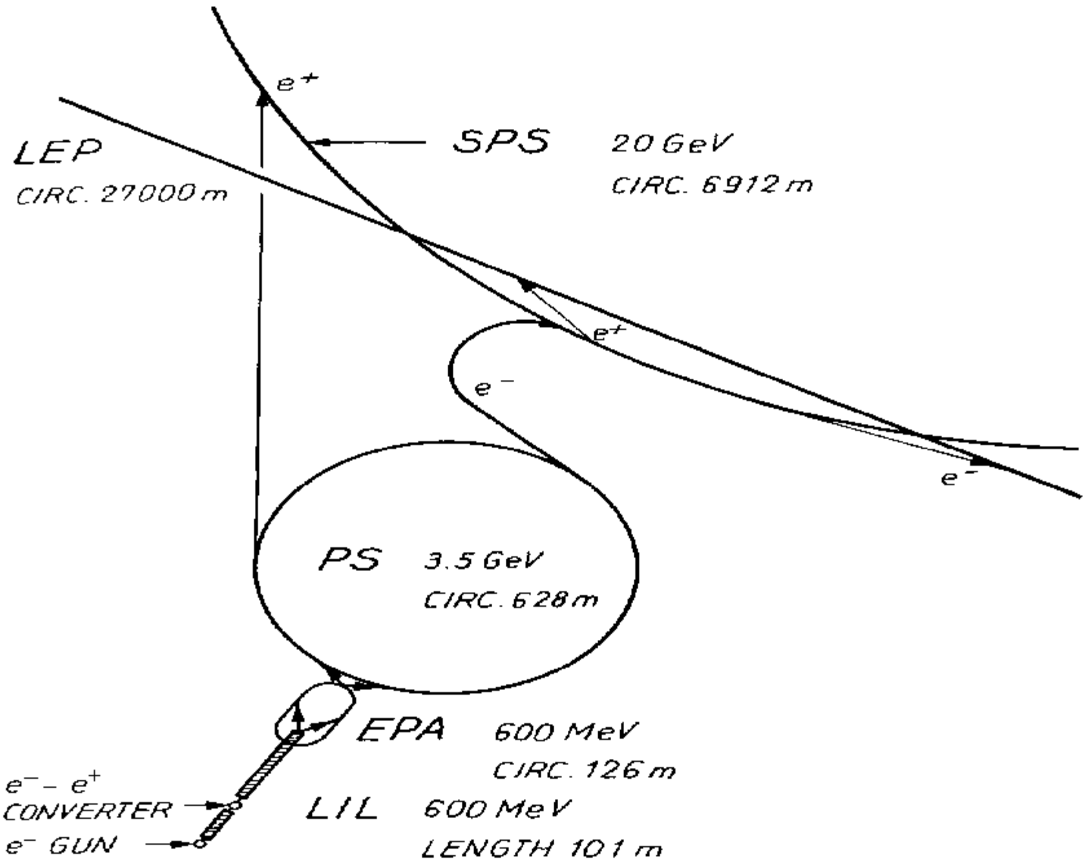

Figure 3.2 The LEP injection system.

3.3 Particle Detectors

The detectors employed in experiments in high-energy physics are required to record the position, arrival time, momentum (energy) and identity of charged and neutral particles. If we have an 'ideal' detector, we can reconstruct the interaction, ie. obtain all possible information on it. This is then compared to theoretical predictions and ultimately leads to a better understanding of the interaction/properties of particles. An ideal detector measures all produced particles, their energy, momentum and type (mass, charge, life time, spin, decays). Precise evaluation of position coordinates is required to determine the particle trajectory and, in particular, its momentum (from the deflection in a magnetic field); precise timing is often required in order to associate one particle with another from the same interaction, frequently in situations where the total interaction rate per unit time may be very high.

Neutral particles are detected through their decay (e.g., $K^0 \rightarrow \pi^+\pi^-$) and/or interaction with matter (e.g., $\pi^0 \rightarrow \gamma + \gamma, \gamma \rightarrow e^-e^+$), leading to secondary charged particles. Different particle types interact differently with matter (detector), e.g. photons do not feel a magnetic field. We need different types of detectors to measure different types of particles. Thus, there is no single detector to detect all kind of particles, so a combination of different detectors is employed. An example is the 'ALEPH' detector.

3.4 The ALEPH Detector

3.4.1 Overview

Figure 3.3 shows a schematic view of the ALEPH detector with the main subdetectors labelled.

ALEPH uses a cartesian coordinate system (x, y, z) or cylindrical coordinates (r, ϕ, z). In any case, the direction z is on the line of beam with the electron direction which is the positive direction of the axis. This direction points to the LEP center and the positive y axis direction is outlined as (x, y, z) which forms a right hand coordinate system.

The detector design purpose is measuring the momenta of particles. Another purpose can be defined as to measure the energy deposition in calorimeter by neutral and charged particles. Identifying the flavours of three lepton is another purpose of the detector. In addition, distance measurement of the short lived particles such as the b and c hadrons and τ lepton can be measured.

Special significance is given to resolution of momentum up to the greatest energies, via large tracker system with 1.5 T magnetic field, and to identification of electron, refers to a segmented, electromagnetic calorimeter, and so as measurement of ionisation taking place in the tracker. Additionally, identification of muon is implemented with tracking inside iron absorber in order to eliminate the hadrons. Hadron (π, K, p) identification was not given point to but it was enough for some analyses given in examples [17].

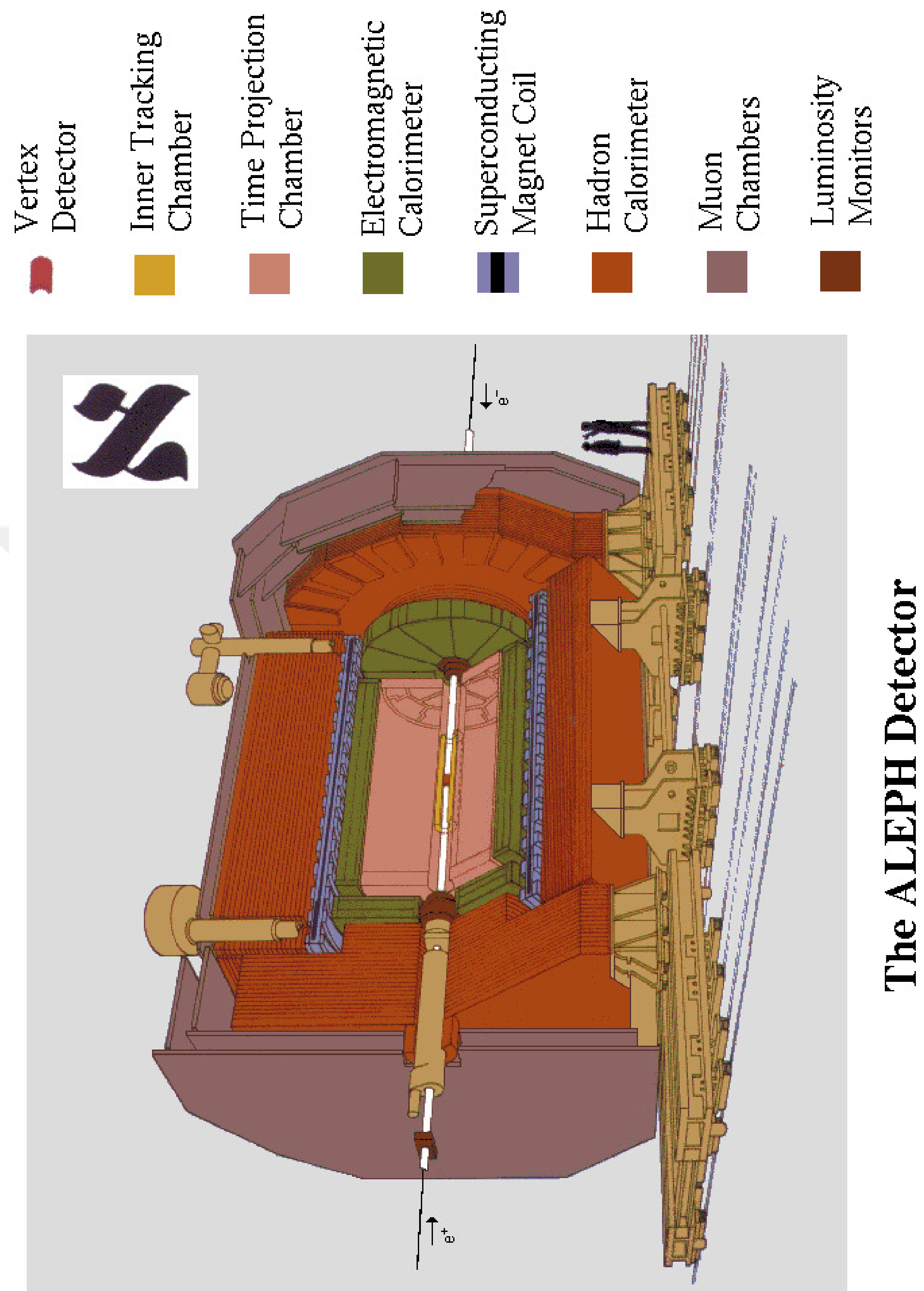

Figure 3.3 Schematic view of the ALEPH detector. Subdetectors are indicated by different colors.

Three sub detectors forms the tracking system: a silicon vertex detector, a drift chamber having outer radius 30 cm, which is a part of the trigger system, and a time projection chamber having outer radius that is 180 cm. Calorimetry consists of two stages: hadronic and electromagnetic. The detector is surrounded by two double-layers streamer muon detection system tubes. Luminosity calorimeters are important for the measurement of cross-section precisely.

The apparatus mainly presented here. For more details see ref [18, 19].

3.4.2 The Central Tracking Chambers

VDET (The Vertex Detector)

Silicon vertex detector stores tracking information from hits around collision point. Hits are providing additional precise information for above tracking mechanism. From this, it is then possible to reconstruct the decay topologies of short-lived particles with typical decay lengths of as little as a few tenths of a millimetre. The configuration of the VDET is shown in Figure 3.4.

The detector contains silicon wafers, 96 in total, that has $(5.12 \times 5.12 \times 0.03)$ cm dimensions. Two cylinders positioned to be coaxial around the pipe of beam. There are nine wafers in the inner layer azimuth with 6.5 cm radius on average. On the other hand, there are 15 wafers with 11.3 cm radius on the above layer. Each layers are contains four wafers giving a total length of 20 cm. Each wafer has 100 μm strip readout both parallel ($r\phi$) and perpendicular (rz) to the beam direction. Incident tracks have space resolution, $\sigma_{r\phi} \approx 12$ micron and $\sigma_z \approx 10$ micron.

ITC (Inner Tracking Chamber)

Conventional cylindrical drift chamber surrounds the vertex detector which is measuring the position $r\phi$ of the track on eight layers of drift cells positioned as a hexagon with radius 16 to 26 cm. Adjacent layers gradual with a width of half of the cell. Drift length defines the resolution on average 150 micron. Measured difference time of signal arrival determines the position of tracks on each end along the beam direction (z). Resolution by this is only about 5 cm. Resolution of tracks is improved by the tracker information. Information is also providing the decision of trigger after crossing of beam in about 2 micro second.

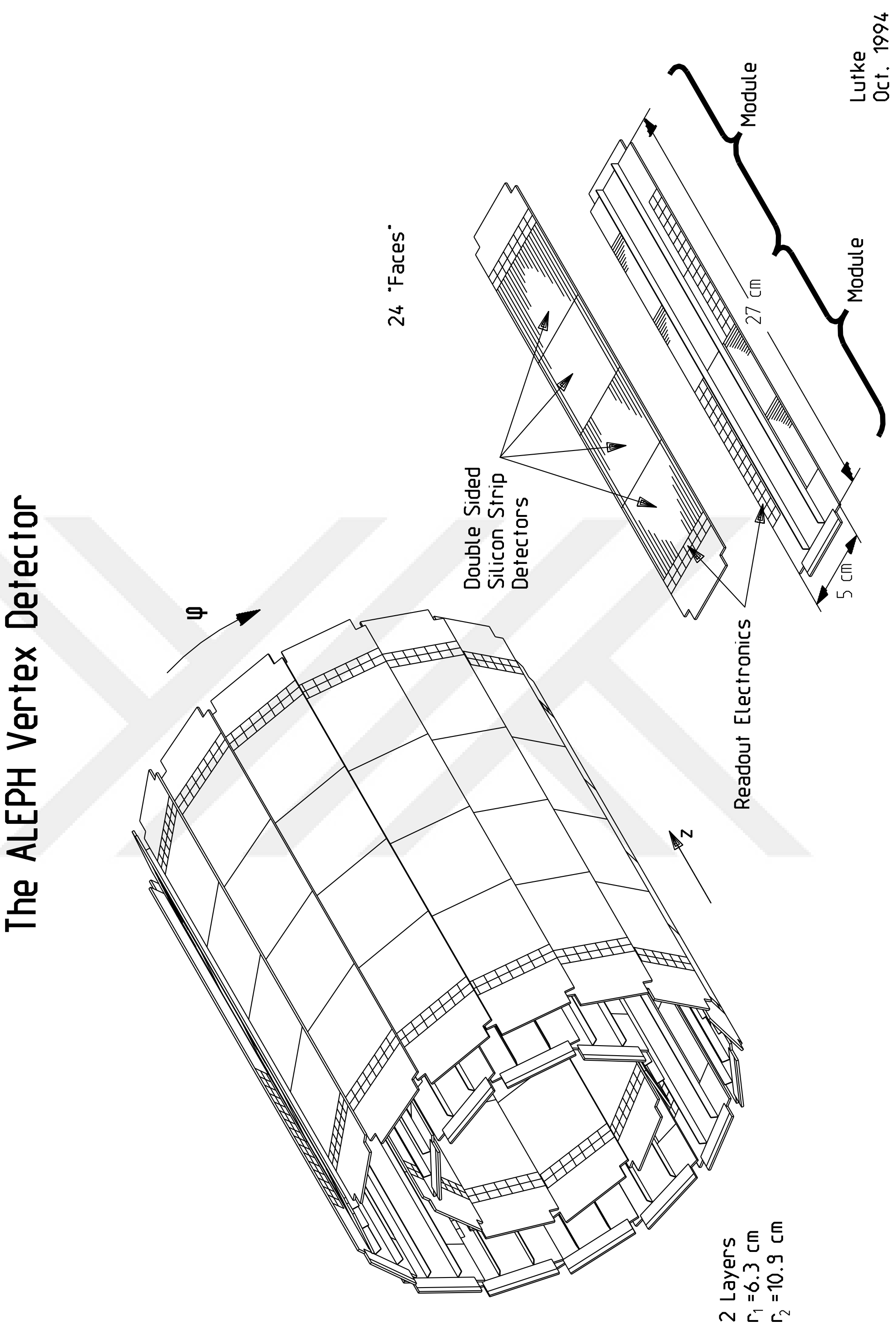

Figure 3.4 Configuration of the original (1991) vertex detector. The VDET is very close to the beam pipe in order to identify very short-lived particles (such as τ leptons and B mesons) with a high resolution position. This detector consists of two concentric arrays of silicon wafers surrounding the beam pipe.

TPC (Time Projection Chamber)

The time projection chamber is the principal detector for tracking which provides 3D spatial measurements at 21 points for the tracks with radius from 30 to 180 cm. A view of the TPC is given in Figure 3.5 which consists of a volume filled with gas bounded by cages at two ends. Central midriff and the two plates separated by 2.2 meters, have electric field in between. Charged tracks ionises the gas as by passing the chamber. Avalanches are produced by the drift of the electrons causing pulses on cathode. Signals inducing cathode are interpolated to calculate coordinate of ϕ. Radial measurement of position gives the r coordinate. Drift time and velocity of trajectory provides information about the z coordinate.

Lost energy in TPC of the particle is measured by the height of pulse on wires. Mass of the particle variates loss of energy (dE/dx) which is used on identification of particles. Identification of electrons, with σ greater than 3, separates up to 8 GeV momentum.

Each end-plate of the TPC is subdivided into eighteen individual wire chambers (sectors), the arrangement is shown in Figure 3.6. The pad size is 6.2 mm $\times$ 30 mm ($r\delta\phi \times \delta r$) and the pad pitch in azimuth is 6.72 mm. The geometry of the sectors is designed to minimise losses in track resolution due to the cracks between the sectors. The resolution is dependent on the angles which a charged track makes with both the sense wires and the cathode pads. The resolution in azimuth coordination is $\sigma_{r\phi} = 180$ micron at zero degrees angle of crossing. The z space resolution is 1.2 mm and 0.8 mm for wires and pads respectively.

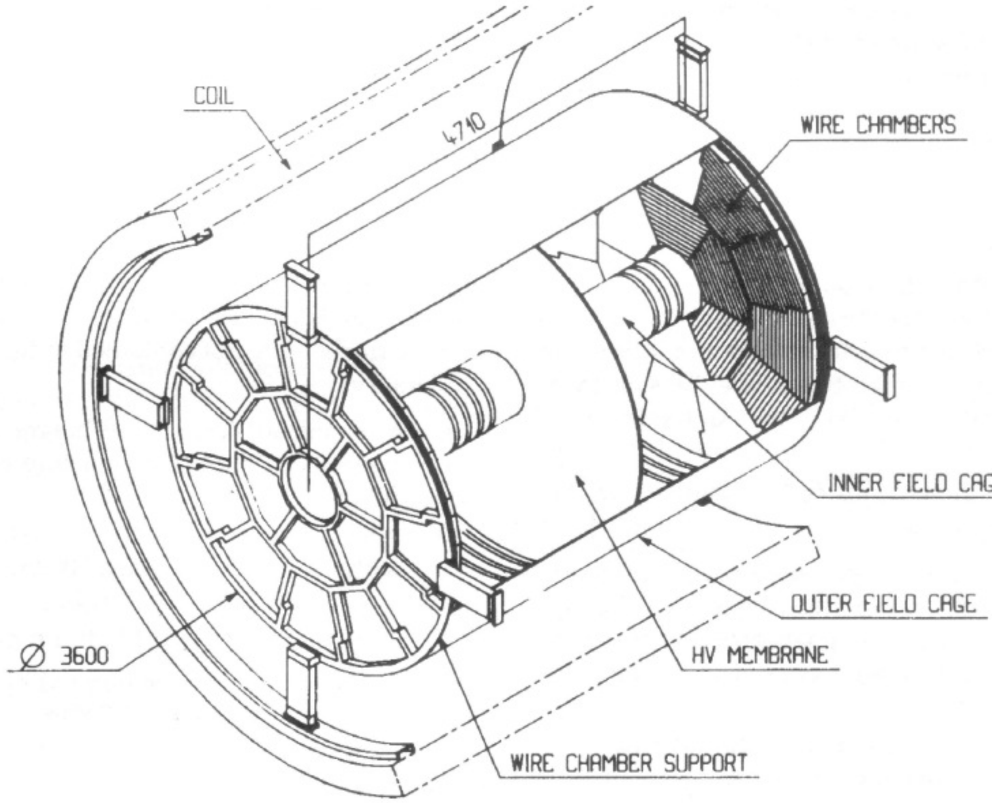

Figure 3.5 A view of the time-projection chamber.

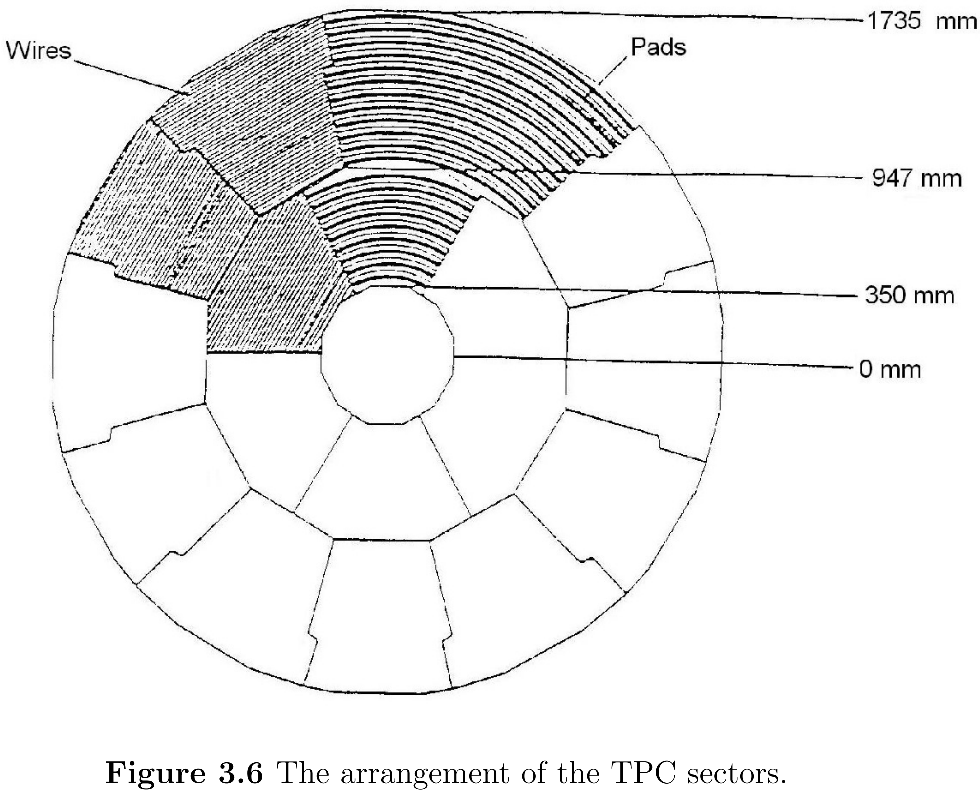

Figure 3.6 The arrangement of the TPC sectors.

Table 3.1 shows the transverse momentum and impact parameter resolutions for three tracking detectors together.

Table 3.1 Momentum resolution and impact parameter resolution for the TPC only, with ITC, and the all three detectors including VDET. Constant term 0.5% needs to be added to the resolution of momentum because of several scattering at lower values of momentum.

	Resolution of Transverse momentum (p_T in GeV)	Resolution of Impact parameter	
Detector	$\Delta p_T/p_T$	$\sigma_{r\phi}(\mu m)$	$\sigma_{rz}(\mu m)$
TPC	$1.2 \times 10^{-3}\ p_T$	310	808
TPC + ITC	$0.8 \times 10^{-3}\ p_T$	107	808
TPC + ITC + VDET	$0.6 \times 10^{-3}\ p_T$	23	28

3.4.3 The Principal Calorimeters

The energy and position coordinates of secondaries from high-energy interactions can also, under suitable conditions, be measured by total absorption methods. In the absorption process, the incident particle interacts in a large detector mass, generating secondary particles which in turn generate tertiary particles, and so on, so that all (or most) of the incident energy appears as ionisation or excitation in the medium−hence the term calorimeter.

For electrons and photons of high energy, a dramatic result of the combined phenomena of bremsstrahlung and pair production is the occurance of cascade showers. A parent will radiate photons, which convert to pair, which radiate and produce fresh pairs in turn, the number of particle increasing exponentially with depth in the medium. A measurement of the position and charge of a shower provides a measure of the position an energy of the electron or photon.

The Electromagnetic Calorimeter (ECAL)

The ECAL is a proportional wire calorimeter containing lead sheets. The chambers cover the range $|\cos\theta| < 0.98$ angular. The calorimeter measures the energy of electrons and photons while braking them. A barrel closed at ends surrounds the TPC which forms the ECAL. Sub divided 12 modules cover an angle of 30 degrees in azimuth as shown in Figure 3.7. The ECAL is insensitive at the cracks which constitute about 2% and 6% in the surface of barrel and endcap respectively. Azimuthal roration of endcaps by 15 degrees ensures that the cracks are not coincident in barrel and endcaps.

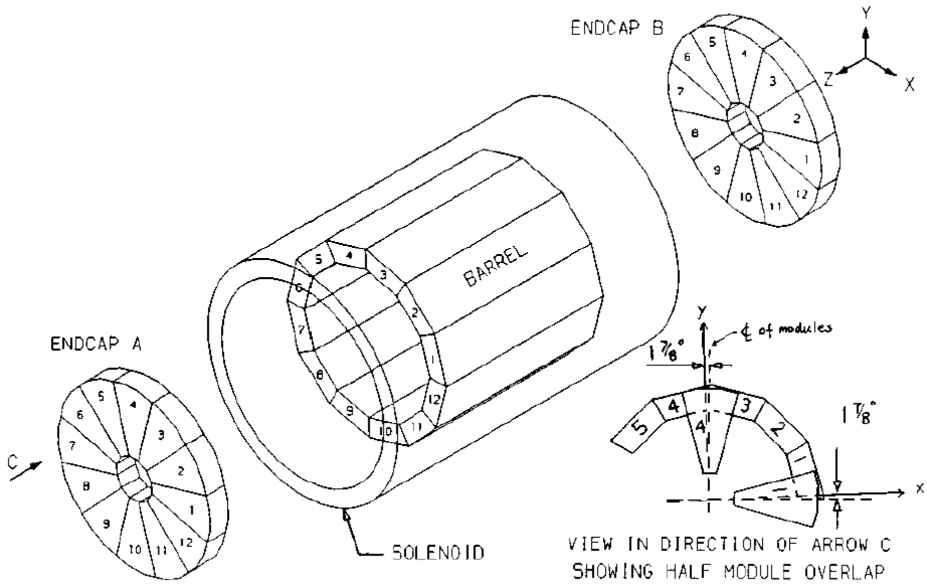

Figure 3.7 Schematic view of the ECAL modules.

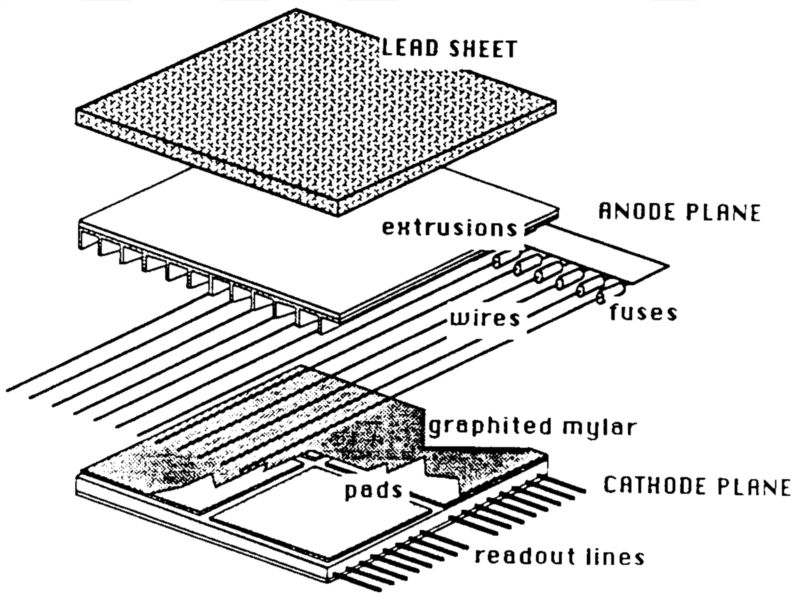

Figure 3.8 ECAL lead/wire-chamber layers.

The modules contain layers of 45 lead wire chambers as shown in Figure 3.8. Tower form which is pointed to the point of interaction is obtained by arranging cathode pads (30 x 30 mm). The position and energy of showers is read out by this form. Structure is important photon, netural pion and the electron identification. The angular resolution is calculated for the ECAL as

$$\sigma_{\theta,\phi} = \left(\frac{2.5}{\sqrt{E}} + 0.25\right) \text{mrad} \tag{3.3}$$

where E is measured in GeV.

Electrons within the energy range between 1 and 45 GeV are used in the calibration. The energy resolution can be obtained by comparing the measured energy to the particle energy. Figure 3.9a shows the resolution as a function of the electron energy. A linear fit results in a resolution function as follows:

$$\frac{\sigma_E}{E} = \frac{0.18}{\sqrt{E}} + 0.009 \tag{3.4}$$

where E is measured in GeV. General form of the form of the Equation 3.4 is:

$$\frac{\sigma_E}{E} = \frac{R}{\sqrt{E}} + k \tag{3.5}$$

where R is called stochastic term (slope of Figure 3.9a) and k is the constant term (intercept of Figure 3.9a). This equation can be explained as follows. Energy measured, E, is proportional to number of electrons, n, which are counted in the ECAL shower, because the number of charges is related with energy deposition in any space. Thus:

$$E \propto n$$

But, this counting is a statistical process carrying a statistical uncertainty $\sqrt{n}$ and so the statistical uncertainty on the energy measurement, the statistical component of energy resolution, can be written as:

$$\sigma_E \propto \sqrt{n}$$

One can set up the ratio σ_E/E:

$$\frac{\sigma_E}{E} \propto \frac{1}{\sqrt{n}}$$

and use the relation $E \propto n$:

$$\frac{\sigma_E}{E} \propto \frac{1}{\sqrt{E}}$$

Hence the last relation can be written as an equality by using proportionality constant R,

$$\frac{\sigma_E}{E} = \frac{R}{\sqrt{E}} \tag{3.6}$$

It is clear why R is called the stochastic term. If we compare Equation 3.6 with 3.4, we see $R = 18\%$.

The energy resolution of the ECAL depends not only on stochastic term R but also on the constant term k. This term, however, is significant only at very high energy (≥ 100 GeV). The value for R and k depend on the particular detector[1]
.

The energy resolution (as a function of polar angle) is shown in Figure 3.9b for electrons from Bhabha events. The energy resolution around 40° is degraded. This corresponds to the overlap region where the endcap and barrel intersects.

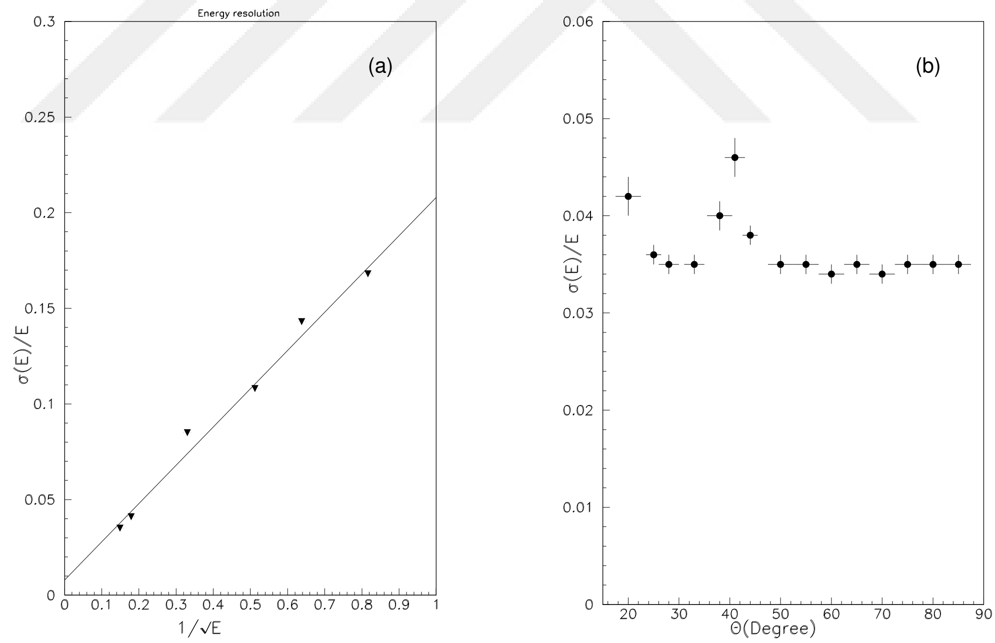

Figure 3.9 Energy resolution of the ECAL; as a function of (a) energy and (b) polar angle for electrons from Z decays (namely, $Z \rightarrow e^+e^-$).

[1] For example, new generation detectors for LHC, $R = 10$ % and $k = 0.7$ % for ATLAS ECAL, and $R = 4$ % and $k = 0.5$ % for CMS ECAL.

The Hadron Calorimeter (HCAL) and Muon Chambers

The hadron calorimeter is used with ECAL in order to measure deposition of hadronic energy. Also, it is a part of the muon identification system. It is composed of 23 layers of plastic streamer tubes which are separated by 5 cm iron slabs, giving a total of about 7.2 interaction lengths at 90 degrees. Calorimeter is made up of 36 modules (24 in barrel and 6 in both endcaps). It is read out in 4788 projective towers with a typical tower coverage of $3.7° \times 3.7°$, which corresponds to 4×4 of the electromagnetic calorimeter towers. The streamer wire signals are summed and used as part of the trigger. The energy resolution of the HCAL for charged pions at normal incidence is given by

$$\frac{\sigma_E}{E} = \frac{0.85}{\sqrt{E}} \tag{3.7}$$

where E is measured in GeV.

Outside the HCAL are another two double layers of streamer tubes which form the muon chambers (acting as simple tracking devices). Two coordinates are obtained from cathode strips both parallel and perpendicular to the wires in each layer. In conjunction with HCAL, the muon chambers are used to identify muons and keep hadron/muon misidentification to a minimum.

3.4.4 The Superconducting Solenoid

The ALEPH magnet is a liquid helium-cooled superconducting solenoid with a magnetic field strength of 1.5 T at a current of 5000 A. The field provides the curvature to charged tracks from which the momentum and sign of charged particles can be determined.

3.4.5 The Luminosity Monitors

The precise measurement of electroweak parameters requires accurate knowledge of the beam luminosity. The reaction rate for a process is given by $\mathrm{R} = \sigma\mathcal{L}$ where σ is the interaction cross-section and $\mathcal{L}$ is the luminosity. Low angle elastic (Bhabha) scattering is used to measure the luminosity as it is almost a pure QED process with very little interference from the weak sector, and has a well known cross-section.

The Silicon Calorimeter

The Silicon Luminosity Calorimeter (SiCAL) is ALEPH's main detector for providing luminosity measurements. It is positioned around the beam pipe at each end of the detector and covers angles between 24 to 58 mrad from the beam axis.

The SiCAL uses 12 silicon/tungsten layers (23.3 radiation lengths) to sample showers produced by Bhabhas. Finely spaced pads determine the angle of an incident particle with a polar resolution of 0.15 mrad. The shower depth gives a measure of the energy deposited with a resolution of 3.4% at 45.5 GeV.

The Luminosity Calorimeter

The Luminosity Calorimeter (LCAL) is a lead/wire calorimeter, similar in design to the ECAL, comprising 38 layers (24.6 radiation lengths). Modules are positioned, on either side of ALEPH, just behind the SiCAL modules. The LCAL monitors polar angles from 45 to 190 mrad with a resolution of 0.5 mrad (at 45.5 GeV), and has an energy resolution of $\sim 0.15/\sqrt{E} + 0.01$, where E is measured in GeV.

BCAL

Online luminosity monitoring is provided by the Bhabha calorimeter (BCAL). This is a sampling calorimeter made of layers of tungsten and plastic scintillator, with a single plane of silicon strips to provide position measurements. The BCAL is positioned next to the beam pipe at 7.7 m from the interaction point, receiving a Bhabha hit rate of ≈ 7 Hz.

3.4.6 ALEPH in Numbers

The ALEPH detector dimensions and resolutions are summarised in Table 3.2. The data is taken from [20].

Table 3.2 A summary table showing the sizes and resolutions of the some subdetectors of the ALEPH detector.

Detector	R_{inner} cm	R_{outer} cm	Length cm	Resolution
VDET	6.5	10.8	20	$\sigma(r,\phi) = 12\ \mu$m $\sigma(z) = 10\ \mu$m
ITC	12.8	28.8	200	$\sigma(r,\phi) = 20\ \mu$m
TPC	31	180	470	$\sigma(r,\phi) = 180\ \mu$m $\sigma(z) = 1$ mm $\sigma(p) = 1.2 \times 10^{-3} p^2$ GeV/c
ECAL	185	225	477	$\sigma(\theta,\phi) = 2.5/\sqrt{E} + 0.25$ mrad $\sigma(E) = 0.18E + 0.01\sqrt{E}$ GeV
HCAL	300	468	700	$\sigma(E) = 0.85E$ GeV
SICAL	6.0	14.6	12	$\sigma(\phi) = 0.3^o$ $\sigma(z) = 7$ cm $\sigma(E) = 0.23\sqrt{E}$ GeV
LCAL	10	52	42	$\sigma(\theta) = 2.5\sqrt{E} + 0.16$ mrad $\sigma(E) = 0.15E + 0.01\sqrt{E}$ GeV

3.5 Trigger and Data Acquisition Systems

3.5.1 The Trigger System

ALEPH employs a three-level triggering system in order to separate genuine e^+e^- interactions from background, to reduce the frequency of accepted events to a rate which can be written to tape, i.e. about 1-2 Hz, and to reduce the dead-time of the detector. The background events are mainly from three sources: beam-gas interactions, off-momentum particles from the beam hitting either collimators or the vacuum pipe, and cosmic rays.

The maximum output acceptable from the level 1 trigger is a few hundred Hertz in order to keep dead-time in the data acquisition to a minimum and to ensure there are no TPC gating problems. To enable the trigger to be sensitive to all areas of physics, it uses information from the HCAL, ECAL, LCAL and the ITC. After a bunch crossing, there is a level 1 *yes* if:

- there are track candidates in the ITC;

- there is energy in a 'trigger region' of the ECAL or HCAL;
- the total energy in the barrel, in either endcap, or entire detector is larger than given thresholds;
- there is a Bhabha event in the SiCAL.

Level 1 uses dedicated hardware to enable a decision to be reached in 5 μs, therefore a level 1 *no* can be reached before the next bunch crossing. The level 1 trigger has a 100% efficiency for hadronic Z decays and $(99.7 \pm 0.2)\%$ efficiency for Bhabha events.

The second level trigger decision is made within 50 μs of the bunch crossing and is used to verify the first level trigger. The trigger only involves the TPC; trigger pads on the TPC end-plates are used to check for the presence of charged particle trajectories in regions predicted by the Level-1 decision. Its aim is to stop and clear data acquisition if it cannot confirm the Level-1 decision. A *yes* decision initiates the readout from the front-end electronics and the data are transferred through the DAQ system. This rate should be kept below 10 Hz in order to keep the dead-time to a minimum; about 75% of the level 1 track-only triggers are removed.

The third level trigger is a 'software trigger' and is only applied after the readout of an event. The aim of this third-level event selection is to identify genuine e^+e^- interactions and separate them from the background triggers, and reduce the output frequency to the desired 1-2 Hz.

3.5.2 The Data Acquisition System (DAQ)

The role of the DAQ is to read the electronic signals of events and format the data so that they may be recorded for event reconstruction. A simplified view of the DAQ system is presented in Figure 3.10, illustrating the flow of data from the front-end electronics to the final stage of event reconstruction. The main steps in the data flow are as follows:

(1) A timing signal, synchronised with the LEP bunch crossings, is sent to the trigger supervisor from the T0 module.

(2) The trigger supervisor transmits the timing signal to the readout controllers (ROCs) which, for most of the subdetectors, initiates the

digitisation in the front-end electronics. After compacting the data through 'zero-suppression', calibrations are applied and the reduced data formatted. The results are then stored in the ROCs' output buffers.

(3) The Level 1 and Level 2 trigger decisions are made and transmitted to the ROCs. A rejection halts the digitisation process and causes the ROCs to be reset and prepared for the next event. If a trigger is accepted at Level 2 then the whole event is digitised.

(4) After digitisation, each ROC sends a signal to the corresponding subdetector event builder (EB) for its data to be read out. These data are processed by the EB and stored in its output buffers.

(5) With an event in its output buffer an EB sends a request to the main event builder (MEB) to be read out. The MEB reads all the subdetector EBs and assembles the whole event. After testing for completeness, the event is passed to an event processor (EP) which performs the Level 3 trigger analysis. A Level 3 *yes* decision results in the event being written to a disk and then to tape. The data are now available for event reconstruction, this is the subject of the next chapter.

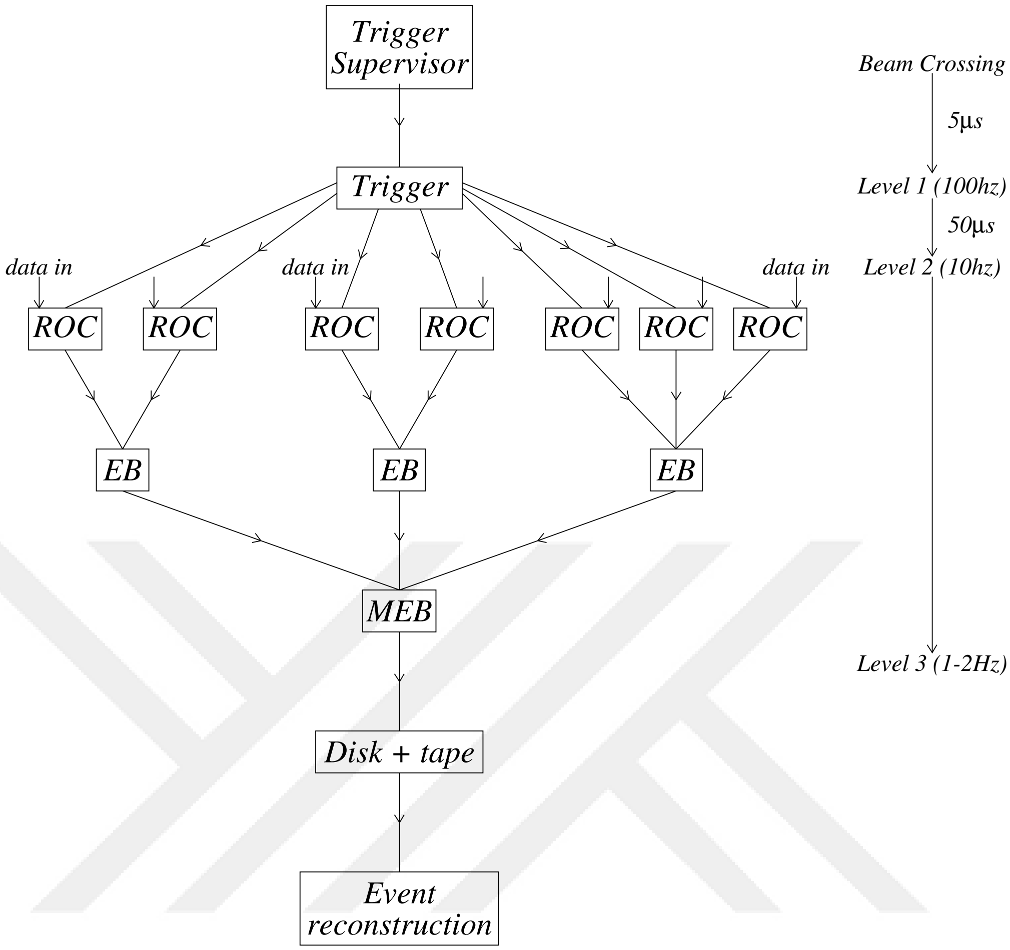

Figure 3.10 A simplified outline of the data acquisition (DAQ) system, including the trigger sequence.

CHAPTER 4

EVENT RECONSTRUCTION AND SIMULATION

4.1 Introduction

Recorded data containing the raw event information are reconstructed offline by the JULIA program. Tracking and calorimeter reconstruction is performed on both real and simulated data (simulated data will be discussed in Section 4.6). The results from JULIA are formed into BOS banks and written to Production Output Tapes (POTs) and then to Data Summary Tapes (DSTs) ready for physics analysis; DSTs contain almost all the information from the POTs, but with non-interesting events (i.e. noise and background) removed. Figure 4.1 illustrates the flow of data from event production to the storage of reconstructed events ready for physics analysis.

A more compact form of data storage is the Mini-DST, which is important for analyses which process a large number of events. Mini-DSTs contain less information and the data are integerised, so that these tapes can be staged to disk more quickly, or stored permenantly on disk, and read more quickly by the analysis program. Additionally, results of some time-consuming algorithms are already available on the Mini-DSTs, further reducing processing time. The Mini-DST is used in the analysis presented in this thesis. The total data (6.4 million Monte Carlo and 4.2 real data events) occupies 100 Gbyte of disk space.

The reconstruction of data by JULIA is described here with emphasis on track reconstruction in the TPC and γ/π^0 reconstruction in the ECAL. The final section describes event simulation.

4.2 Track Reconstruction

Figure 4.2 shows examples of the reconstruction of tracks from coordinates in the TPC. Each track is the result of fitting a helix to chains of 3-dimensional space coordinates which are consistent with the trajectory of a charged particle. Note that the tracks are curved in the xy projection, but straight in the z projection. The following sections describe details of TPC coordinate determination and track fitting.

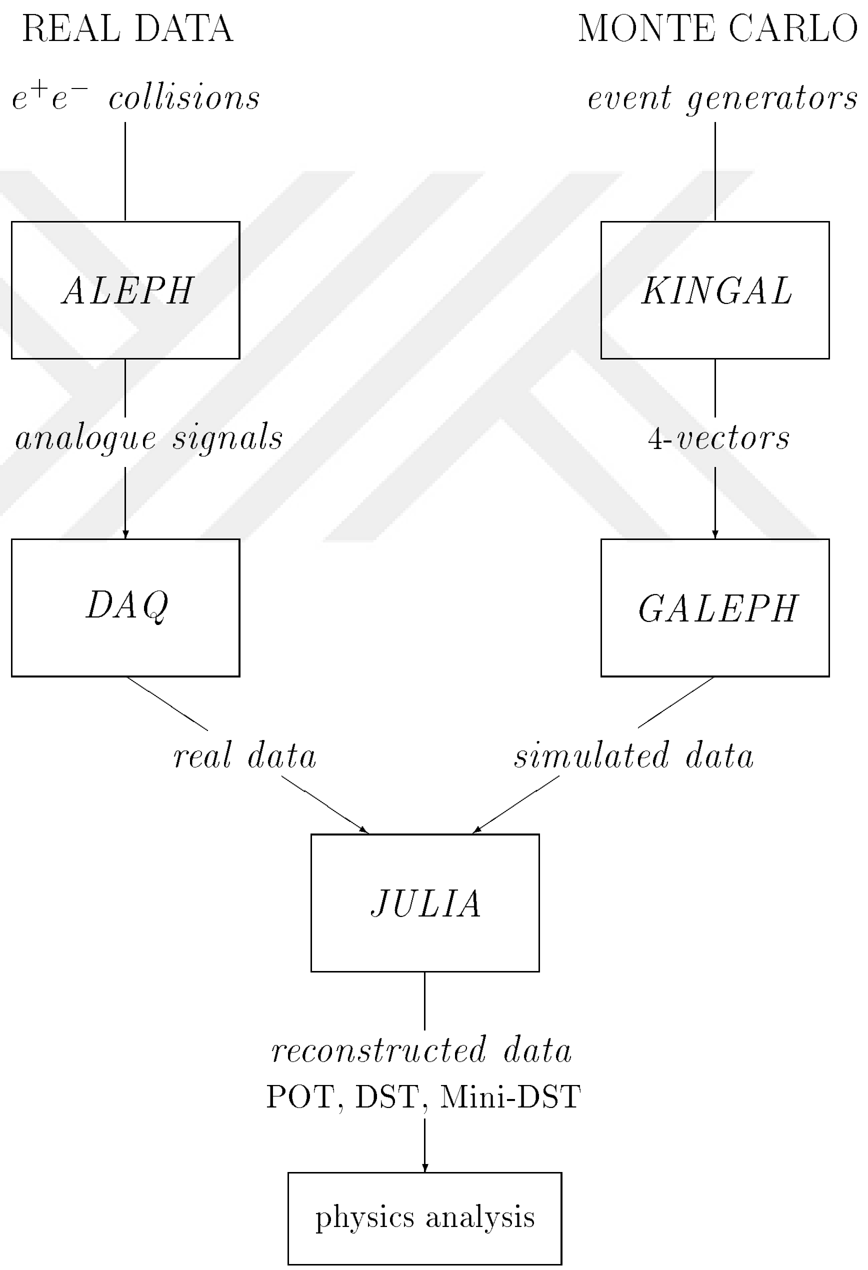

Figure 4.1 The flow of data in the ALEPH experiment, including the simulated-data chain.

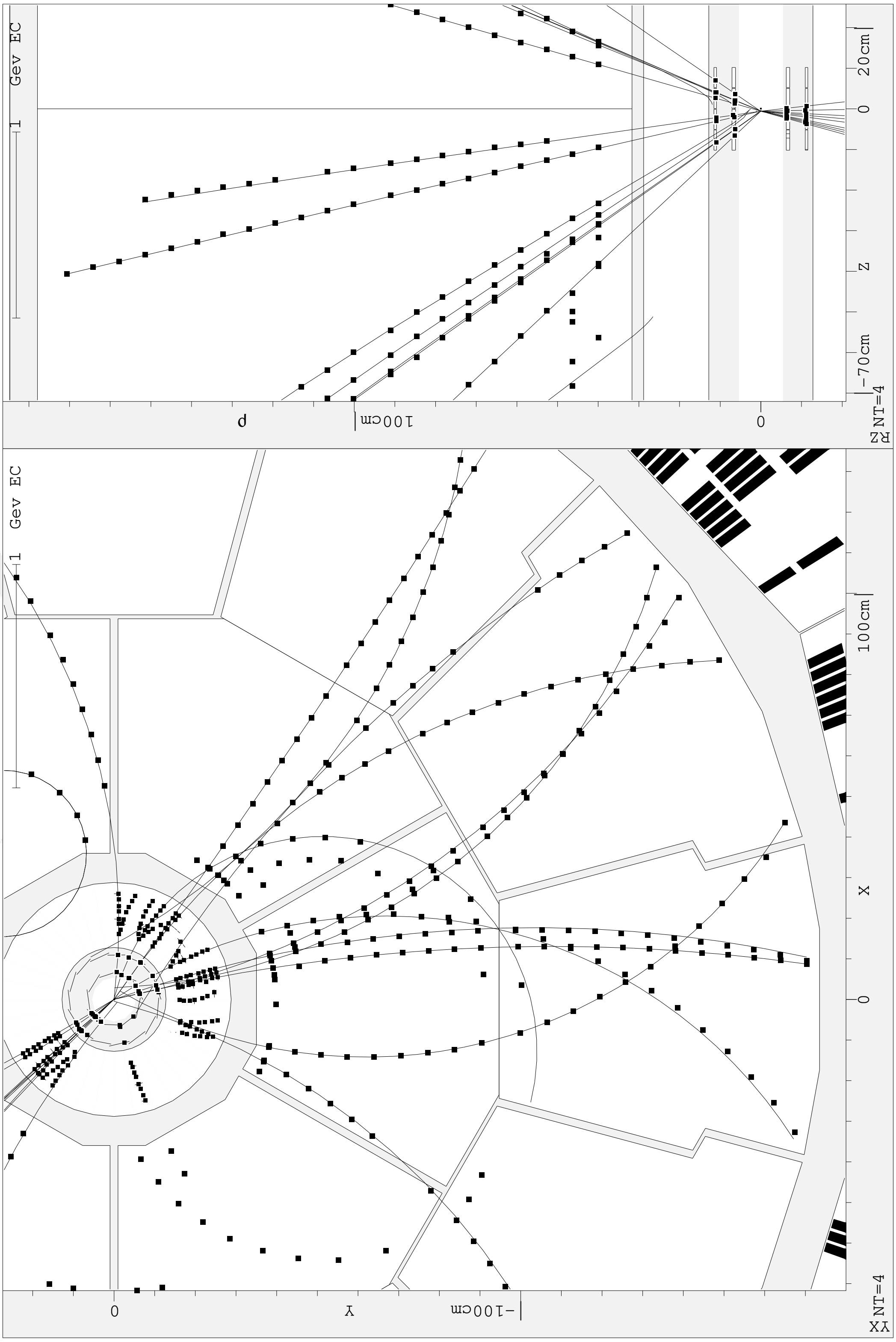

Figure 4.2 Reconstruction of tracks from coordinates in the TPC. Two projections are shown: the xy projection, and the rz ($r^2 = x^2 + y^2$) projection.

4.2.1 TPC Coordinate Determination

The raw data collected from the TPC comes in two forms:

- The pad hits, which contain the pad number, arrival time and duration of the pulse.
- Digitised pulse-heights per time-slice, or 'buckets', corresponding to each pad hit.

Clusters and Pulses

Coordinate determination begins with the identification of clusters of pad hits (pulses) on a given pad row in the plane of 'pad number' versus 'drift time'. A cluster is built, ignoring for the moment pulse-height information, by starting with one hit and including hits on adjacent pads if they overlap the first by at least one sample. An example of such a cluster is shown in Figure 4.3, the cluster is formed by two nearby tracks which are not clearly distinguishable at this stage.

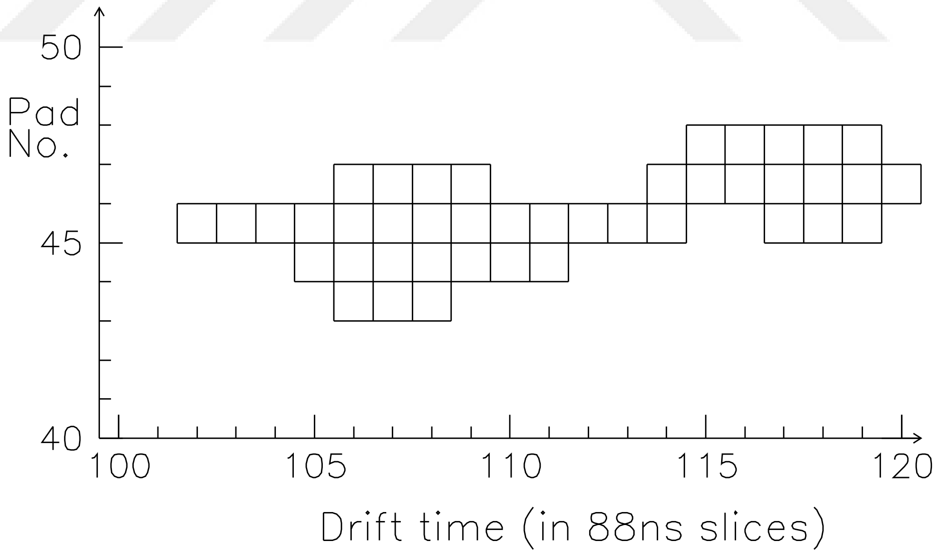

Figure 4.3 A TPC pad row cluster formed by two nearby tracks.

A good cluster satisfies the following criteria:

- A minimum of 2, and a maximum of 20 pads in the cluster.

- The minimum cluster length is 5 and the maximum is 35.

A rejected cluster is flagged as a ‘bad’ coordinate; such clusters are not included in track reconstruction.

Subclusters and Subpulses

Once clusters have been established they are analysed again with the pulse-height information included in order to separate, or at least recognise, within each cluster the contributions coming from different particles. Figure 4.4 illustrates an example of a cluster which is separated, in drift time (or z), into three subclusters by inspecting the pulse-heights. The charge profile of each pulse is analysed for evidence of multiple peaks. Peaks that are sufficiently isolated from others form subpulses. Groups of subpulses on adjacent pads are aligned with respect to time (or z) and grouped into subclusters. Within a subcluster, each subpulse must be on a separate pad. The charge profiles of the resulting subclusters are also scanned for evidence of multiple peaks; if a valley between peaks is sufficiently low then such a subcluster can be broken in $r\phi$, otherwise it is flagged as being unusable. Examples of such unusable clusters are shown circled in Figure 4.2: the hits from the two tracks originating from a photon conversion in the TPC gas are only resolved when the tracks are separated by a sufficient distance. For each subpulse, both a charge estimate and a time estimate are made from the digitisations. These are used in the reconstruction of coordinates.

Coordinates

Each ‘good’ subcluster is used to calculate a z and $r\phi$ coordinate. For the $r\phi$ coordinate the sub-pulse charge estimator is used: a Gaussian fit is made if the subcluster has 3 or less pads, or a charge-weighted average of the pad position is taken if the subcluster has more than 3 pads. The z coordinate is calculated using both the charge estimator and the time estimator.

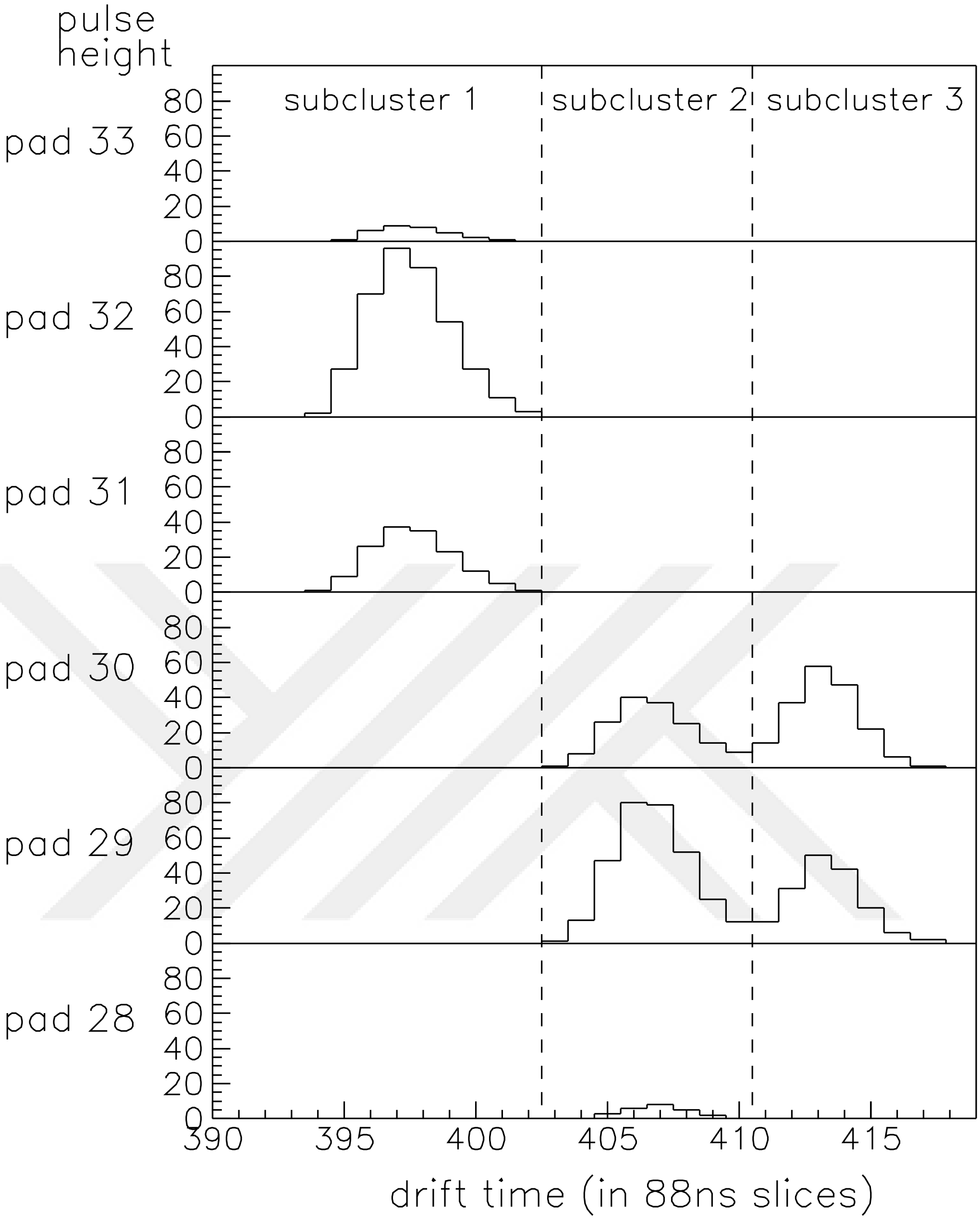

Figure 4.4 An example of a complex cluster and how the reconstruction program has broken it down into three contributions from which three individual coordinates can be calculated.

4.2.2 TPC Track Finding and Fitting

Track candidates are formed from TPC coordinates as follows. Sets of coordinates which are consistent with an arc of a helix less than π radians are formed into ‘chains’. Chains that are determined to belong to the same helix (e.g. multiple arcs of a spiral) are linked together into a single ‘track candidate’. To account for multiple scattering, the coordinate error estimates are increased in accordance with the distance from the track origin. If an acceptable fit is not obtained, then up to two points are removed from the fit, corresponding to those that contribute the most to the χ^2 of the overall fit. If this does not result in an acceptable fit then a search is made for a kink in the track candidate, and if one is found the track is split. If no significant kink is found then a search is made for bad points by fitting a track candidate with one point at a time removed. If none of these methods leads to a good fit the track candidate is kept without modification. Details of the algorithms used to find and combine the chains into track candidates can be found in [21].

The track finding efficiency in the Time Projection Chamber is studied using Monte Carlo. In hadronic Z decays, about 99% of tracks crossing at least four pad rows are reconstructed successfully.

The five helix parameters given in Figure 4.5 can be found by fitting a helix function to the pad coordinates.

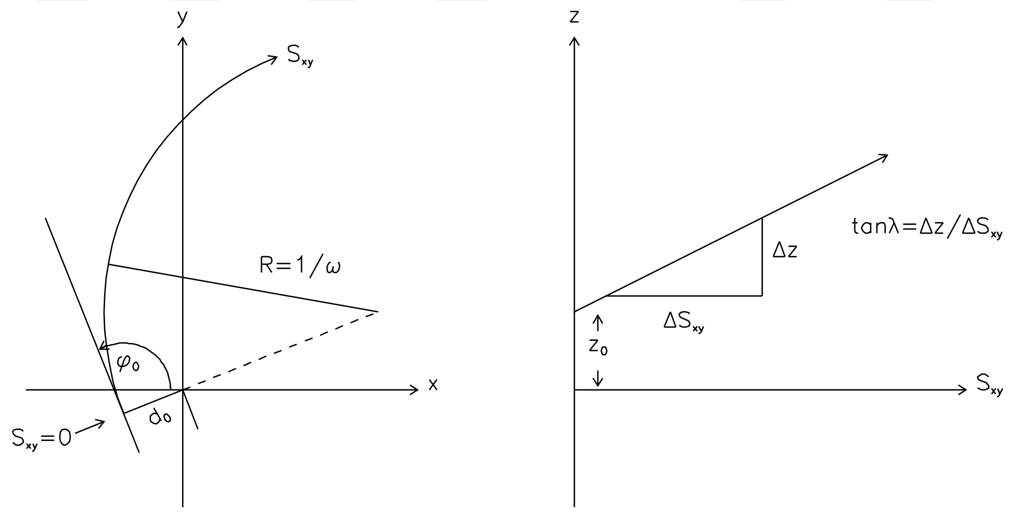

Figure 4.5 Helix parameters used for track finding algorithms in TPC.

A circle fit performed in $x-y$ plane results in ω (defined as inverse radius of curvature), d_0, and ϕ_0 (the angle of emission in $x-y$ plane). A linear fit in the s_{xy}-z plane yields z_0 (the z coordinate at the closest approach to the z axis) and

$\tan\lambda$ (representing the tangent of dip angle). The circle fit parameters are used to calculate the values of s_{xy}.

4.2.3 TPC-ITC-VDET Track Association

Once TPC tracks have been identified, ITC and VDET coordinates are added to improve the track measurement. The TPC tracks are projected back into the ITC and a search is made for ITC coordinates within a 'window' defined in z and ϕ around the trajectory. If no ITC hits are found in the first two outer layers then the search is abandoned. If more than three hits are found, a fit is performed and the ITC coordinates may be accepted, subject to a cut on the χ^2 of the fit. Finally VDET hits are associated to tracks which extrapolate close to them and the tracks are then refitted.

4.3 Ionisation Energy Loss

The TPC also provides information on a charged particle's rate of loss of energy due to ionisation (dE/dx). This information is obtained from the measured ionisation on the TPC sense wires and is calculated as follows:

(1) The raw digitisations for each wire pulse are reduced to time and charge estimates.

(2) The wire pulses are associated with the reconstructed TPC tracks. Individual wire pulses that match to more than one track are ignored.

(3) The truncated mean dE/dx is calculated for every track: the dE/dx samples are distributed according to a Landau distribution and the mean is calculated after discarding the upper 40% and lower 8% of the sample. The upper truncation is to reject samples arising from hard scattering, and the lower one reduces the dependency of the dE/dx estimator on the track angle and drift length.

4.4 Calorimeter Reconstruction

Data from the ECAL and HCAL are also processed by JULIA. This section describes briefly the formation of calorimeter objects, the following section describes in more detail the reconstruction and identification of photons in the ECAL.

Calorimeter Clusters and Objects

Clusters of energy deposition in the ECAL are formed by associating a group of spatially connected storeys (i.e. storeys which possess a common corner). All storeys which have an energy exceeding the threshold t_{low} (typically set to 30 MeV to minimise effects of noise) are used as input to the cluster finding algorithms. A topological cluster is only retained if it contains at least one storey above the threshold t_{high} (typically 90 MeV).

ECAL clusters are then associated with nearby charged tracks, clusters which are more than 3 cm (about one pad width) from the entry point of a charged track into the ECAL are considered to be neutral. Clusters associated with minimum ionizing tracks, electrons, and neutral particles are distinguished. Charged clusters with excess energy may have photons associated with them. A similar process is carried out to form HCAL clusters. Calorimeter objects are then formed from the calorimeter clusters with the possibility of more than one particle contributing to each object. ECAL and HCAL objects which overlap are merged into combined calorimeter objects. Further information on calorimeter reconstruction can be found in [21].

4.5 Photon Reconstruction

The clustering algorithm described above builds large clusters, often merging energy from photons and hadronic interactions. For the purpose of improving photon reconstruction, particularly in hadronic events, an extension to the above algorithm is implemented. It uses the facts that electromagnetic showers generally start in the first segment in depth of the electromagnetic calorimeter and that, unlike the cell patterns of hadronic clusters, storeys receiving energy from a photon have a compact arrangement and most of them share a face with another storey associated to the same photon. Figure 4.6 shows the energy deposits of three photons in the ECAL, the showers begin in stack 1 (the first picture), they have a maximum in stack 2, and have almost completely disappeared by stack 3. It is apparent from the figure that the large cluster contains two subclusters due to two photons, the algorithm for photon reconstruction described here attempts to resolve these clusters by forming 'G-clusters' as follows.

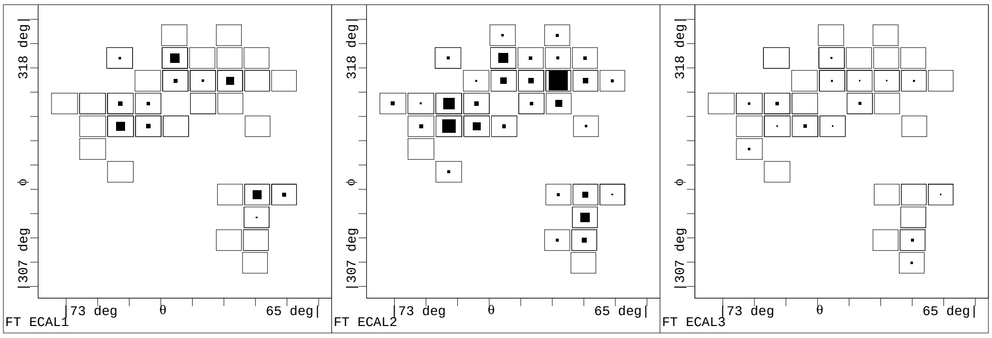

Figure 4.6 Energy deposits of three photons in ECAL towers; the showers begin in stack 1 (the first picture), they have a maximum in stack 2, and almost completely disappear by stack 3. All towers contributing to the cluster are shown in each stack; empty boxes represent tower storeys containing zero energy.

4.5.1 G-clusters

G-clusters are formed as follows. The storeys of stack 1 of the ECAL are scanned in the order of decreasing energy. A storey without a more energetic neighbour defines a new G-cluster. Other storeys in the same stack are assigned to the cluster of their highest energy neighbour, storeys are considered neighbours only when they share a common face. The procedure is repeated for storeys in the second and third stacks but, the algorithm looks first for a neighbour in the previous stack during the process of a storey. G-clusters which are found by the algorithm are maintained as photon candidates depending on the condition whether or not their energy is greater than 0.25 GeV, and if no charged track impact at a distance of less than 2 cm from G-cluster barycentre exists. The efficiency and the background strongly on the density of the particle impacts on calorimeter.

Photon Position Calculation

The position of the photon impact point is given by the G-cluster barycentre. Position is corrected for biases according to the finite cell size of the calorimeter.

Photon Energy Calculation

The photon energy is computed by using the energy collected in the four central towers of the cluster and expected value of the energy fraction in four towers F_4 to reduce the sensitivity of energy measurement to hadronic background and clustering effects. For a single photon in calorimeter, this fraction is computed from the parametrisation of the shower shape. The calorimeter pad area and the distance between the photon impact and the nearest tower corner is taken into account in computation as well as the variation with energy of the expected F_4. Corrections to the energy are computed for energy losses before and after the ECAL and in the region where the ECAL edncap and barrel overlap.

π^0 Reconstruction

The reconstruction of neutral pions from G-clusters provides an improvement in purity and efficiency. The identification of subclusters is particularly useful for higher energy pions where the energy deposits of the daughter photons overlap. Discussion of π^0 reconstruction from G-cluster photons will be reserved until Chapter 6 where the methods will be shown in detail as part of the analysis presented in this thesis.

4.5.2 Merged Photons

For the energies above 10 GeV, the probability of resolving a π^0 into two G-clusters decreases. Further information is contained in the distribution of energy in calorimeter. Extract it takes computation of energy weighted moments of the two dimensional energy distribution. Assuming that cluster contains just two photons, it is possible to reconstruct two photon momenta and compute their mass by using moments up to the third order. This allows a check of π^0 hypothesis for unresolved high energy clusters. An example of the use of this method can be found in [22].

In this thesis, as the signal-to-background improves at high energy, we do not attempt to reconstruct unresolved high energy clusters.

4.5.3 Converted Photons

An alternative to taking photons from the ECAL is to take converted photons reconstructed in the TPC. About 7% of photons convert in the tracking chambers and are therefore not reconstructed as neutral objects in the ECAL. However, these photons may be reconstructed from their daughter particles identified in the TPC. This provides a much improved energy resolution[1] [23]. This method can be used to reconstruct, for example, Σ° baryons (decaying to $\Lambda\gamma$). However, the method suffers from very low efficiency. The efficiency can be significantly improved, particularly at low energy, by including single arm conversions (where one electron or 'arm' is retained in the material of the detector) though with a loss of energy resolution. Single arm conversions have been used in the reconstruction of B^* mesons (decaying to $B\gamma$) [24].

For neutral pion reconstruction at low energy, converted photons provide π^0 candidates of higher purity than that obtained from ECAL photons [25]. Again, the problem is the very low efficiency; a combination of converted photons and ECAL photons regains some efficiency though with a reduction in purity.

One may think that D^{*0} analysis can be improved by including converted photons. Since the photon conversion probability is about 7% in the detector, its contribution to reconstruction of the signal is negligible in terms of statistics. We therefore do not attempt to reconstruct converted photons.

4.6 Event Simulation

For the purpose of comparing with the model, and by means of measuring the acceptance of the detector, a sample about 6 million Monte Carlo simulated events are generated with the Jetset [26] software and progressed by a full detector reconstruction simulation. After event selection, the number of Monte Carlo events is about 5 million. The generator is tuned to describe the ALEPH data using the inclusive charged particle and event shape distributions [27].

For further model comparison and as a systematic check for the extrapolation into the unmeasured region, the measured spectra were compared to those of Pythia8.2 [28] and Herwig++2.6 [29]. The model parameters were tuned using ALEPH data in the same manner as mentioned above.

[1] For low energy photons the improvement is around an order of magnitude.

Event simulation proceeds in two steps: simulation of the physics under investigation (carried out by event generators and the KINGAL program), and simulation of the response of the detector to the KINGAL particles (carried out by the GALEPH program).

4.6.1 KINGAL

The KINGAL package is effectively an interface between the event generators and GALEPH. The event generators use Monte Carlo simulation techniques to produce the desired physics. The KINGAL output gives a 4-vector kinematic representation of each simulated particle. Short-lived resonances are decayed according to decay tables based on experimental data; longer-lived particles are retained so that secondary vertices can be generated in GALEPH.

4.6.2 GALEPH

The Generator for ALEPH (GALEPH) is a detector simulation, representing the interaction of particles with the material of the detector, and the response of the detector to the particles. It generates digitised pulses with the same format as those produced by the data acquisition system.

The GALEPH package uses the GHEISHA package to simulate hadronic showers. Electromagnetic shower simulation is carried out using the GEANT software [30]. Particle scattering as well as energy loss calculations are also carried out by the GEANT package. The quality of the simulation can be seen in the plots presented in Chapter 5, and is further discussed in Chapter 6.

CHAPTER 5

EVENT SELECTION

Approximately 4.2 million hardonic Z^0 decays at center-of-mass energies within ± 2 GeV of the Z^0 peak mass where recorded by ALEPH from 1991 to 1995. After event selection cuts, described in the following sections, the total number of events selected for the analysis is about 3.2 million. Table 5.1 shows the contribution from each year of data taking.

Table 5.1 Selected hadronic events from each year of data taking.

Year	Number of hadronic events	LEP Energy $peak-2$, $peak-1$, $peak$, $peak+1$, $peak+2$
1991	223,963	4%, 4%, 82%, 6%, 4%
1992	548,356	100%
1993	528,854	11%, 0%, 72%, 0%, 17%
1994	1,345,422	100%
1995	593,151	8%, 0%, 78%, 0%, 14%
	total: 3,239,746	

Event selection covers two main areas: the first is a selection on event quality, the second is the selection of the hadronic signal Z $\rightarrow q\bar{q}$. These two areas are discussed below in Sections 5.1 and 5.2.

5.1 Data Quality

Several checks are made in an attempt to ensure events are of reasonable quality for analysis. For the real data 'run quality' is assigned to each run period based on checks at various levels. From this information, runs which are passed as good quality for the ECAL and TPC are selected. This includes runs with software fixes for TPC track distortions. Individual events are selected only if the relevant subdetectors have their high voltage on. A small fraction of the selected events (2.6% in 1992 and 0.4% in 1993) have the VDET high voltage off. Whilst the absence of the VDET in these events produces a visible degradation in tracking performance, particularly the impact parameter resolution, the effect is considered small enough for them to be included.

To remove events which suffer from a low geometric acceptance, a cut is applied on the polar angle of the event axis (with respect to the beam axis) as defined by sphericity. Events are accepted if this angle is in the range $35° < \theta < 145°$ ($|cos\theta| < 0.82$). Figure 5.1 shows the event polar angle distribution for selected[1] hadronic events.

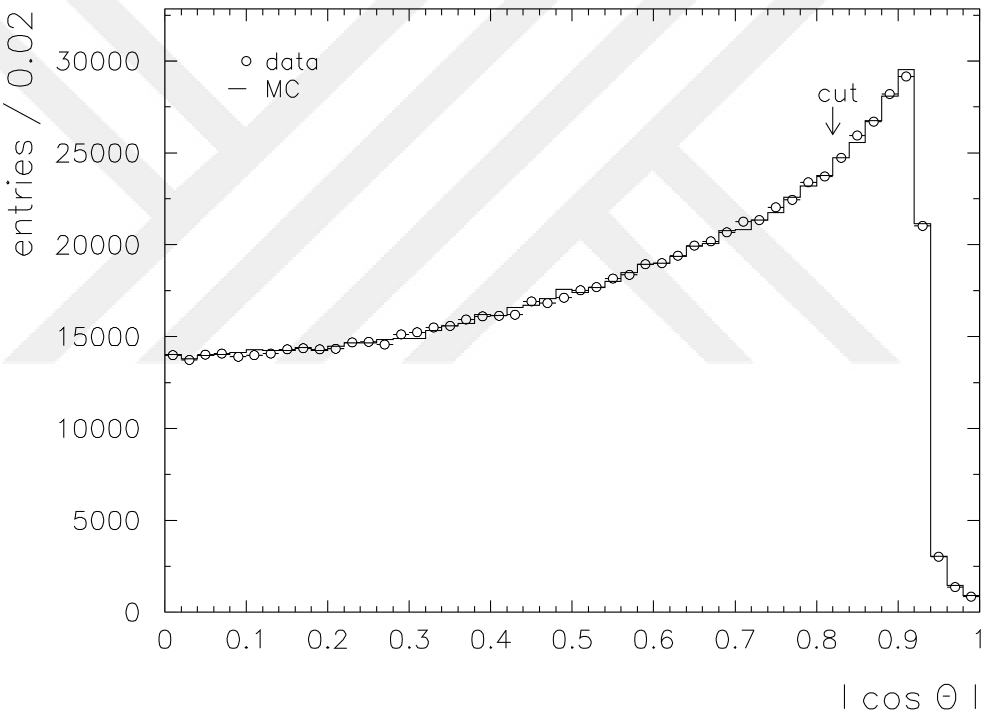

Figure 5.1 Polar angle of the event axis (with respect to the beam axis) as defined by sphericity for selected hadronic events. For event selection the polar angle θ is required to be in the range; $35° < \theta < 145°$ ($|cos\theta| < 0.82$).

The cut ensures that most tracks in an event are well contained within the sensitive regions of the detector and therefore gives rise to a large, well defined,

[1] Here 'selected' means events passing the complete event selection as described in this chapter with the exception of the polar angle cut itself.

acceptance. The sphericity angle cut dominates the efficiency with which hadronic events are selected, reducing the number of hadronic events by 18.6%.

5.2 Hadronic Event Selection

The ALEPH detector records a variety of events, most of which are decays of the Z to its various modes, $\gamma\gamma$ events, and t-channel scattering of electrons. The Z can decay via several channels: Z $\rightarrow q\bar{q}$, Z $\rightarrow \ell^+\ell^-$ and Z $\rightarrow \nu\bar{\nu}$. The reaction Z $\rightarrow q\bar{q}$ is suppressed by the invisible reaction Z $\rightarrow \nu\bar{\nu}$, and so the more species of neutrinos there are, the greater process the Z $\rightarrow q\bar{q}$ is suppressed. Table 5.2 lists the decay modes of the Z [7].

Table 5.2 Dominant decay modes of the Z Boson.

Z Decay Mode	Fraction (%)
e^+e^-	3.363 ± 0.004
$\mu^+\mu^-$	3.366 ± 0.007
$\tau^+\tau^-$	3.370 ± 0.008
hadrons	69.910 ± 0.060
invisible	20.000 ± 0.060

In addition to these there are a small number of background processes such as beam-gas interactions, stray beam electrons, cosmic rays and synchrotron radiation. Figure 5.2 shows the reconstruction of a hadronic sample event in ALEPH detector. The discriminating feature of these type of events is the large multiplicity of visible particles, and the huge fraction of their center-of-mass energy.

Hadronic event selection applied here is that used in the Neutral Vector Meson paper [31] and is typical of the hadronic selection which can be found in many ALEPH QCD papers.

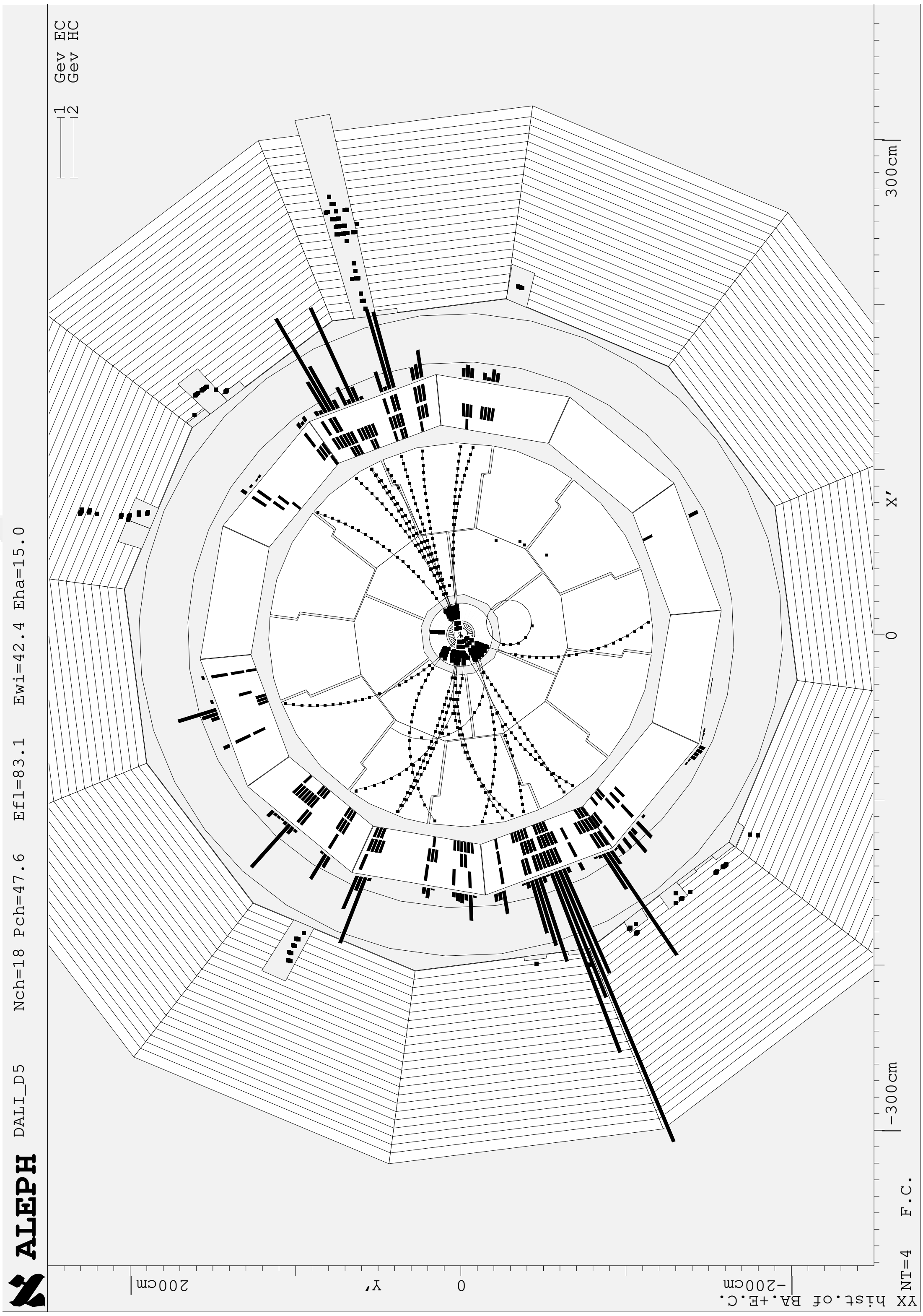

Figure 5.2 Reconstruction of a typical event in hadronic decays at the ALEPH detector. The total reconstructed energy is 83 GeV and the overall charged components are 48 GeV computed from 18 selected tracks in this event.

5.2.1 Track Cuts

Hadronic events are selected on the basis of the total charged multiplicity and energy within an event. For this, cuts are applied to select 'good' charged tracks, removing some badly reconstructed tracks and ensuring track momenta are well measured and that the tracks originate from the interaction point. This gives rise to a more reliable estimate of the total charged multiplicity and energy and a reasonable agreement with the Monte Carlo.

The selection of 'good' charged tracks is as follows. A track must have:

- at least 4 TPC coordinates
- a polar angle in the range $20° < \theta < 160°$
- a transverse impact-parameter $|d_0| < 2\,\mathrm{cm}$
- a longitudinal impact-parameter $|z_0| < 5\,\mathrm{cm}$
- a momentum $p_t > 200\,\mathrm{MeV}/c$.

After all these cuts the ratio Monte Carlo / real data for the number of tracks selected is 1.0042 ± 0.0002. This agreement illustrates the global tuning of JETSET to fit the ALEPH data. The distributions of the track cuts are shown in Figures 5.3 to 5.6 for selected[1] tracks. The distributions are discussed next.

Number of TPC Coordinates

Figure 5.3 shows the distribution of the number of TPC coordinates for selected tracks. Tracks with no TPC coordinates are those reconstructed only in the ITC, such tracks tend to have a poorly measured z component of their momentum vector. A cut of at least 4 TPC hits provides a starting point for the selection of 'good' charged tracks.

[1] Here 'selected' means tracks passing all other track cuts and events are selected as described in Section 5.1.

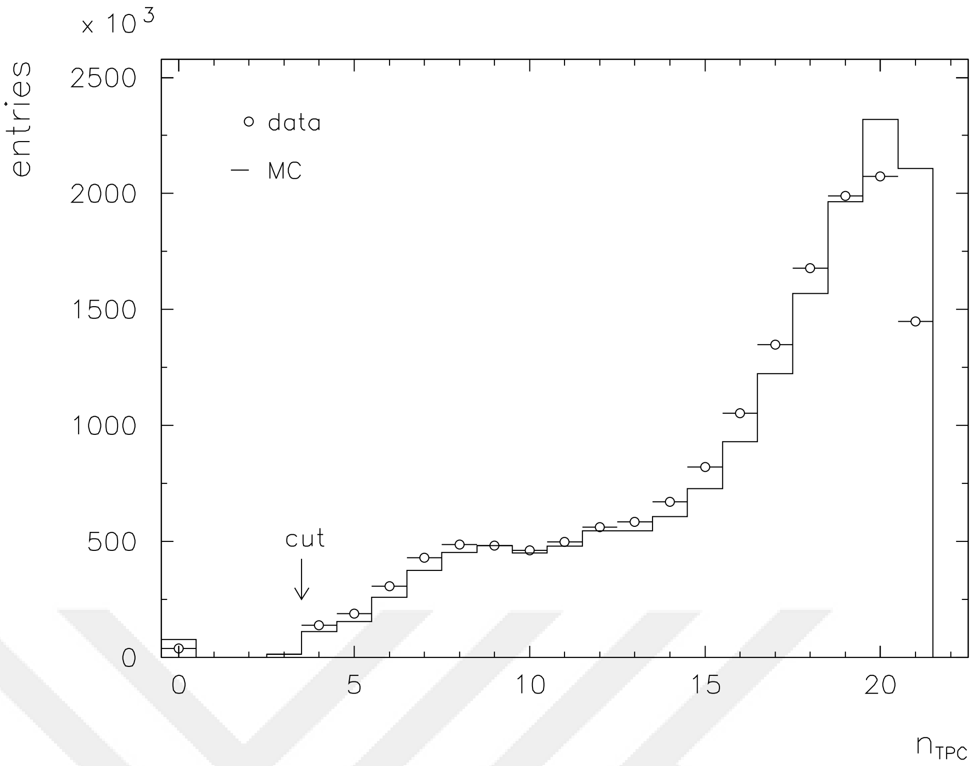

Figure 5.3 Number of TPC coordinates for selected tracks.

Polar Angle

Figure 5.4 shows the distribution of the polar angle for selected tracks. The cut is mostly redundant but removes the few tracks whose momentum resolution is very poor due to a small path length in the xy plane of the TPC.

Impact Parameters

Whilst hadronic events typically have a high charged multiplicity, background events normally of low multiplicity can gain additional charged particles, thereby mimicking low multiplicity hadronic events, due to a variety of processes. These processes involve interactions with the material of the detector such as nuclear interactions, photon conversions, back-scatter of particles from the ECAL. Tracks can also be gained by the failure to link successive turns of spirals, the decay of charged tracks, the return of spiraling tracks into the TPC, and 'imaginary' tracks constructed by JULIA from bad or incorrectly assigned TPC hits. These processes usually result in tracks which do not point back to the interaction point, thus their effects can be minimised by making cuts on the track impact parameters d_0

and z_0.

Figures 5.5 and 5.6 show the distribution of the impact parameters for selected tracks. The cuts are loose (Figures 5.5b and 5.6b) allowing tracks originating from decays away from the interaction point, for example B meson decays, to be selected. Figures 5.5c and 5.6c show the ratio real data / Monte Carlo for the distributions. The Monte Carlo has a tighter distribution for both d_0 and z_0. For the d_0 cut the real data initially selects $\approx 5\%$ less tracks in the ± 0.05 cm region, an excess is seen for larger values of d_0 and by $|d_0| = 0.5$ cm the number of tracks in the Monte Carlo compared to the number in the real data agrees to $\approx 0.7\%$, by $|d_0| = 2.0$ cm the agreement is $\approx 0.1\%$. The z_0 distribution shows a similar behaviour though this is less sensitive due to its much wider distribution.

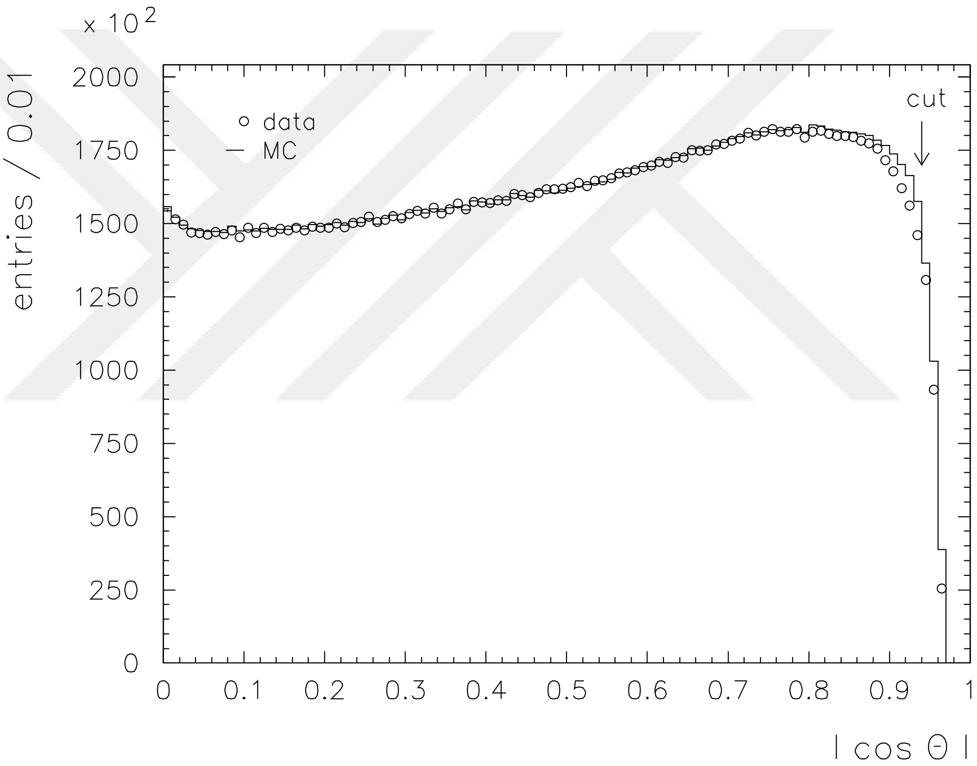

Figure 5.4 Polar angle for selected tracks.

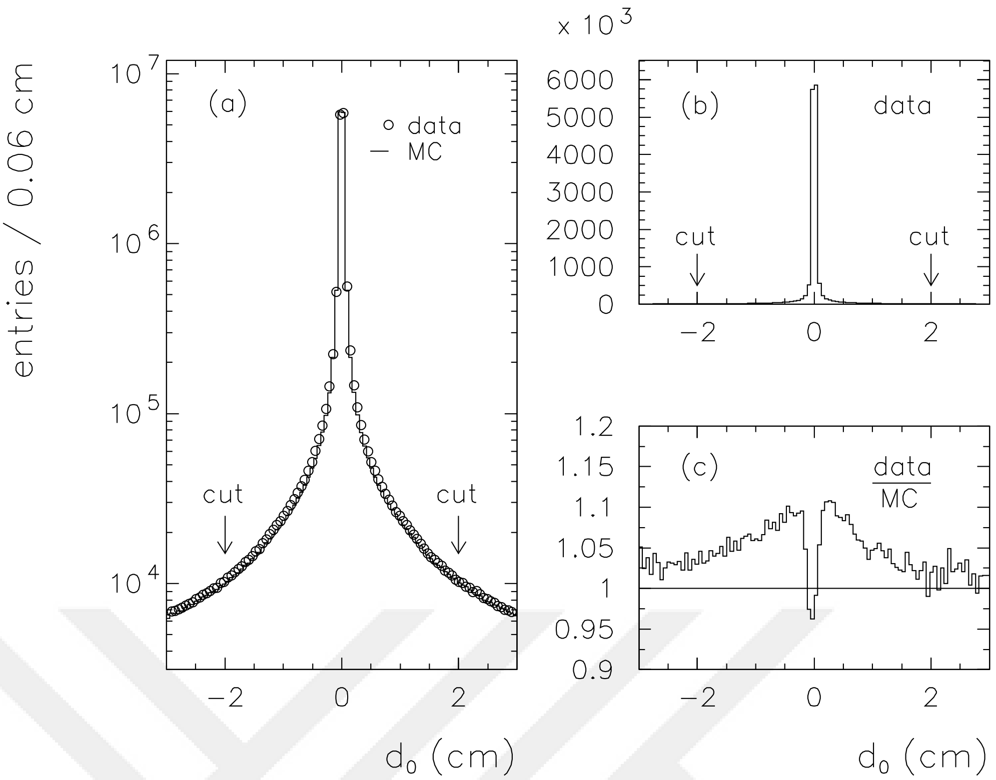

Figure 5.5 Transverse impact parameter for selected tracks. (a) Monte Carlo and real data compared: the distribution in real data is wider than that in the Monte Carlo. (b) The cut of 2 *cm* is loose allowing tracks from heavy flavour decays away from the interaction point to be selected. (c) the ratio real data / Monte Carlo shows the wider distribution in the real data.

Transverse Momentum

Figure 5.9 shows the distribution of the transverse momentum for selected tracks. Applying a p_t cut of 200 MeV/c removes tracks which turn tightly in the TPC. Since such tracks do not transverse many TPC pad rows, they therefore suffer from a poor momentum resolution.

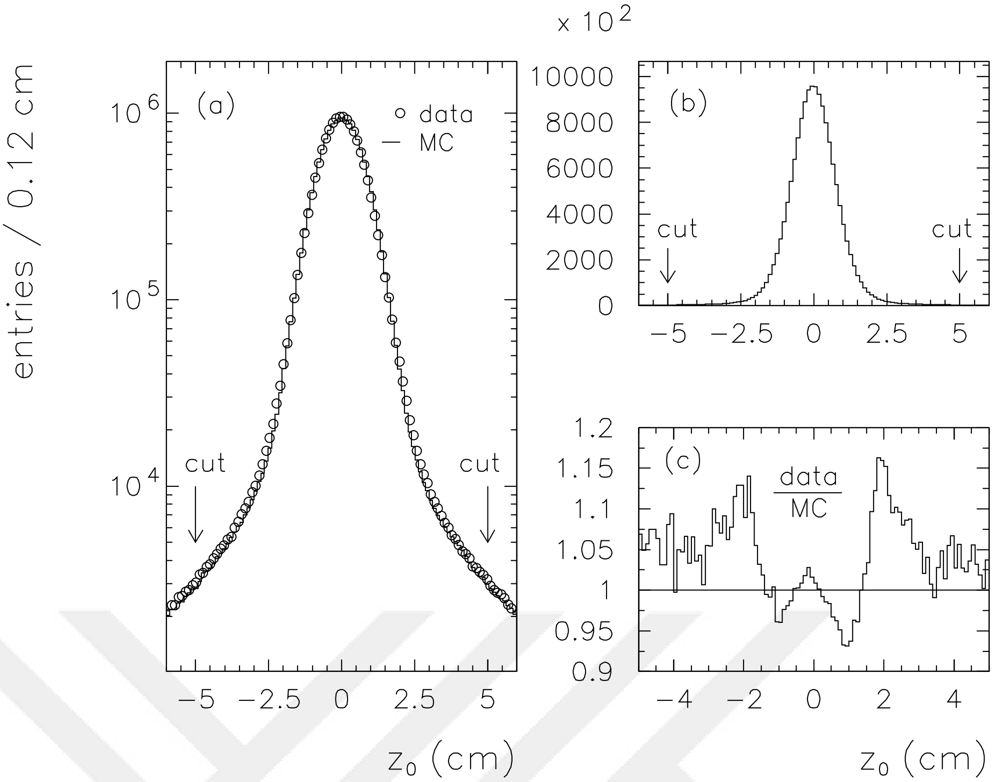

Figure 5.6 Longitudinal impact parameter for selected tracks. Figures (a), (b) and (c) follow the same form as Figure 5.5. The ratio real data / Monte Carlo shows the wider distribution in the real data. The cut is loose reducing the effect of the discrepancy.

5.2.2 Event Cuts

Figure 5.7 shows the event charged energy[2] versus the event charged multiplicity for events in the real data after applying the event sphericity angle cut. A clear separation of the hadronic event types can be seen. The hadronic signal is selected with an efficiency of 94.9% and a purity of 99.6% by requiring events to have:

- a minimum of 5 'good' charged tracks, and
- a minimum of 15 GeV total 'good' charged energy.

The track multiplicity cut removes Z $\rightarrow l\bar{l}$ events. Most $\gamma\gamma$ events are removed with the event polar angle cut, the rest are removed by the charged energy cut. Figures 5.8a and 5.8b show a good agreement between Monte Carlo and real data

[2] The pion mass is assumed for all charged tracks.

for the charged energy and multiplicity distributions for the selected events[3] . All event selection criterias has been summarised in Figure 5.10.

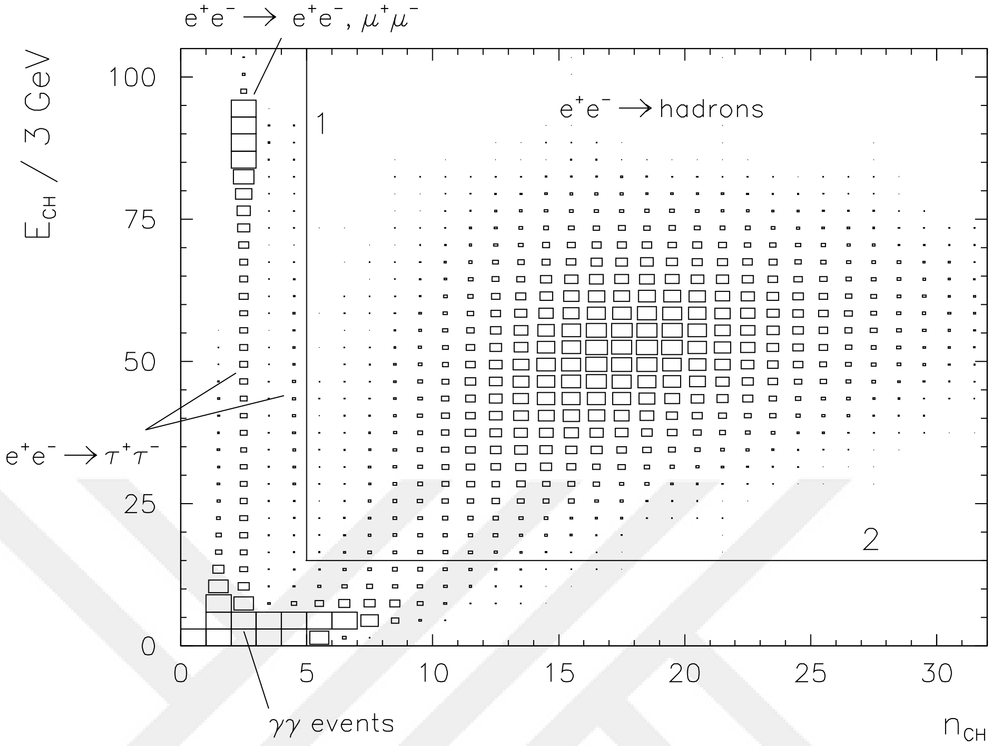

Figure 5.7 Charged energy, E_{CH}, versus charged multiplicity, n_{CH}, for events in real data after 'good' charged track and event polar angle cuts have been applied. The hadronic signal is selected by requiring at least 5 good charged tracks (cut 1) and a charged energy of at least 15 GeV (cut 2).

[3] A good agreement is expected as the tuning of the Monte Carlo relies to a great extent on measurements in the real data of charged track distributions.

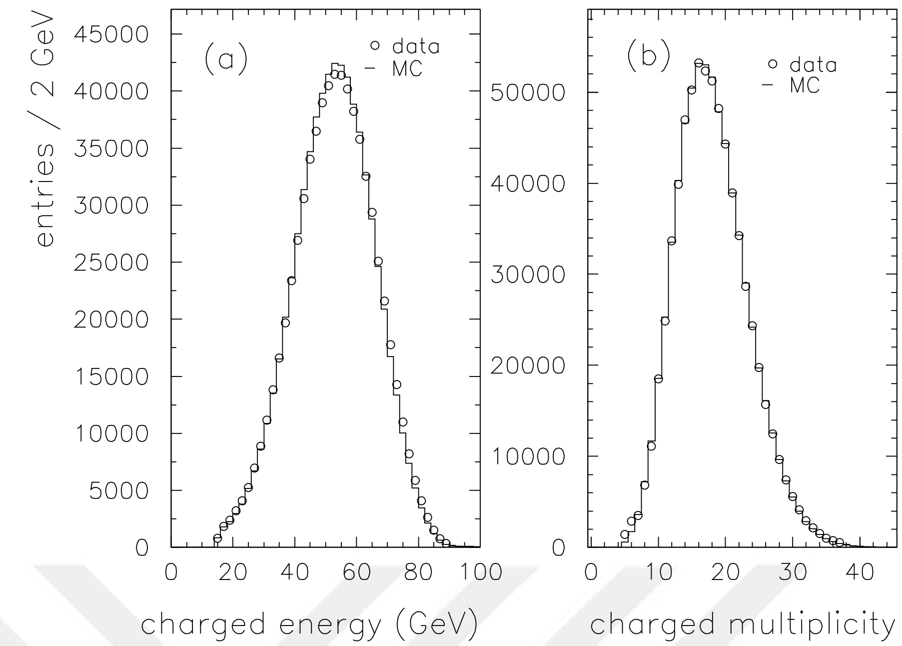

Figure 5.8 Charge distributions for selected events, a) charged energy, and b) charged multiplicity. The Monte Carlo is in good agreement with the real data.

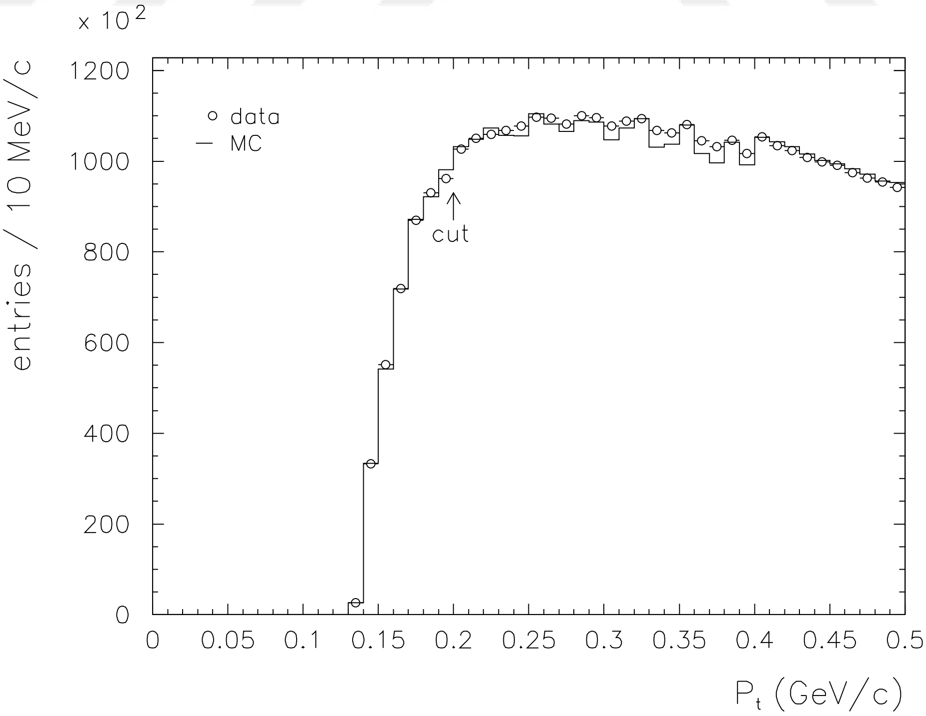

Figure 5.9 Transverse momentum for selected tracks. a cut of 200 MeV/c is applied to ensure a reasonable momentum resolution.

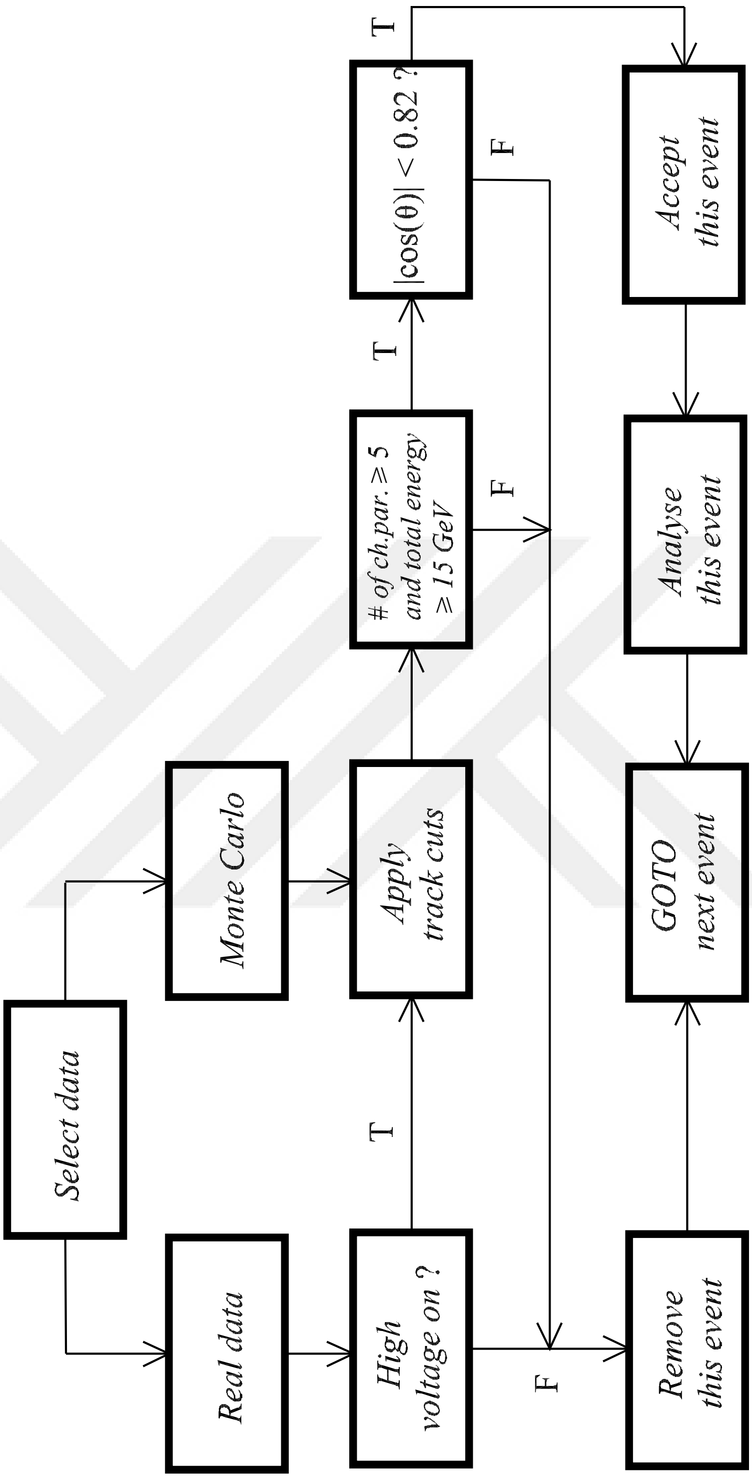

Figure 5.10 Flow chart of hadronic event selection.

5.3 Event Background

The level of background after event selection is dominated by tau events with a small contribution from $\gamma\gamma$ events. Background from other processes such as decays of the Z to e^+e^- and $\mu^+\mu^-$, t-channel scattering of beam electrons, beam-gas, and cosmic rays are much smaller [32]. From Monte Carlo studies the contributions to the selected events are given in Table 5.3.

Table 5.3 The contributions of the hadronic and background events obtained from Monte Carlo.

Selected event	Contribution in %
Hadronic	99.625 ± 0.001
Tau	0.325 ± 0.002
$\gamma\gamma$	0.050 ± 0.004

Note that, without the cut on the event angle, the contribution from $\gamma\gamma$ events would be comparable with that from tau events.

CHAPTER 6

PARTICLE SELECTION FOR THE ANALYSIS

6.1 Introduction

Particle identification is important to reduce the combinatorial background in physics analysis. In this chapter, the selection of charged particles and neutral pions for the analysis of D^{*0} mesons, in decay channel $D^{*0} \to D^0\pi^0$, is described, where D^0 is reconstructed from $D^0 \to K^-\pi^+$ [1] and $\pi^0 \to \gamma\gamma$. The selection of charged tracks is relatively trivial, while neutral pion selection and reconstruction is much more complicated. All selection performances are determined from simulation studies with the aim of maximising the product of *purity* and *efficiency*. In the calculations, natural units are used such that $h = c = 1$.

6.2 Charged Track Selection

The charged track selection for the analysis involves cuts on the same parameters as in the track selection for event selection. The polar angle and TPC coordinate multiplicity cuts are kept the same. The impact-parameter cuts are tightened considerably to increase the purity of selected charged tracks originating from D^0 decays. A small increase in the momentum cut is introduced to improve the agreement in the impact parameter distributions and remove poorly measured tracks. Additionally, two cuts are applied to the χ of ionisation energy loss, dE/dx, so as to remove some electron and proton backgrounds. The charged track selection for the analysis is as follows:

- a transverse impact-parameter $|d_0| < 0.5$ cm
- a longitudinal impact-parameter $|z_0| < 2.0$ cm

[1] The anti particle is reconstructed from $\bar{D^0} \to K^+\pi^-$

- a momentum $p_\pi > 0.5\,\text{GeV}$ and $p_K > 1\,\text{GeV}$
- if available, $|\chi(\text{dE/dx})| < 3$ (with both π and K hypotheses)

After all these cuts the ratio of Monte Carlo to real data for the number of tracks selected is 1.0101 ± 0.0002. The details of applying the cuts are described in the following sections.

6.2.1 Impact Parameters

Tight cuts on the impact parameters are introduced to increase the reconstructed purity of tracks from D^0 mesons. According to Monte Carlo Simulation studies, the hard cuts $|d_0| = 0.5$ cm and $|z_0| = 2.0$ cm remove significant number of electron, muon and pion backgrounds from K_s^0 decays. Based on the definitions given in the previous chapter, Figure 6.1 and Figure 6.2 shows d_0 and z_0 distributions respectively. About 1% of daughter particles from $D^0 \to K^-\pi^+$ decay are lost by applying these cuts.

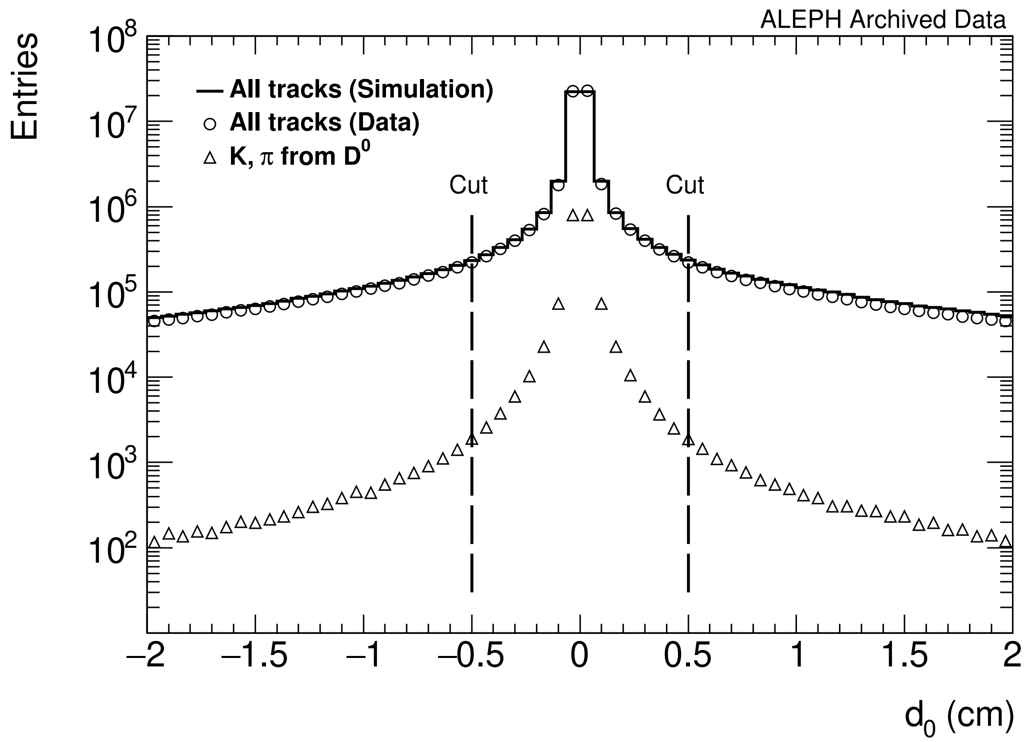

Figure 6.1 Transverse impact parameters distributions for reconstructed tracks from $D^0 \to K^-\pi^+$ decay. Dashed lines represent the cut applied.

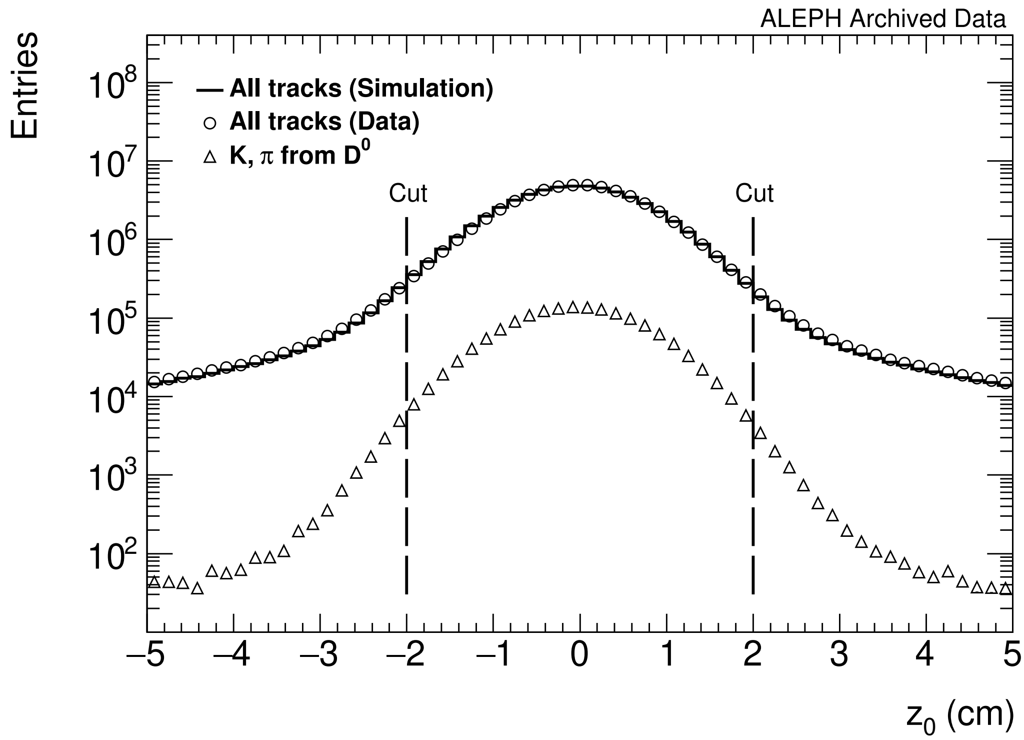

Figure 6.2 Longitudinal impact parameter distributions for reconstructed tracks from $D^0 \to K^-\pi^+$ decay. Dashed lines represent the cut applied.

6.2.2 Momentum

The cut on the momentum for tracks is increased from 0.2 GeV to 0.5 GeV for π and to 1 GeV for K as shown in Figure 6.3. This increment improves the average reconstructed momentum resolution (see Section 6.5.4) and the agreement between Monte Carlo and real data for the impact parameter distributions.

6.2.3 Ionisation Energy Loss

Charged particle identification is performed by the measurement of ionisation energy loss, dE/dx. A particle's energy loss is sampled in the TPC by up to 338 wires. The deviation from an assumed hypothesis is defined as $\chi(\mathrm{dE/dx})$:

$$\chi(\mathrm{dE/dx}) = \frac{(\mathrm{dE/dx})_{\mathrm{measured}} - (\mathrm{dE/dx})_{\mathrm{expected}}}{\sigma_{\mathrm{dE/dx}}} \tag{6.1}$$

where $\sigma_{\mathrm{dE/dx}}$ is the expected dE/dx resolution normalised with a sample of minimum ionising tracks. Note that, not all charged tracks have dE/dx information. Figure 6.4 shows the measured dE/dx as a function of particle momentum for charged particles.

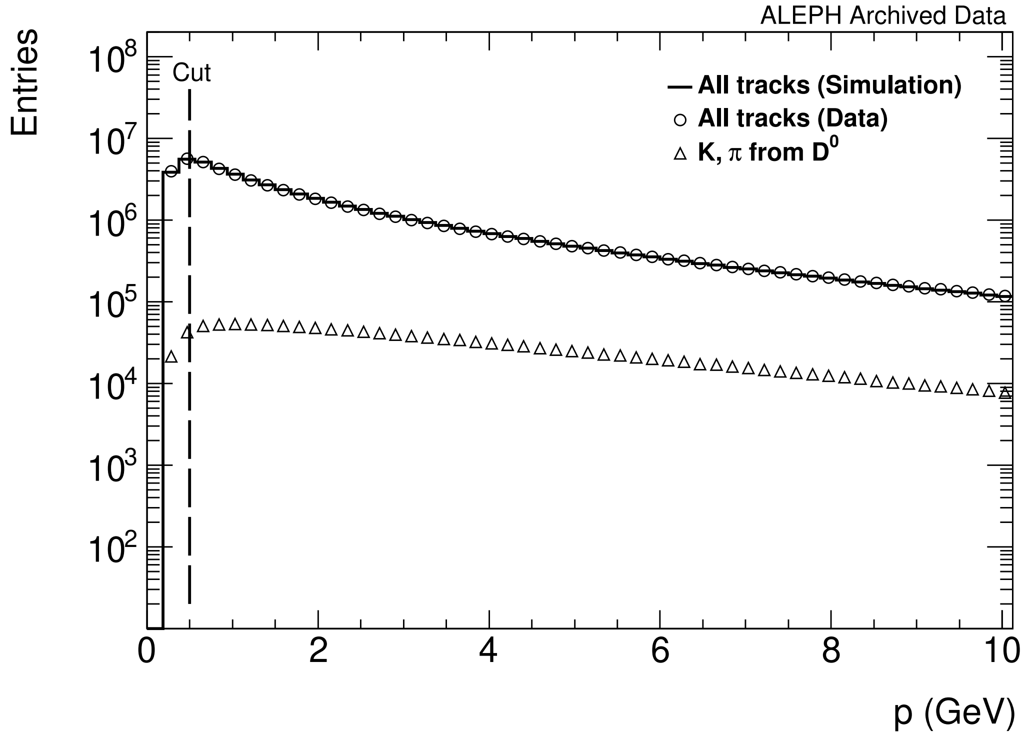

Figure 6.3 Momentum distribution for reconstructed tracks, and particles from $D^0 \to K^-\pi^+$ decay. Dashed line represents the cut applied for $K^\pm$.

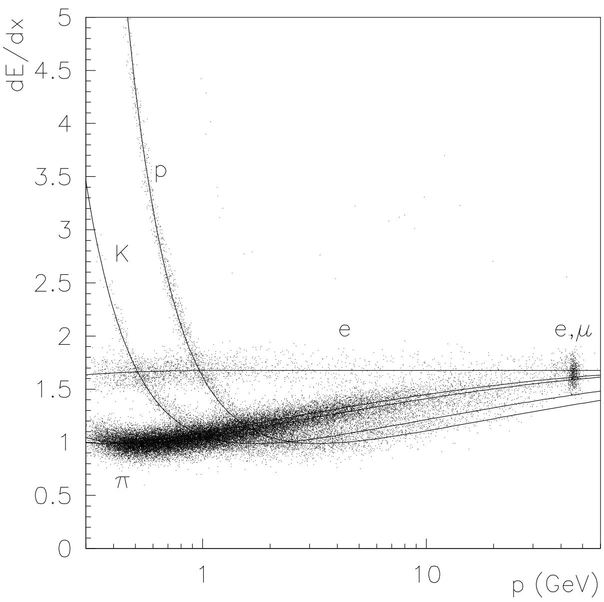

Figure 6.4 Measured dE/dx as a function of momentum for electrons, muons, poins, kaons and protons.

Figure 6.5 a and b show χ(dE/dx) distributions of all charged particles for Monte Carlo and real data according to the π and K hypotheses[2] respectively. If available, charged particles satisfying $|\chi(\text{dE/dx})| < 3$ are selected for the analysis. Together, the cuts applied on momenta, impact parameters and χ(dE/dx) value allow us to select tracks from D^0 mesons with 91% efficiency.

6.3 π^0 Selection

Neutral pions decay to two photons ($\pi^0 \to \gamma\gamma$) with a branching ratio of $98.798 \pm 0.032\%$ [7]. For this analysis, photons[3] are reconstructed using the ECAL. π^0 candidates are selected from invariant mass distributions of photon pairs using the equation

$$m^2 = 2E_1E_2(1 - \cos\theta_{12}) \tag{6.2}$$

where m is the invariant mass of the reconstructed photons whose energies are E_1 and E_2, and θ_{12} is the angle between two photons. In the physics analysis, unconverted photons with an energy greater than 0.5 GeV are selected. If π^0 candidates are true they form a signal, or false, they can form a background as shown in Figure 6.6. In order to minimise systematic uncertainties, pion candidates are selected within a large mass window range, $0.05 \text{ GeV} < m(\gamma, \gamma) < 0.25 \text{ GeV}$. Simulation studies show that the mass window selection efficiency is about 99.4%.

The lower energy bound for π^0 candidates is 1 GeV, i.e. twice the photon energy cut. An upper bound of 10 GeV is applied to reduce the combinatorial background at high energies. Energy distribution of π^0 is shown in the Figure 6.7.

6.4 D^0 Selection

D^0 candidates are reconstructed from the decay channel $D^0 \to K^-\pi^+$ and selected within the mass window between 1.83 GeV and 1.90 GeV, with efficiency about 96.9%, as shown in Figure 6.8.

---

[2] i.e. for pions, the mass of charged pion is assigned to all charged particles.

[3] Photons converting to e^+e^- pair within the material of the detector, 7% on average, are not selected.

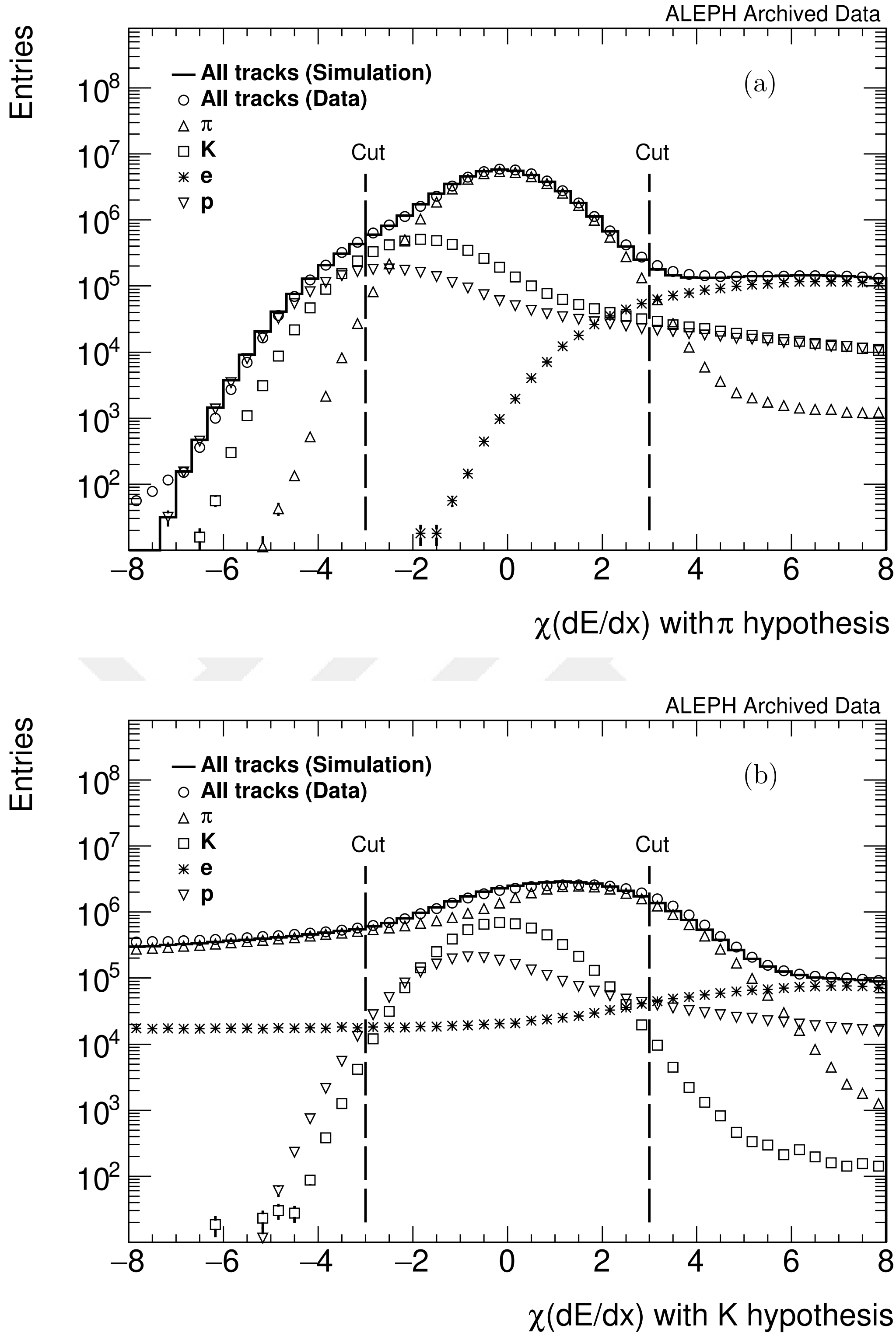

Figure 6.5 χ(dE/dx) distributions according to (a) π hypothesis and (b) K hypothesis. Dashed lines represent the cut applied.

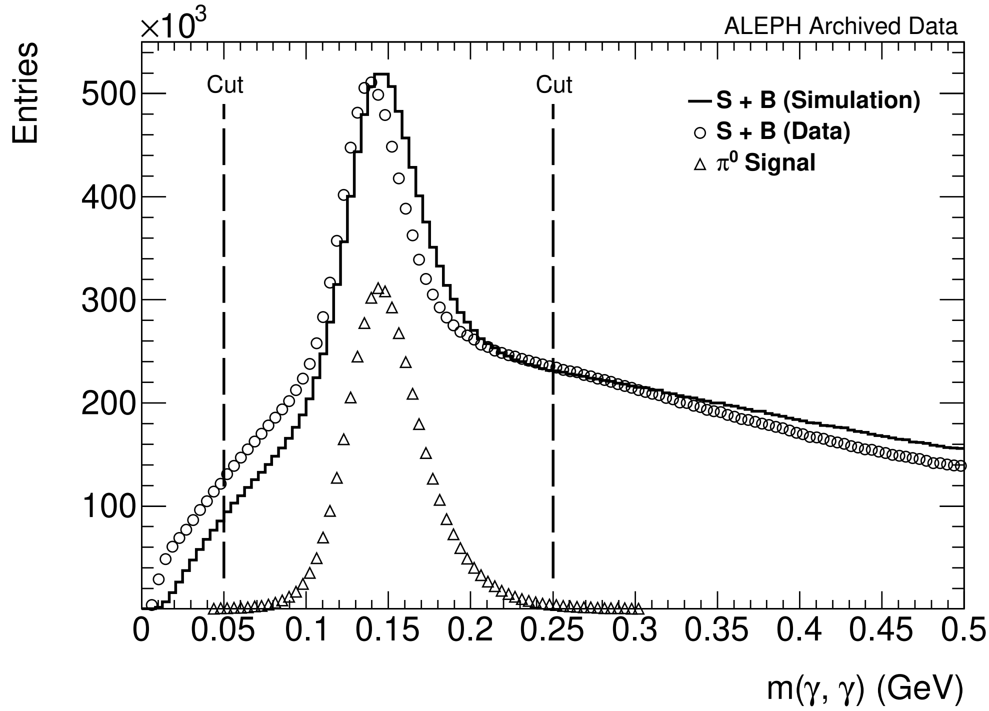

Figure 6.6 An example of the invariant mass of photon pairs around a π^0 peak. Photon pairs that produces a correct combination results in a π^0 signal peak. Dashed lines represent the selection of mass window. S + B abbreviation corresponds to distribution of Signal and Background summation.

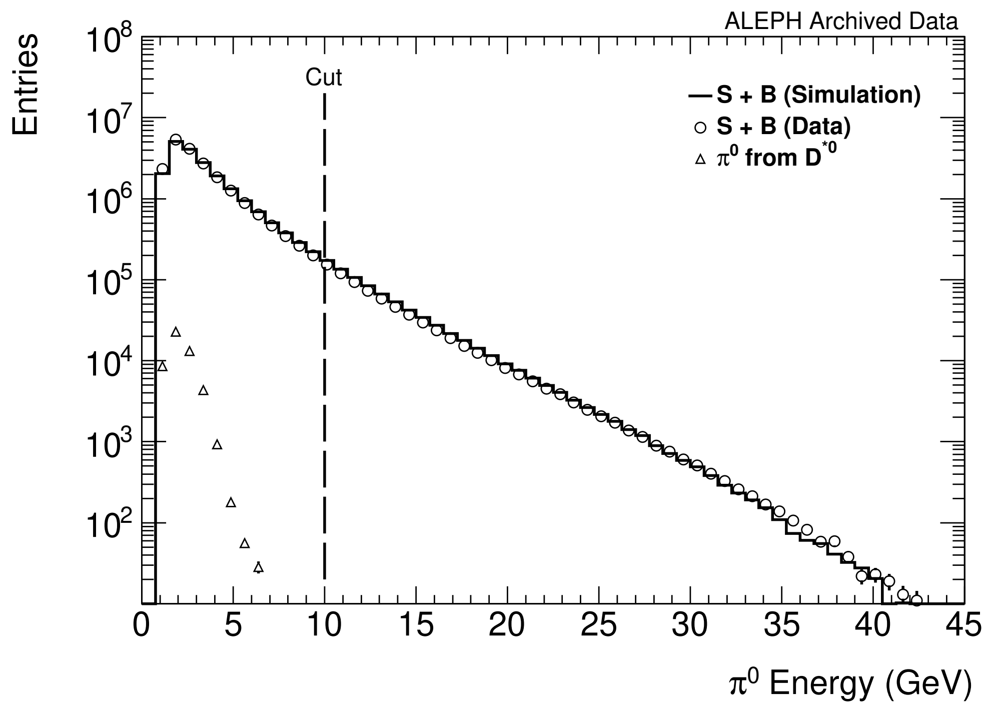

Figure 6.7 Energy distribution of π^0 candidates.

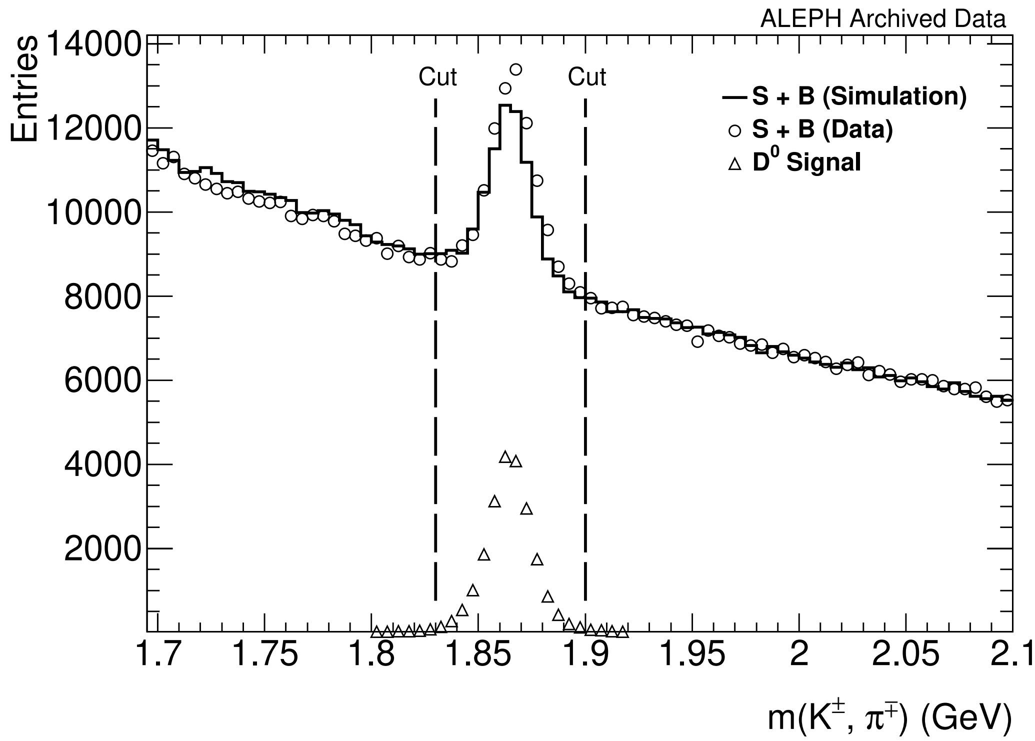

Figure 6.8 Invariant mass of $K^{\pm}$ $\pi^{\mp}$ combinations around a D^0 peak. Combinations of correct track pairs produces a peak of D^0 signal.

After initial mass window selection, momentum cut, $p_{D^0} > 12$ GeV, is applied for D^0 candidates. Another cut known as $\cos\theta^*$ which represents cosine of the angle between D^0 and its daughter particle kaon measured in D^0 rest frame is also applied. Distribution is uniform for the signals while it peaks at 1 for the background. Figure 6.9 shows the $\cos\theta^*$ distribution for D^0 candidates where the cut $|\cos\theta^*| < 0.8$ is found to be optimum in the analysis in order to reduce the combinatorial background.

6.5 Reconstruction Performances

Details of reconstruction efficiency, purity and momentum resolution have a direct effect on the reconstructed D^{*0} signal significance. Reconstruction performances for selected particles are determined from Monte Carlo studies. Some distributions are presented in the following subsections.

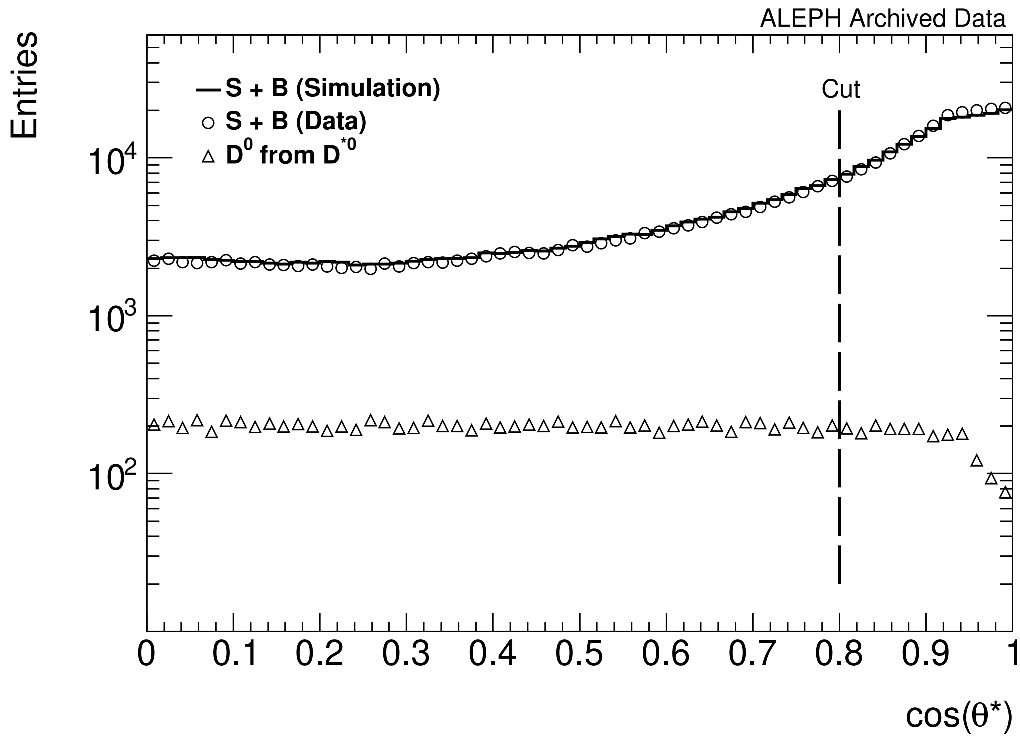

Figure 6.9 $\cos\theta^*$ distribution. Dashed line represents the cut applied.

6.5.1 Momentum Distributions

The momentum spectra of generated and reconstructed tracks ($K^\pm$ and $\pi^\pm$) and π^0 are given in Figure 6.10 and Figure 6.12 respectively. The distributions help us to form the purity and efficiency of daughter particles.

6.5.2 Purity

The purity, $\mathcal{P}$, of the selected charged tracks ($K^\pm$ and $\pi^\pm$) and π^0 are defined as follows:

$$\mathcal{P}_{(K^\pm,\pi^\pm)} \equiv \frac{\text{number of reconstructed good charged tracks matched to } (K^\pm \text{ or } \pi^\pm)}{\text{number of reconstructed good charged tracks}}$$

$$\mathcal{P}_{\pi^0} \equiv \frac{\text{number of reconstructed } \pi^0 \text{ candidates matched to } \pi^0}{\text{number of reconstructed } \pi^0 \text{ candidates}}$$

Figure 6.11 and 6.13 respectively illustrate the purity of the selected charged tracks and neutral pions.

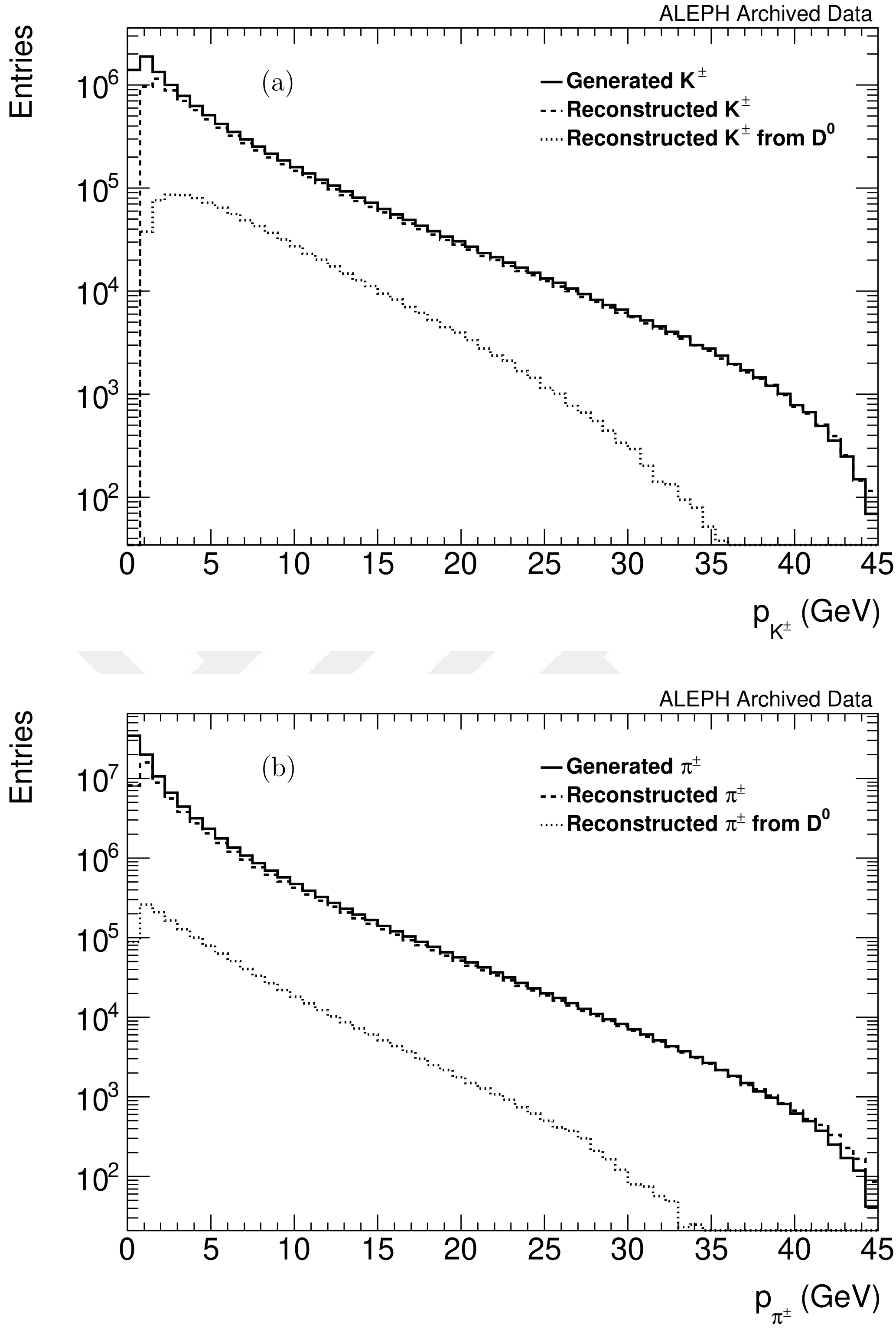

Figure 6.10 Momentum distributions of charged tracks (a) $K^{\pm}$ and (b) $\pi^{\pm}$.

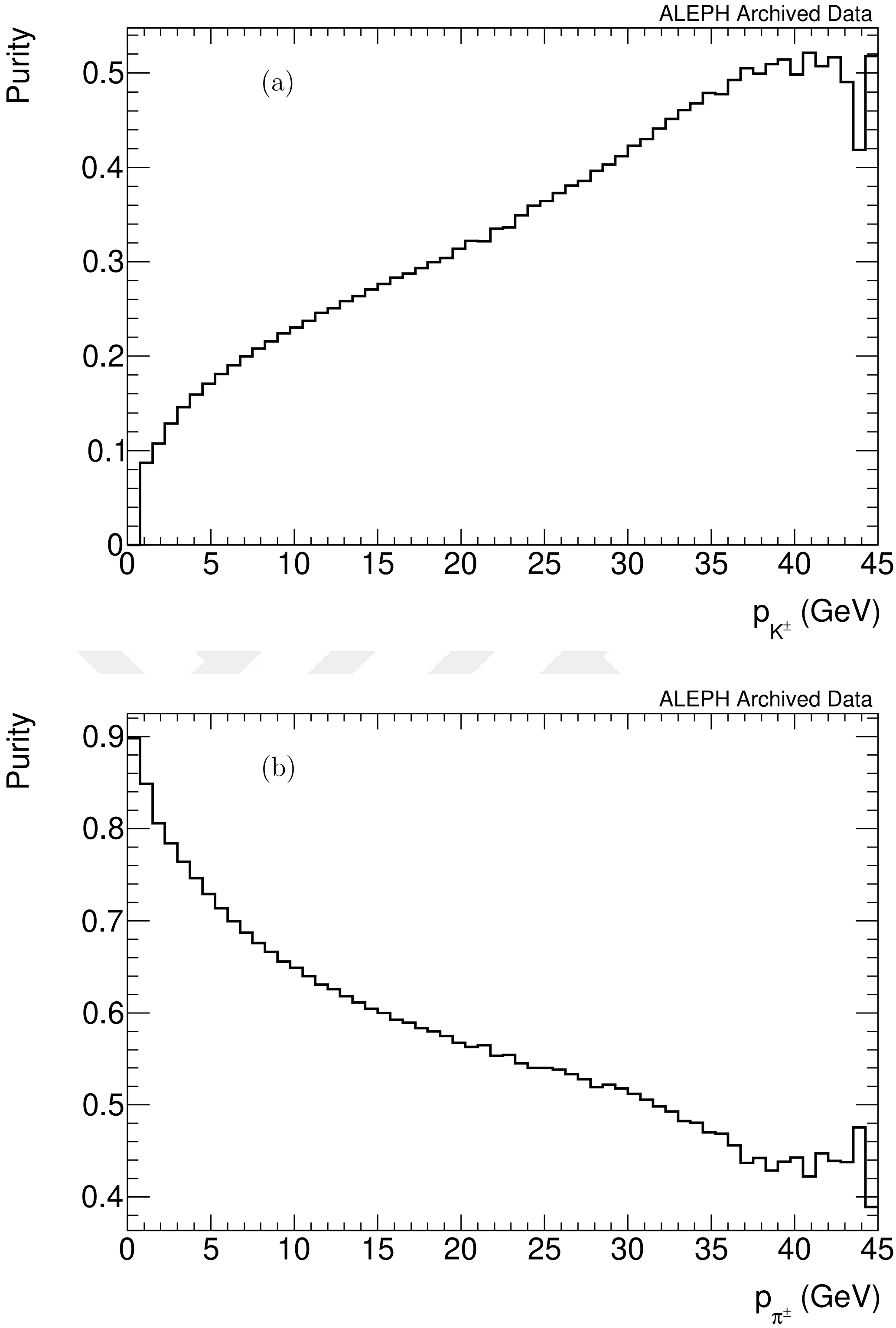

Figure 6.11 Purity of reconstructed charged tracks (a) $K^{\pm}$ and (b) $\pi^{\pm}$ as a function of momentum.

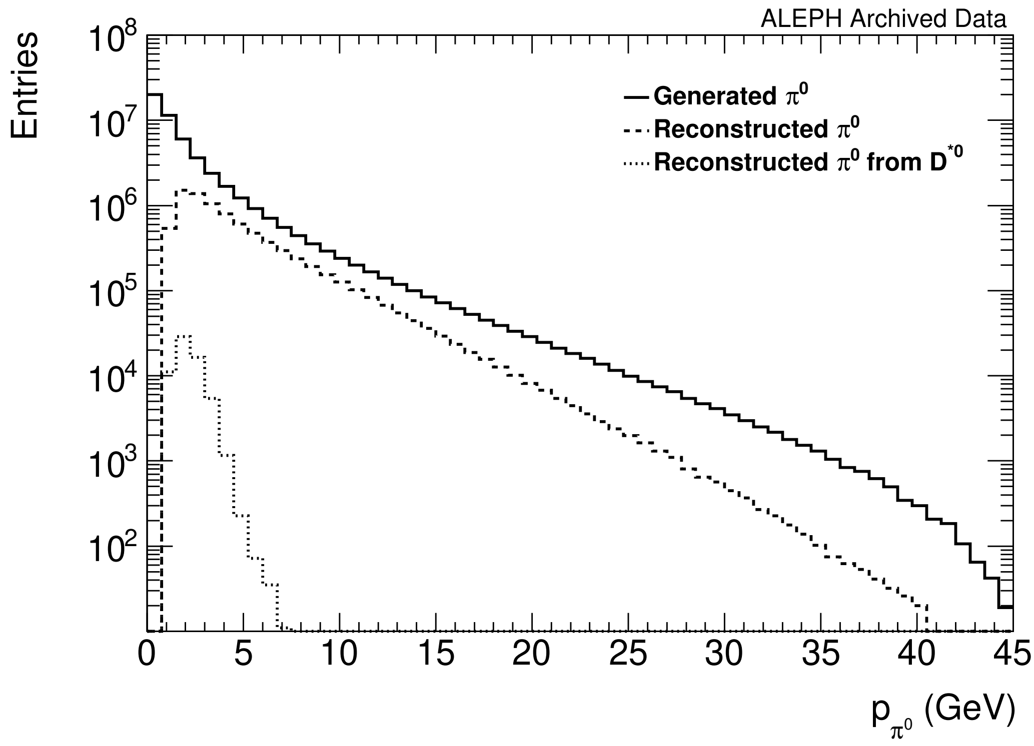

Figure 6.12 Momentum distributions of π^0.

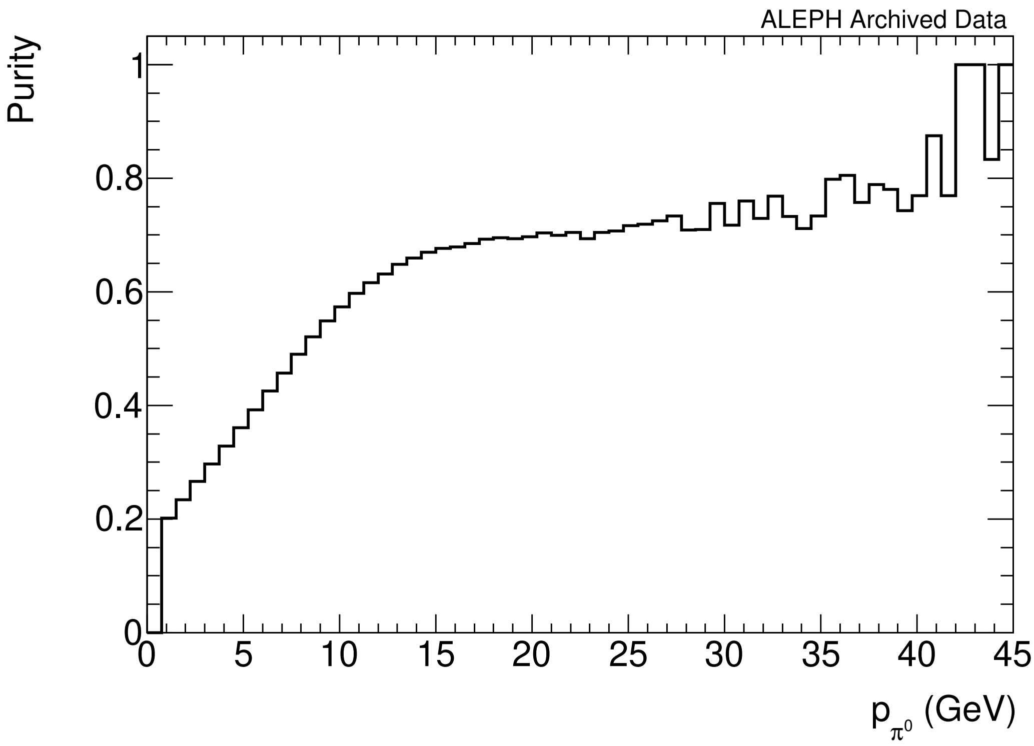

Figure 6.13 Purity of all reconstructed π^0 candidates as a function of momentum.

6.5.3 Efficiency

The selection efficiency, $\mathcal{E}$, of charged tracks and π^0 can be defined as follows:

$$\mathcal{E}_{(K^\pm,\pi^\pm)} \equiv \frac{\text{number of reconstructed good charged tracks matched to } (K^\pm \text{ or } \pi^\pm)}{\text{number of } K^\pm \text{ and } \pi^\pm \text{ generated at the truth level}}$$

$$\mathcal{E}_{\pi^0} \equiv \frac{\text{number of reconstructed } \pi^0 \text{ candidates matched to } \pi^0}{\text{number of } \pi^0 \text{ generated at the truth level}}$$

The selection efficiency for charged tracks and π^0 are shown in Figure 6.14 and Figure 6.15 respectively. Note that, the efficiency at high energies is grater than one. This is because the poor momentum resolution of reconstructed tracks results in bin to bin migrations.

6.5.4 Momentum Resolution of tracks

The momentum resolution, σ_p, for charged particles, is measured from the Monte Carlo studies and defined as the 'half width at half maximum' for the distribution p_{rec}/p_{tru}. The residual, δ_p , is defined as the displacement of the peak of the distributions from one. The results are shown in Figure 6.16. Resolution is worse at high momentum because the tracks become very straight, and at low momentum due to scattering of the particle with the gas in the TPC.

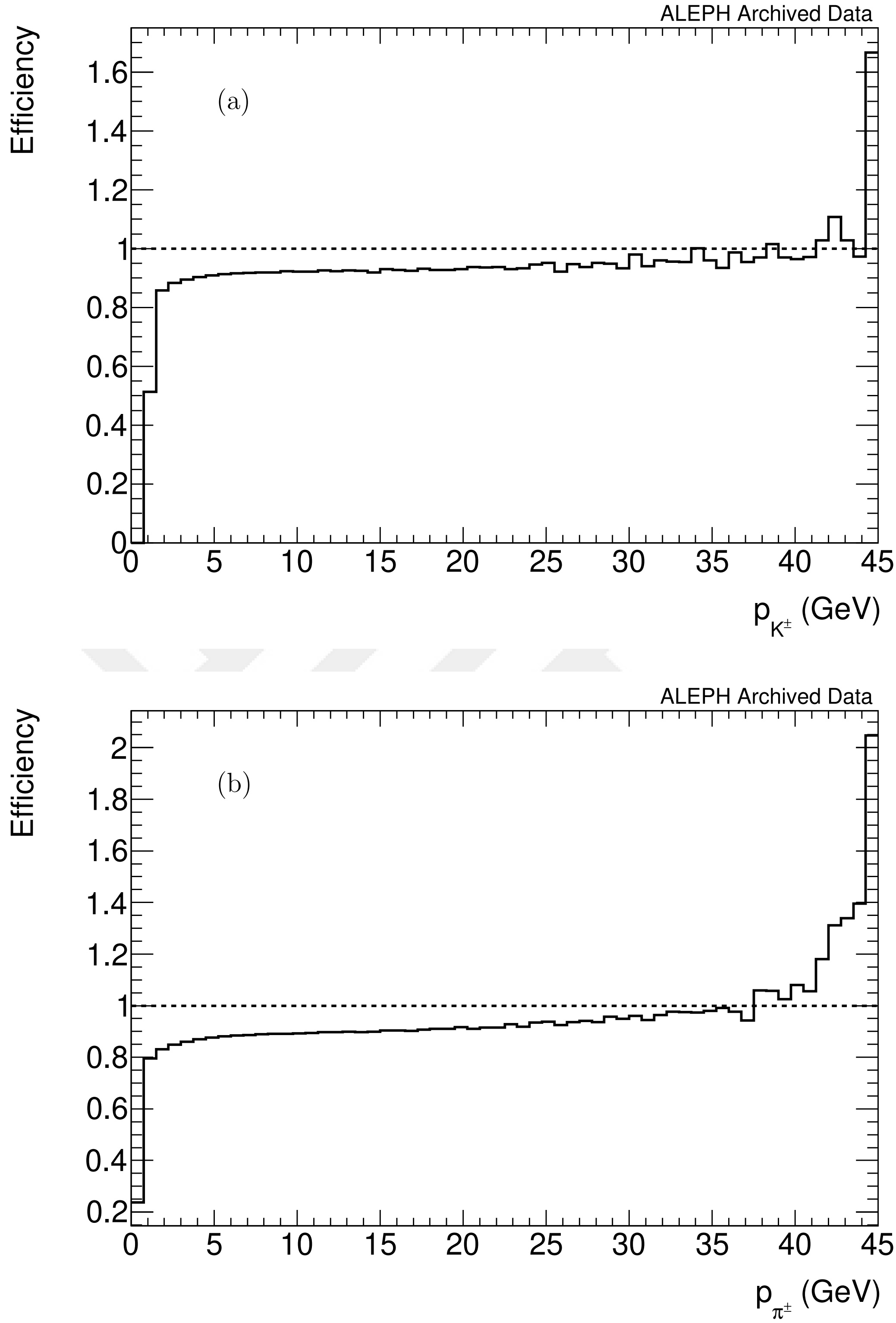

Figure 6.14 Efficiency of reconstructed charged tracks (a) $K^{\pm}$ and (b) $\pi^{\pm}$ as a function of momentum.

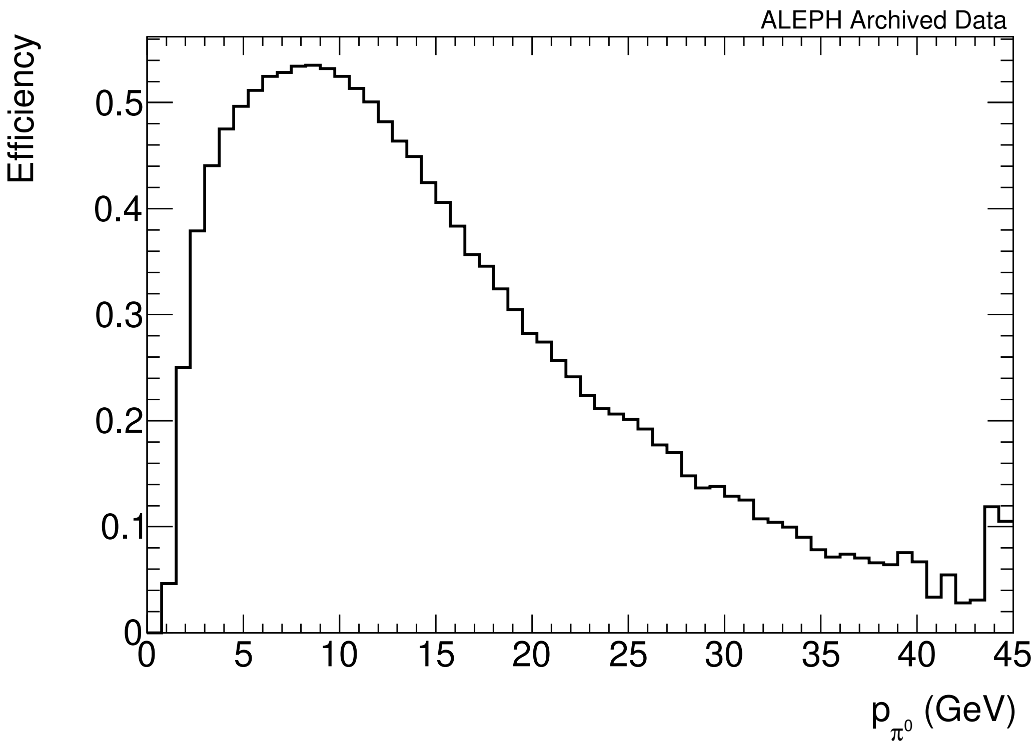

Figure 6.15 Efficiency of all reconstructed π^0 candidates as a function of momentum.

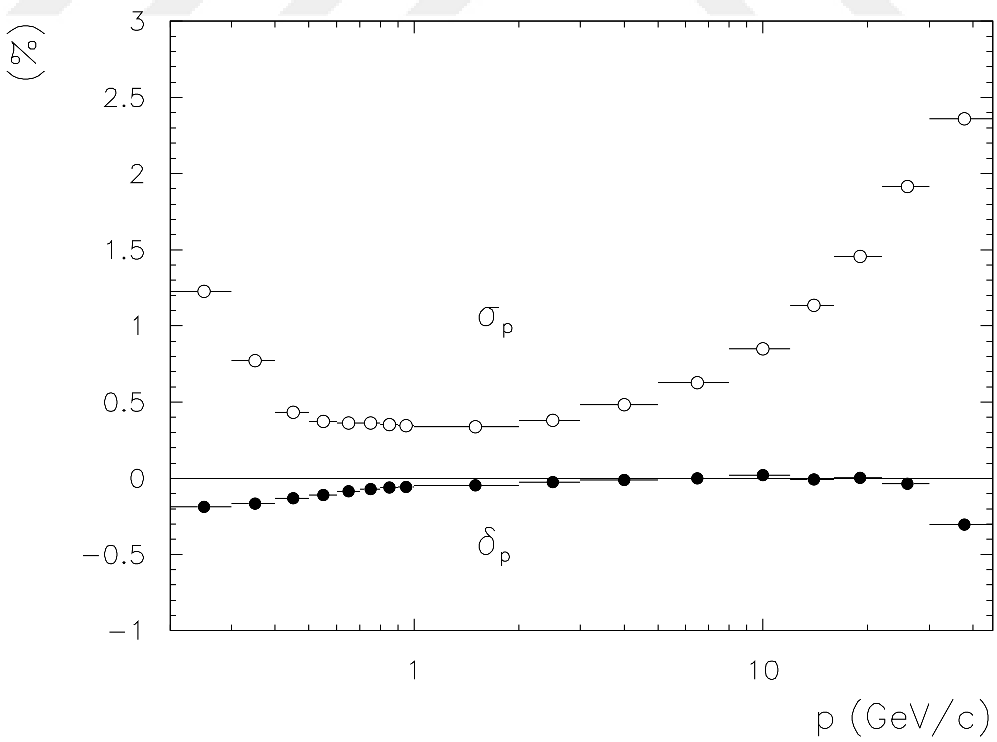

Figure 6.16 Measured momentum resolution, σ_p, and residuals, δ_p, as a function of momentum for all reconstructed charged particles.

6.6 Mass Constraint

Uncertainties in the reconstructed momentum vector of a π^0 are introduced due to the finite ECAL spatial and energy resolution. By making use of the relation:

$$m_r^2 = 2E_1E_2\left(1 - \cos\theta_{12}\right) \tag{6.3}$$

relating the reconstructed π^0 mass m_r to the reconstructed photon energies E_1 and E_2 and their opening angle θ_{12}. In order to improve the momentum resolution of the neutral pions, one can apply a kinematic refit to the momentum vectors of the reconstructed photons. To do that, the momenta of the photons are adjusted such that their invariant mass ideally gives the nominal mass of π^0, 0.135 GeV [33]. Refitted momentum of π^0 leads to a significant increase in the signal significance.

Figure 6.17 shows distribution of momentum difference between generated and reconstructed π^0 candidates. It is clear that mass constraint improves momentum resolution, defined as the width of the distribution.

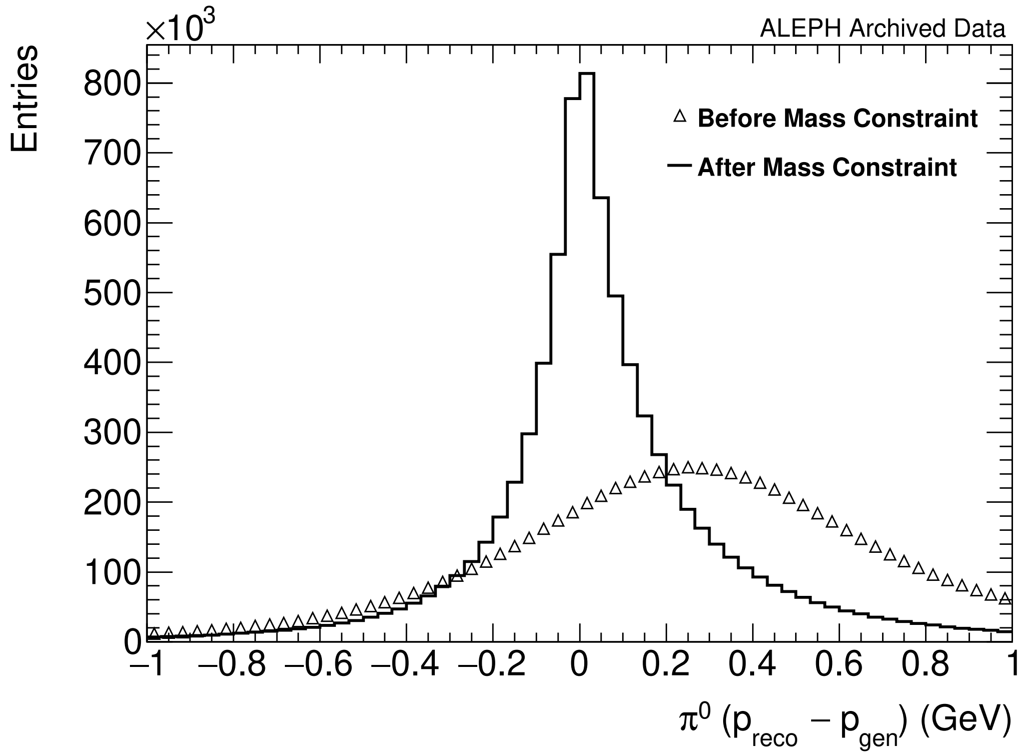

Figure 6.17 Distribution of momentum difference between reconstructed and generated π^0 before and after mass constraint.

A counterpart study is repeated for D^0 candidates. Distributions are shown in

Figure 6.18. Improvement is relatively small compared to π^0 since the momentum resolution of charged tracks are much smaller than that of unconverted photons.

Applying mass constraint on both daughter particles, D^0 and π^0 together, provides further improvement on the invariant mass resolution of D^{*0}. Results are shown in Figure 6.19.

6.7 Summary of cuts

All the cuts for the particle selection in the analysis is summarised in Table 6.1. Note that selection efficiencies after these cuts for both D^0 and π^0 are greater than 95%.

Table 6.1 Standard cuts applied on the selection of particles.

Variable Name	Symbol	Accepted Range
Kaon Momentum	$p_{K^\pm}$	> 1 GeV
Pion Momentum	$p_{\pi^\pm}$	> 0.5 GeV
Transverse impact-parameter	$\|d_0\|$	< 0.5 cm
Longitudinal impact-parameter	$\|z_0\|$	< 2.0 cm
dE/dx with Kaon hypothesis	$\|\chi\left(\frac{dE}{dx}\right)\|$	< 3.0
dE/dx with Pion hypothesis	$\|\chi\left(\frac{dE}{dx}\right)\|$	< 3.0
D^0 Momentum	p_{D^0}	> 12 GeV
Cosine angle	$\cos\theta^*$	< 0.8
Photon Energy	E_γ	> 0.5 GeV
Neutral pion Energy	E_{π^0}	< 10 GeV
Invariant mass of $K\pi$ pair	$m_{K\pi}$	$1.83 < m < 1.90$ GeV
Invariant mass of $\gamma\gamma$ pair	$m_{\gamma\gamma}$	$0.05 < m < 0.25$ GeV

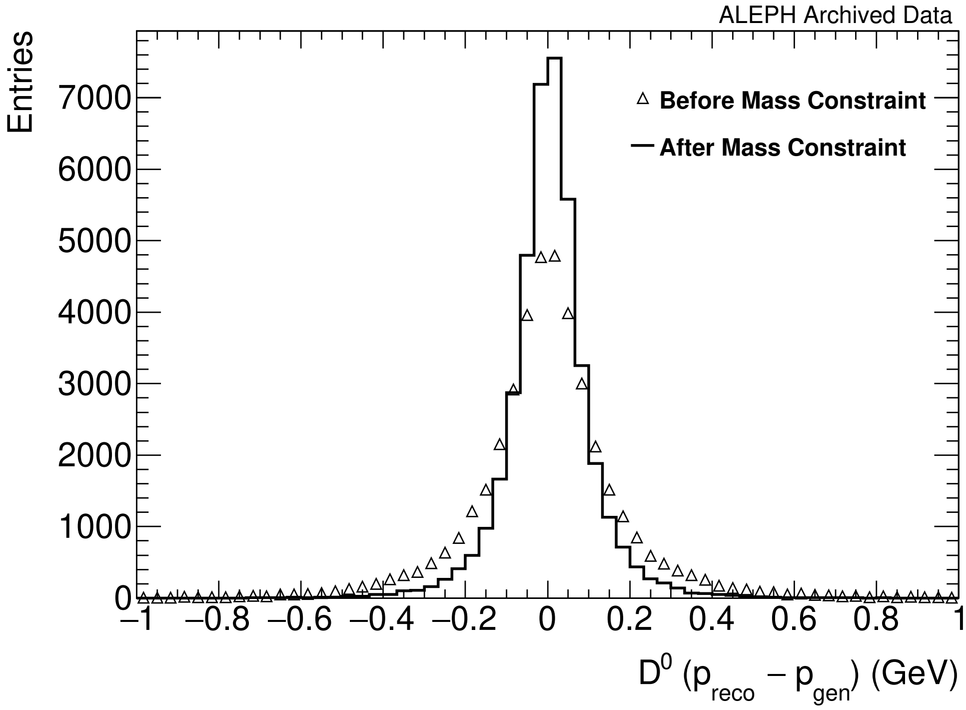

Figure 6.18 Momentum difference between reconstructed and generated D^0 before and after mass constraint.

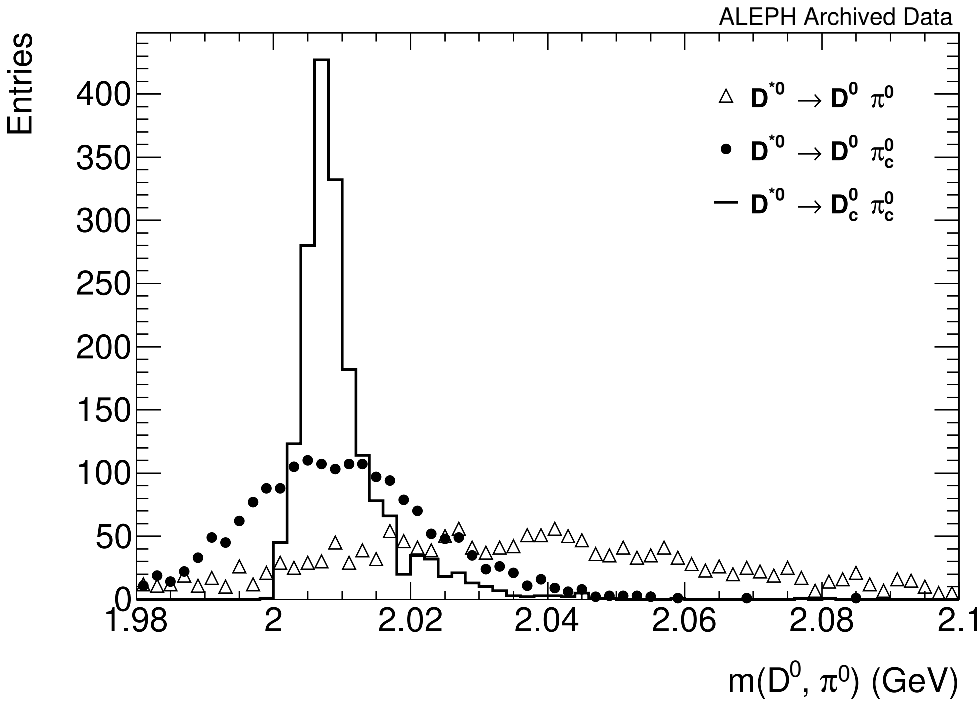

Figure 6.19 Invariant mass distribution of D^{*0} signal. Triangles represent unconstrained signals. Full circles represents mass constraint only applied on π^0. Solid line represents mass constraint applied on both of the daughter particles.

CHAPTER 7

EXTRACTION OF THE D^{*0} SIGNAL

7.1 Introduction

The production rate and the cross-section of $D^{*0}(2007)$ meson is extracted from the invariant mass distributions of their daughter particles, D^0 and π^0, by applying the fitting procedure for the invariant mass to the summation of a background and a signal functions. The products D^0 and π^0 are reconstructed from the decay channels $D^0 \rightarrow K^-\pi^+$ and $\pi^0 \rightarrow \gamma\gamma$ respectively. Here, π^0 is called a soft particle because the masses of D^{*0} and D^0 are close to each other. As a result, the energy of π^0 becomes relatively small. Branching ratios of these decay channels are given in Table 7.1.

Table 7.1 Decay channels, corresponding branching ratios and masses of parent particles used in the analysis [7].

Decay	BR	Nominal Mass (MeV)
$D^{*0} \rightarrow D^0\pi^0$	$64.70 \pm 0.90\%$	2006.8500 ± 0.0500
$D^0 \rightarrow K^\pm\pi^\mp$	$3.95 \pm 0.03\%$	1864.8300 ± 0.0500
$\pi^0 \rightarrow \gamma\gamma$	$98.82 \pm 0.03\%$	134.9770 ± 0.0005

In the analysis, standard cut based and multivariate analysis methods such as BDT (Boosted Decision Trees) from the TMVA library of ROOT framework [34] are used. In the extraction of D^{*0} signal, well known fitting procedure is applied.

7.2 Signal Reconstruction

The data are analyzed in 10 intervals of scaled energy: $x_E = E/E_{beam}$. Here E_{beam} (about 45.6 GeV) is the LEP beam energy. These energy intervals are tabulated in the Table 7.2.

Table 7.2 Scaled energy intervals.

Interval	x_E Range
0	$0.00 \leq x_E < 0.30$
1	$0.30 \leq x_E < 0.40$
2	$0.40 \leq x_E < 0.45$
3	$0.45 \leq x_E < 0.50$
4	$0.50 \leq x_E < 0.55$
5	$0.55 \leq x_E < 0.60$
6	$0.60 \leq x_E < 0.65$
7	$0.65 \leq x_E < 0.70$
8	$0.70 \leq x_E < 0.75$
9	$0.75 \leq x_E < 0.80$
10	$0.80 \leq x_E < 1.00$

Using Monte Carlo simulation, one can study the theoretical shape of the energy distributions for the reconstructed D^{*0} mesons. Invariant mass distributions for several energy intervals for simulation and recorded data using standard cut based method are shown in the Figure 7.1. Distributions for all the x_E intervals are given in Appendix A.

Mass distribution for energy range $x_E < 0.3$ (top left corner) shows that the signal significance is poor. However, it is possible to extract D^{*0} signal candidates for $x_E \geq 0.3$ which corresponds to approximately $E_{D^{*0}} > 12$ GeV. It is found that, the extraction of signal using fitting procedure for $x_E < 0.5$ is very difficult because of the unstabilities in fits. It is clear that a sophisticated method is required in order to improve signal significance. Therefore, multi variate analysis classification methods from machine learning algorithms (in addition to the standard cut based analysis) is applied for signal extraction of D^{*0}.

Note that, applications of sophisticated machine learning algorithms have become increasingly popular in particle physics due to their superior discrimination capabilities and growth of available computing power in recent years. For this reason, TMVA classification methods are applied in the analysis to improve signal significance of D^{*0}.

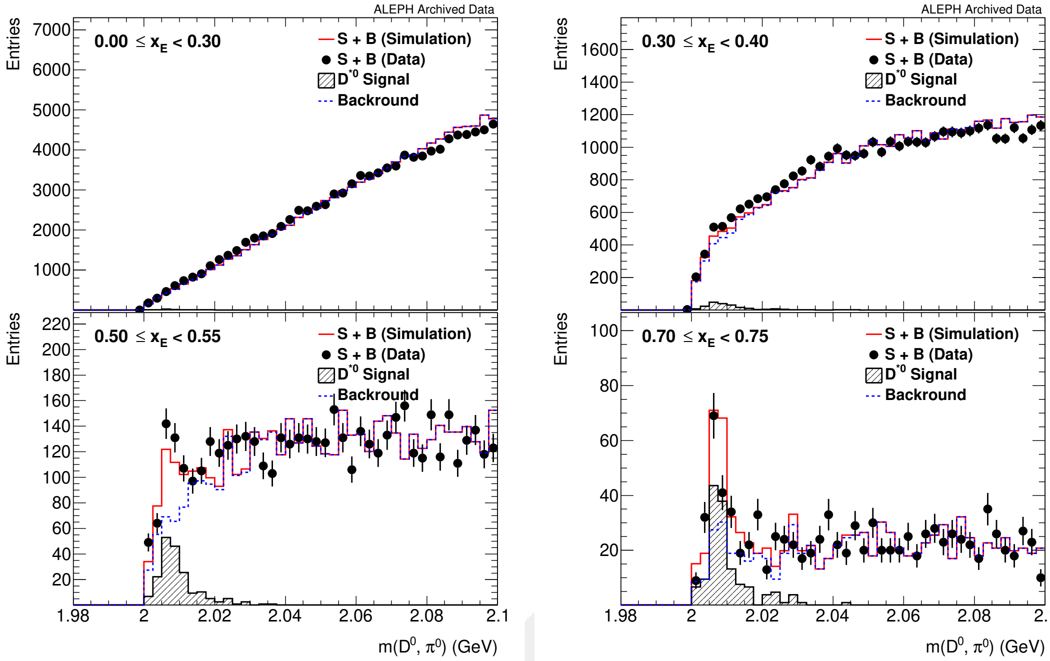

Figure 7.1 Invariant mass of D^0 and π^0 for a few x_E intervals. S + B corresponds to summation of Signal and Background.

7.3 TMVA Analysis

It is essential to extract a maximum of the available information from the data in high energy physics. Multivariate classification methods based on machine learning techniques provides further performance in the analysis. Under ROOT framework, TMVA is a toolkit consists of training, testing, validation and application of various multivariate analysis algorithms. All multivariate techniques in TMVA belong to the family of "supervised learning" algorithms.

Classification methods process the training events, for which the desired output is known, to determine the mapping function that describes a decision boundary. Testing events are used to apply boundaries on samples which were not in the training list. TMVA provides input and output distributions, cut efficiencies and receiver operating characteristic (ROC curve) plot for all the methods used in the training. The toolkit also provides a regression analysis for a linear or non-linear correlation investigation purposes between input and target [34].

In this analysis, classification method is used in order to distinguish the signal and the background of D^{*0} candidates. Input variables and the method used in the analysis are described in the following subsections.

7.3.1 Input variables for the analysis

Training and testing processes require a set of variables for the signal and the background separately. Table 7.3 contains the list of variables selected for the analysis.

Table 7.3 Variables used in the training.

Variable Name	Description
D0P	D^0 momentum.
D0CosTheta	$\cos\theta^*$ as described in the Section 6.4.
Pi0P	π^0 momentum.
Pi0PhtAngle	Angle between two daughter photons of π^0.
DsE	Ratio of subtraction to summation of D^0 and π^0 energies[1].

These variables are grouped into two, signal and background, which are discriminated by Monte Carlo studies. Figure 7.2 illustrates the distributions for all the input variables in the training process. Note that, half of the data are used in the training and the other half for testing.

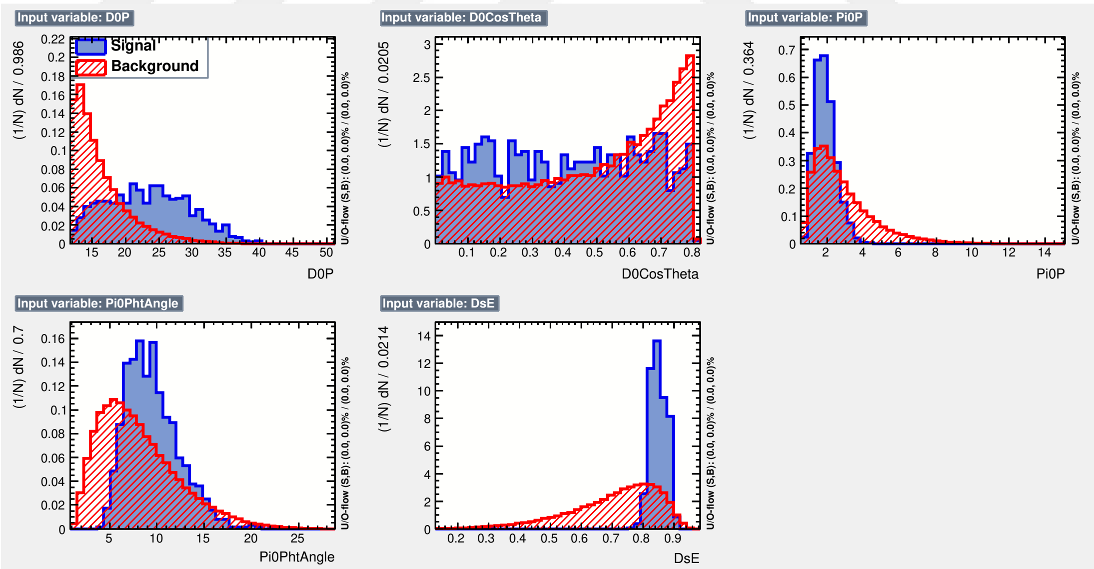

Figure 7.2 Distributions of input variables used in TMVA.

As the first step, ROC curve is inspected to find the optimum method for the analysis since TMVA provides various classification methods. Comparison of performances for different methods is shown in the Figure 7.3.

[1] That is, $DsE = |E_{D^0} - E_{\pi^0}|/(E_{D^0} + E_{\pi^0})$

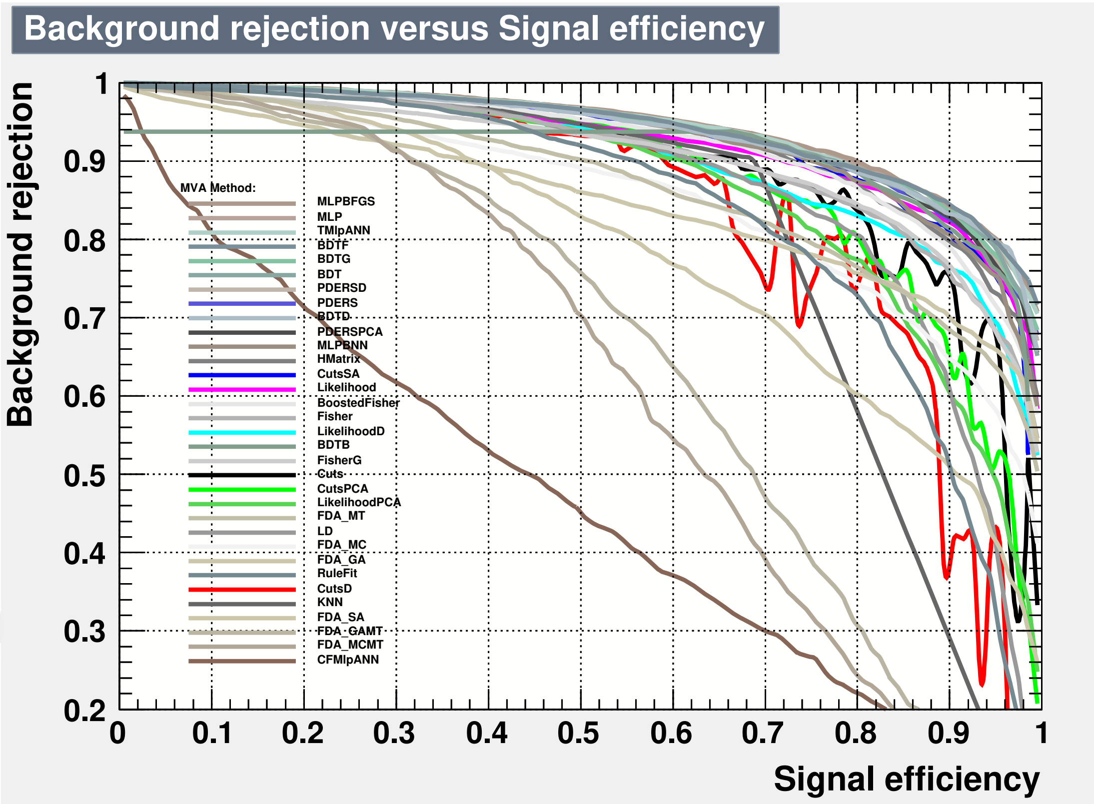

Figure 7.3 Comparison of TMVA classification methods (ROC curve).

ROC curve carries the information about performances of various methods. It can be understood from the curves that most of the methods show good performance. Some of them are poor in terms of signal efficiency and background rejection such as FDA method. Multi layer perceptron (MLP) methods are shown to be having the best performance, however, it is poor in terms of time consumption for the training and testing compared to other methods such as Boosted Decision Trees (BDT).

BDT method is chosen in this analysis since its performance is one of the best in all methods and it is fast. For the same value of signal efficiency, background rejection difference between BDT and the best method in the ROC curve list, is negligible.

7.3.2 BDT Method

Boosted Decision Tree method from TMVA toolkit uses the idea of forming a tree with its branches, nodes and leafs. Leafs at a branch represents the terminal where concluding decision is made. BDT categorization is built with conditional selections on the sample with a criteria to decide whether it is a signal or a background. Nodes are representing the points where data is split into various subgroups in order to have branches end up with homogeneous class items.

In an ideal case, all the items in a sample are from the similar class hence the *entropy* for this sample becomes zero. Training procedure is based on partitioning the data into subsets until the entropy becomes as low as possible. Boosted term refers to developing new trees with re-weighted samples which ends up in a wrong class decisions during the training. Boosting provides increased performance since it compensates the fluctuations in the training sample. Further details can be found in BDT Method class reference [35].

In the analysis, various number of boosted decision trees in the forest is tested and the default value, which is 850 is chosen since the performance is not altering significantly. Distribution of BDT response for the test sample, and cut efficiency plots are provided by the TMVA toolkit at the end of training and testing which are shown in the Figure 7.4 a and b respectively.

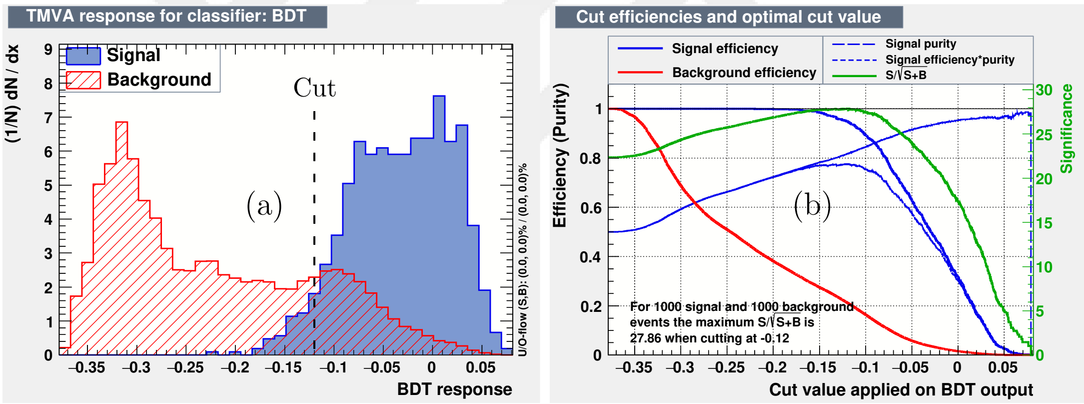

Figure 7.4 BDT method (a) classifier response and (b) cut efficiency distributions. Optimum cut (−0.12) suggested by the TMVA method is shown on BDT response distribution with dashed line.

Optimum cut value suggested by the BDT method is −0.12. Applying TMVA cut value in the analysis for the purpose of rejecting candidates which were classified as background, results in an improvement in the significance of the invariant mass distribution of $D^0\pi^0$ pairs.

7.3.3 Performance of BDT

Figure 7.5 shows the comparison of $m(D^0, \pi^0)$ distributions before and after TMVA cut applied. See Appendix B for the distributions of all x_E intervals.

Obviously TMVA improves signal purity for both simulation and recorded data.

Using Monte Carlo simulation, for $x_E \geq 0.3$, number of signal and background are counted around the signal region (2.00 GeV $< m <$ 2.04 GeV). Then, the efficiency and purity before and after the TMVA cut are calculated. Results are given in Table 7.4. It is clear that the signal significance is improved by about 6%.

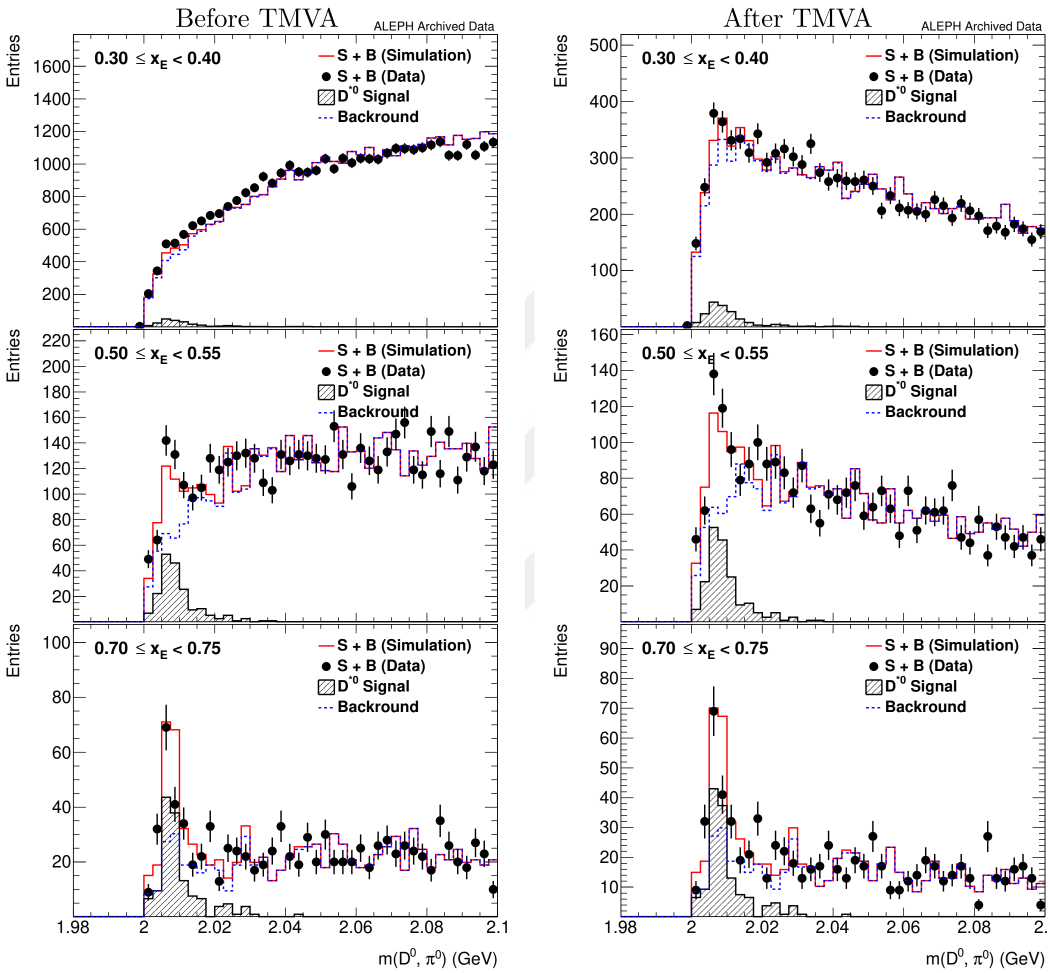

Figure 7.5 Invariant mass of D^0 and π^0 for a few x_E intervals before (left column) and after (right column) the TMVA suggested cut value is applied.

Table 7.4 Signal (S) and background (B) counting results together with signal efficiency (E) and purity (P) calculations of D^{*0} before and after the TMVA cut.

	Signal	Background	S/B	P	E	$E \times P$
Before	1881	52757	3.6%	3.4%	100.0%	3.4%
After	1761	15822	11.1%	10.0%	93.6%	9.4%

7.4 Fitting Procedure and Extraction of Signal

To extract the signal and measure the rate of the D^{*0}, the invariant mass distribution is fitted (using the method of least squares) as a sum of background and signal functions. In this section, Monte Carlo simulation models for each component contributing to the D^0 and π^0 invariant mass will be described.

7.4.1 Signal Shape

D^{*0} signal distribution is modeled by using two different line shapes namely Landau and Relativistic Breit-Wigner functions.

The explicit expression for Landau distribution is given in the Equation 7.1.

$$f_L(m) = Ae^{-\frac{1}{2}(\lambda\ +\ e^{-\lambda})} \tag{7.1}$$

where $\lambda = (m - \mu)/(\sigma)$, μ is mean (most probable) value and σ is the width of distribution. For the signal function, A, μ and σ values are free parameters while m is the invariant mass of $D^0\pi^0$ pair.

On the other hand, Relativistic Breit-Wigner distribution is given in the Equation 7.2.

$$f_{BW}(m) = \frac{m \cdot m_0 \cdot \Gamma(m)}{(m^2 - m_0^2)^2 + m_0^2 \cdot \Gamma^2(m)} \tag{7.2}$$

where m is the invariant mass of daughter particles, m_0 is the nominal D^{*0} mass, and Γ is the mass dependent width. In this analysis, the Equation 7.3 is found to be suitable.

$$\Gamma(m) = \Gamma_0 \cdot \left(\frac{q}{q_0}\right)^3 \frac{2q_0^2}{q_0^2 + q^2} \tag{7.3}$$

where Γ_0 is a scale factor and selected as a free parameter in the fit. q is the momentum of the decay products in the rest frame of the parent and q_0 is the momentum when $m = m_0$ [31]. q can be written in terms of the particle masses as follows:

$$q^2 = \frac{(m^2 - m_{D^0}^2 + m_{\pi^0}^2)^2}{4m^2} - m_{\pi^0}^2 \tag{7.4}$$

In Figure 7.6, the first row shows the Landau and RBW functions fitted to Monte Carlo signal distribution respectively for an x_E interval. Ratios of the integral of the signal fit functions to signal histogram contents as a function of x_E intervals is given in the second row. Both functions seem to be modeling the signal properly from the Monte Carlo simulation studies. In the analysis, both functions are used for extraction of signal separately and their difference is considered as a systematic error.

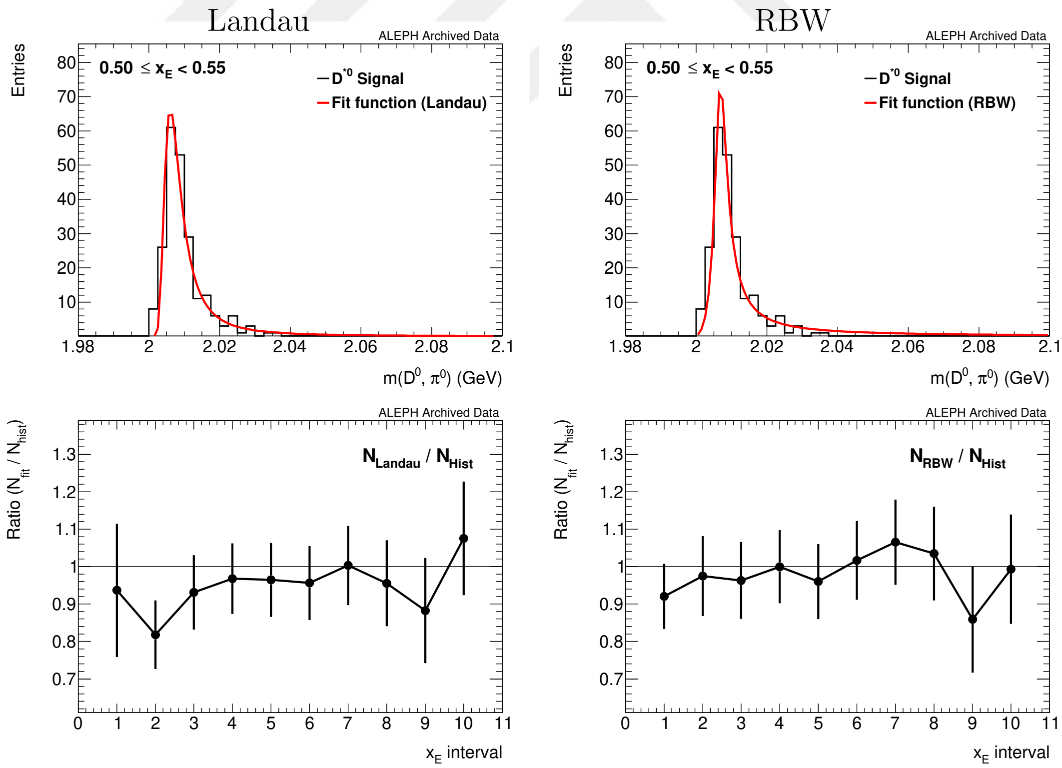

Figure 7.6 Sample fit results of Landau and Relativistic Breit-Wigner functions (first row) and ratio of the fitted signal integral to the number of reconstructed D^{*0} mesons in the Monte Carlo for all x_E intervals (second row).

7.4.2 Combinatorial Background

The combinatorial background is parameterized by the following function:

$$f_b(m) = (m - p_1)\exp(\ p_2 m \ + \ p_3 m^2) + p_4 + p_5 m \tag{7.5}$$

where m is the invariant mass of $D^0\pi^0$ pair and p_1 to p_5 are free parameters adjusted by the fitting procedure. An example fit result, for a special x_E interval, for a background distribution is shown in Figure 7.7.

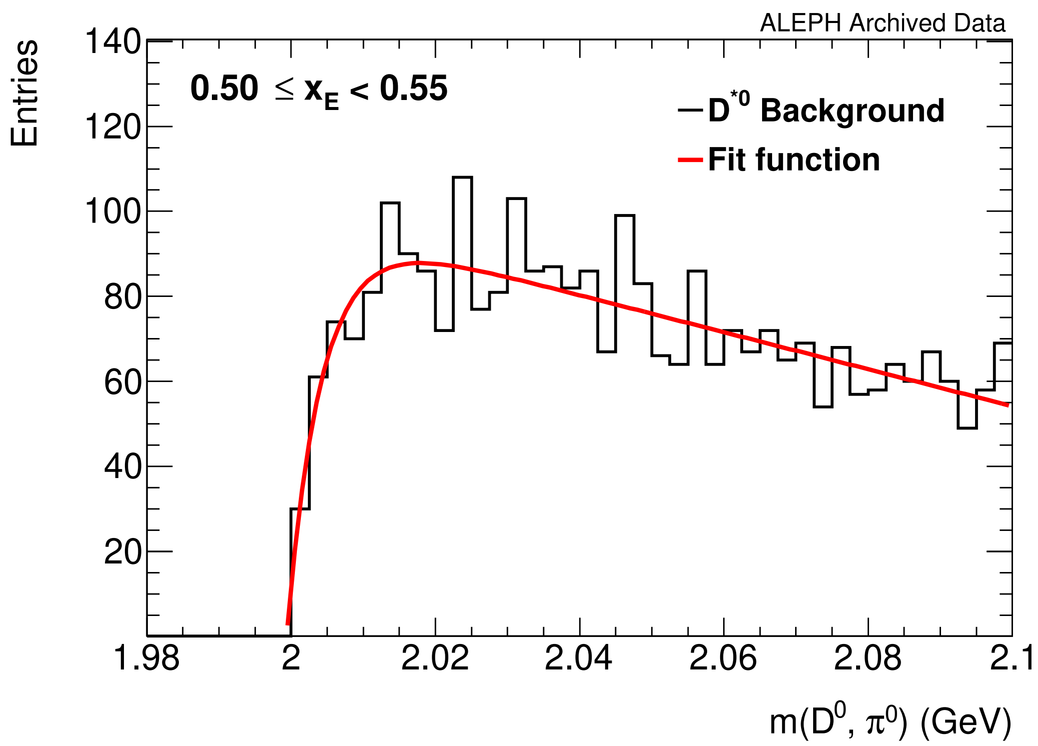

Figure 7.7 Fit result on D^{*0} background distribution for a sample x_E interval.

7.4.3 Total Fitting Function

By adding signal and background model functions, the total fitting function is built as follows:

$$f(m) = (m - p_1)\exp(\ p_2 m \ + \ p_3 m^2) + p_4 + p_5 m + p_6 e^{-\frac{1}{2}(\frac{m-p_7}{p_8}\ +\ e^{-\frac{m-p_7}{p_8}})} \tag{7.6}$$

Figure 7.8 shows an example of the fit function results for Monte Carlo and recorded data. Fit results for all x_E intervals can be seen in the Appendix C.

Invariant mass distribution of D^0 and π^0 peaks at around 2006 MeV which is consistent with the corresponding value at PDG (2006.85 ± 0.05 MeV). In addition, the mass difference distribution, given in Figure 7.9, peaks at about 142 MeV which is also consistent with the corresponding value at PDG (142.014 ± 0.030 MeV) [7].

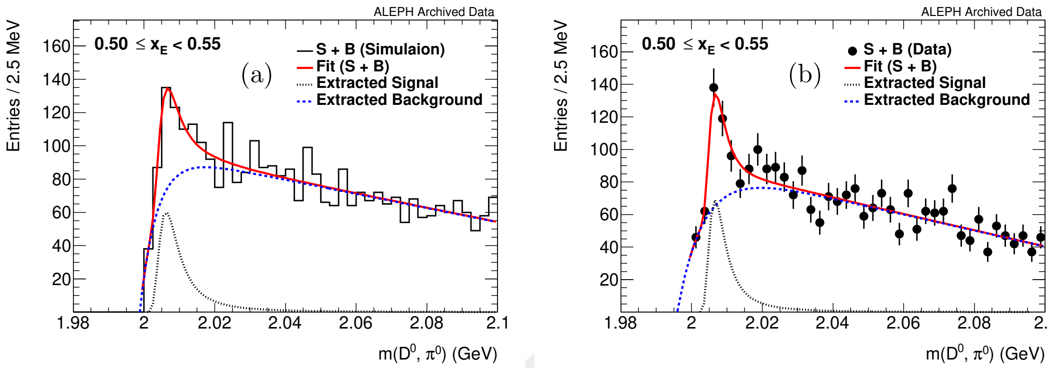

Figure 7.8 Fit result for the invariant mass of D^0 and π^0 (a) Monte Carlo simulation and (b) recorded data distribution for one x_E interval.

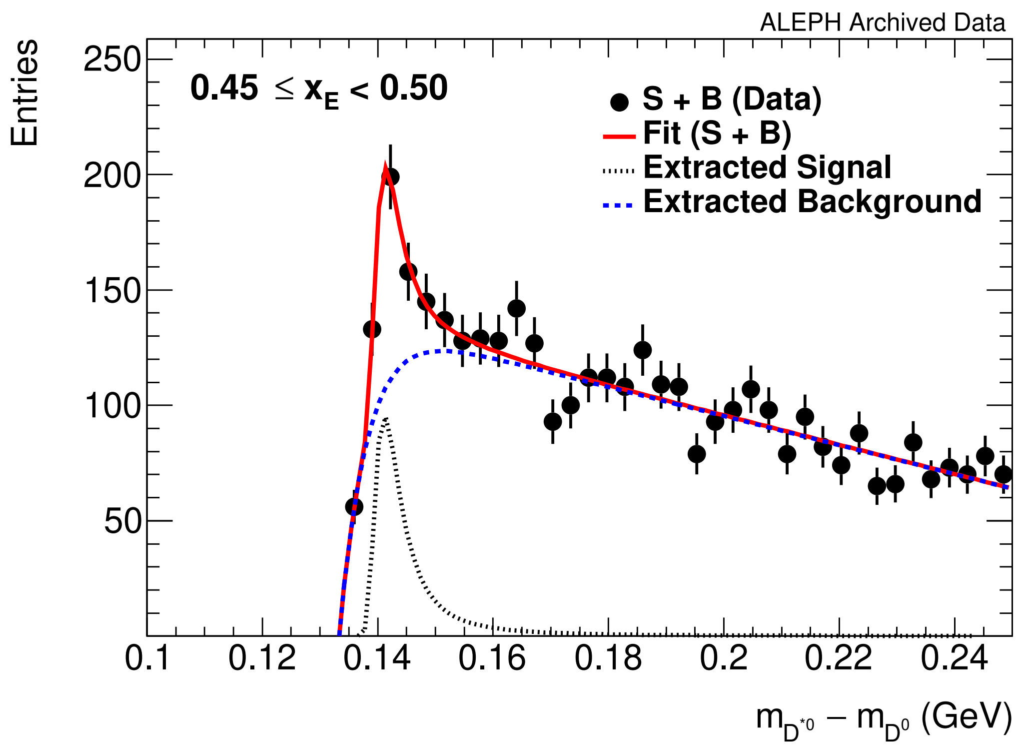

Figure 7.9 Mass difference distribution. Peak value is at 141.6 ± 0.1 MeV.

7.5 Production Rates and Differential Cross-Section

Production rate per event and the differential cross-section of D^{*0} for each x_E intervals are measured, calculated and will be presented here.

The production rate, R, is calculated for each momentum and energy intervals by correcting fitted signal S for the reconstruction efficiency $\mathcal{E}$ and normalising to one event. The rates are corrected for the branching ratio which is $BR(D^{*0} \rightarrow\ D^0\pi^0) = 64.70 \pm 0.90\%$. Calculation is given below.

$$R = \frac{S}{N}\frac{1}{\mathcal{E}}\frac{1}{BR} \tag{7.7}$$

where N is the total number of hadronic events which is obtained as:

$$N = N_{gen}\left(\frac{N_{DA}}{N_{MC}}\right) \tag{7.8}$$

where N_{gen} is the number of generated events before event selection in the Monte Carlo, N_{DA} and N_{MC} are the numbers of selected events in data and Monte Carlo respectively. The efficiency is defined as

$$\mathcal{E} = \frac{S_{rec}}{S_{gen}} \tag{7.9}$$

where S_{rec} is the number of reconstructed D^{*0} mesons in the Monte Carlo (macthed to the generated level) and S_{gen} is the number of generated D^{*0} mesons in the Monte Carlo (before event selection cuts).

Dividing the rates by the width of the energy intervals, δx_E, gives the values for the differential cross-section, $1/\sigma_{tot} \cdot d\sigma/dx_E$, for each interval:

$$\frac{1}{\sigma_{tot}}\frac{d\sigma}{dx_E} = \frac{R}{\delta x_E} = \frac{1}{\delta x_E}\frac{S}{N}\frac{1}{\mathcal{E}}\frac{1}{BR} \tag{7.10}$$

Combining the above equations yields:

$$R = \left(\frac{S}{S_{rec}}\right)\left(\frac{S_{gen}}{N_{gen}}\right)\left(\frac{N_{MC}}{N_{DA}}\right)\left(\frac{1}{BR}\right) \quad \text{and} \quad \frac{1}{\sigma_{tot}}\frac{d\sigma}{dx_E} = \frac{R}{\delta x_E} \tag{7.11}$$

See Chapter 9 for the results of above calculations together with statistical and systematic errors for all x_E intervals.

7.5.1 An Example of Rate and Cross Section Calculation

An example production rate and cross section calculations for the energy interval $0.50 \leq x_E < 0.55$, namely $\delta x_E = 0.05$, is as follows. Number of selected events in this analysis are 3,239,746 and 1,701,263 for data and Monte Carlo simulation respectively. Number of generated events is 3,160,166. N is calculated by the Equation 7.8.

$$N = N_{gen}\left(\frac{N_{DA}}{N_{MC}}\right) = 3160166\left(\frac{3239746}{1701263}\right) = 6017961 \text{ events}$$

Number of reconstructed and generated D^{*0} mesons is counted as 94 and 38731 respectively. Efficiency is then calculated by using the Equation 7.9.

$$\mathcal{E} = \frac{S_{rec}}{S_{gen}} = \frac{94}{38731} = 0.0024$$

Number of D^{*0} mesons evaluated in the analysis for recorded data is 159 from the fit procedure for the same x_E interval. Branching ratio for the decay channel $D^{*0} \to D^0\pi^0$ is 0.647. Production rate for the interval is calculated as given in the Equation 7.7.

$$R = \frac{S}{N}\frac{1}{\mathcal{E}}\frac{1}{BR} = \frac{159}{6017961}\,\frac{1}{0.0024}\,\frac{1}{0.647} = 0.017 \text{ particles/event}$$

Hence, the differential cross-section is:

$$\frac{1}{\sigma_{tot}}\frac{d\sigma}{dx_E} = \frac{R}{\delta x_E} = \frac{0.017}{0.05} = 0.340 \text{ particles/event/GeV}$$

Finally, by using error propagation formula, one can report the values together with corresponding statistical errors originating from fitting procedure as follows:

$$R = 0.017 \pm 0.003 \text{ particles/event}$$

$$\frac{R}{\delta x_E} = 0.340 \pm 0.057 \text{ particles/event/GeV}$$

CHAPTER 8

SYSTEMATIC ERROR ANALYSIS

8.1 Introduction

Counting uncertainties that result in values being randomly high or low are expressed as statistical errors. On the other hand, model and measurement uncertainties in the analysis procedure result in values being randomly or systematically high or low are expressed as systematic errors.

The study of systematic uncertainties for this analysis takes various forms; the details are given in the following sections. The results, including statistical errors, are summarised in Table 8.3 at the end of this chapter.

8.2 Source of Systematic Errors

The potential systematic error sources can be divided into three categories; Machine learning (TMVA) suggested optimum cut, track selection cuts and modeling signal function. An additional systematic error due to the uncertainty in the extrapolation to full x_E range is included in the final results.

8.2.1 TMVA suggested cut

The optimum cut suggested by the multivariate analysis of is -0.12. This cut is decreased to -0.14 and increased to -0.10. The largest contribution from this cut is about 17%.

8.2.2 Track Selection Cuts

The calculation of the efficiency corrections relies on an adequate reproduction of the detector acceptances by the Monte Carlo. Repeating the measurement with different (though reasonable) values of cuts applied to the track selection criteria, results in variations in the measured D^{*0} rate. Such variations can be interpreted as discrepancies between the calculated efficiency and the true efficiency for the reconstruction of the D^{*0} signal. However, it is expected that varying cuts will also give rise to statistical variations that are already accounted for in the assignment of statistical errors. This is supported by the observation that, variations due to selection cuts are seen to be random in magnitude and sign in general. Therefore the following results for systematic errors due to selection cuts are considered to be over-estimates. Again, the largest variation in the measured rate for each cut for each x_E interval is assigned as the systematic error.

Photon Energy, E_γ

Energy cut for the selection of photons is 0.5 GeV. It is increased to 0.6 GeV. The largest contribution from this cut is about 26%.

Transverse Impact Parameter, d_0

The cut applied to the transverse impact parameter of charged tracks is 0.5 cm. This cut is decreased to 0.3 cm and increased to 1.3 cm. The largest variation is found to be about 21%.

Cosine angle cut for D^0, $\cos\theta^*$

A default cut $|\cos\theta^*| < 0.8$ for D^0 is applied. This cut is decreased to 0.75 and increased to 0.85 and maximum deviation is assigned as systematic error. The largest contribution from this cut is about 19%.

Ionisation Energy Loss, χ(dE/dx)

A cut of $|\chi(\mathrm{dE/dx})| < 3$ is applied on energy loss for charged tracks. The rate extraction procedure is repeated after omitting the cut completely. The largest contribution from this cut is about 28% which is the maximum among all systematic errors.

Momentum cut for D^0

Momentum cut for D^0 candidates is 12 GeV. This cut is decreased to 11 GeV and increased to 13 GeV. The largest contribution from this cut comes from the first energy interval which is about 22%.

8.2.3 Signal Function

By default,the landau function is selected for the signal shape. The signal extraction procedure is repeated using the Relativistic Breit-Wigner function. The difference in the measurements are taken as a systematic error. The maximum fluctuation is about 21%.

8.2.4 Extrapolation to $x_E = 0$

The measurement covers only the regions where $x_E \geq 0.3$. To estimate the total production rate, the total measured rate is extrapolated to $x_E = 0$. The unmeasured fraction of the total rate in the recorded data is about 39% for $x_E < 0.3$. The procedure relies on the Monte Carlo to give the correct scale factor for the extrapolation. To estimate the uncertainty in the scale factor, the calculation is repeated for different Monte Carlo simulation programs and the results are listed in Table 8.1.

Table 8.1 Estimated values of unmeasured fraction and corresponding scale factors for different Monte Carlo programs.

Monte Carlo Program	Unmeasured Fraction ($x_E < 0.3$)	Scale Factor ($x_E = 0$)
JETSET 7.4 (ALEPH tuned)	37%	1.593
PYTHIA 8.2 (Default tuning)	38%	1.610
HERWIG++ 2.6 (Default tuning)	33%	1.544

The largest difference, about 4%, is between JETSET and HERWIG. This value is taken as an additional systematic uncertainty.

8.3 Summary of Errors

All sources of systematic errors used in calculations are shown in the Table 8.2 with corresponding maximum and minimum errors of all x_E intervals.

Table 8.2 Summary of the applied cuts and variations in their values used in the systematic error analysis. Corresponding minimum and maximum contributions are expressed in %.

Source of error	Default value	Changes	Error (%) Min.	Error (%) Max.
TMVA Cut	−0.12	−0.10, −0.14	3	17
E_γ	0.5 GeV	0.6 GeV	2	26
d_0	0.5 cm	0.3, 1.3 cm	2	21
$\cos\theta^*$	0.8	0.75, 0.85	1	19
$\chi(dE/dx)$	[−3, 3]	removed	2	28
P_{D^0}	12 GeV	11, 13 GeV	1	22
Signal shape	Landau	RBW	2	21

Table 8.3 summarises the statistical and systematic errors for the D^{*0} measurement in x_E intervals. For the systematic errors, the individual errors from each source are shown for each measured energy intervals.

The total error 'e_{all}' for the total measured ranges, calculated for each error source, is taken as the sum of the errors, e_i, in each interval (horizontally in the table) weighted by the rate, R_i. For this, the quadratic sum is calculated as given in The Equation 8.1

$$e_{all} = \frac{\sqrt{\sum (e_i R_i)^2}}{\sum R_i} \tag{8.1}$$

The total systematic error, e_{tot}, for each energy interval, is calculated by taking the quadratic sum of each error source e_k (vertically in the table). Hence

$$e_{tot} = \sqrt{\sum e_k^2} \tag{8.2}$$

The last row of each table shows the total error for all, and each energy interval, calculated as the quadratic sum of the total systematic and the statistical errors.

Table 8.3 Systematic and statistical errors for the D^{*0} rate in each measured energy interval. All values are expressed in % rounded to one decimal place.

Source of Error		x_E interval									
	e_{all}	1	2	3	4	5	6	7	8	9	10
TMVA Cut	5.2	12.5	13.3	9.3	12.2	14.8	5.6	17.0	6.0	2.9	4.7
E_γ	7.4	19.0	17.9	8.5	10.1	25.5	7.0	9.2	8.4	1.5	7.1
d_0	6.8	17.6	15.7	10.2	5.1	21.1	8.9	5.2	2.0	5.0	3.0
$\cos\theta^*$	7.0	18.5	18.7	4.1	10.1	13.0	3.8	19.1	4.3	12.6	0.6
$\chi(dE/dx)$	3.9	5.2	17.0	4.8	5.3	28.0	12.5	5.2	2.4	10.6	7.8
P_{D^0}	7.9	21.9	13.4	3.6	4.4	20.0	5.0	4.4	1.9	0.6	0.0
Signal shape	3.5	4.2	6.6	14.7	16.0	15.3	5.8	21.3	16.0	1.5	2.0
Systematic error (e_{tot})	16.3	41.2	40.1	23.1	26.1	53.9	19.7	35.6	19.9	17.6	12.1
Statistical error	9.2	22.4	19.7	24.6	15.4	7.3	28.9	23.7	15.6	20.2	10.0
Total error	18.7	46.9	44.7	33.7	30.3	54.4	35.0	42.8	25.3	26.8	15.7

CHAPTER 9

RESULTS AND CONCLUSION

9.1 Results

In this section, the results obtained from the ALEPH measurement for D^{*0} meson are presented and compared with the Monte Carlo simulation event generator softwares.

9.1.1 Rates and Differential Cross-sections

Table 9.1 shows the rates and differential cross-sections of D^{*0} in each interval of energy. The errors are statistical and systematic respectively. The result of sum over each x_E interval is also shown. The last row gives the result of extrapolated sum to include $x_E = 0$ together with an additional error which is about 6% representing the extrapolation uncertainty.

The differential cross-section as a function of x_E are compared to theoretical predictions in Figure 9.1. Quadratic sum of statistical and systematic contributions are shown as error bars. Statistical errors are also indicated by perpendicular lines on the error bars. Note that unmeasured range, $x_E < 0.3$, is equally divided into six subranges in Monte Carlo event generator simulations to see the tendency in that interval.

Table 9.1 Measured multiplicities and differential cross-sections for the D^{*0} in x_E intervals. The result of summing over the measured x_E intervals is also given, including extrapolation to full x_E range with an additional error due to the uncertainty in the extrapolation.

x_E range	Multiplicity $D^{*0}(2007)/Z$ decay	$(1/\sigma_{had})d\sigma/dx_E$
0.30 - 0.40	0.0659 ± 0.0160 ± 0.0362	0.6587 ± 0.1604 ± 0.3619
0.40 - 0.45	0.0171 ± 0.0044 ± 0.0137	0.3420 ± 0.0875 ± 0.2740
0.45 - 0.50	0.0315 ± 0.0082 ± 0.0081	0.6301 ± 0.1637 ± 0.1617
0.50 - 0.55	0.0148 ± 0.0028 ± 0.0071	0.2970 ± 0.0568 ± 0.1429
0.55 - 0.60	0.0120 ± 0.0025 ± 0.0114	0.2395 ± 0.0507 ± 0.2289
0.60 - 0.65	0.0171 ± 0.0033 ± 0.0031	0.3427 ± 0.0655 ± 0.0623
0.65 - 0.70	0.0038 ± 0.0010 ± 0.0027	0.0767 ± 0.0197 ± 0.0550
0.70 - 0.75	0.0073 ± 0.0010 ± 0.0021	0.1466 ± 0.0199 ± 0.0415
0.75 - 0.80	0.0059 ± 0.0014 ± 0.0015	0.1181 ± 0.0280 ± 0.0298
0.80 - 1.00	0.0058 ± 0.0018 ± 0.0011	0.0290 ± 0.0091 ± 0.0053
0.30 - 1.00	0.1812 ± 0.0194 ± 0.0421	
all x_E	0.2886 ± 0.0309 ± 0.0670 ± 0.0088	

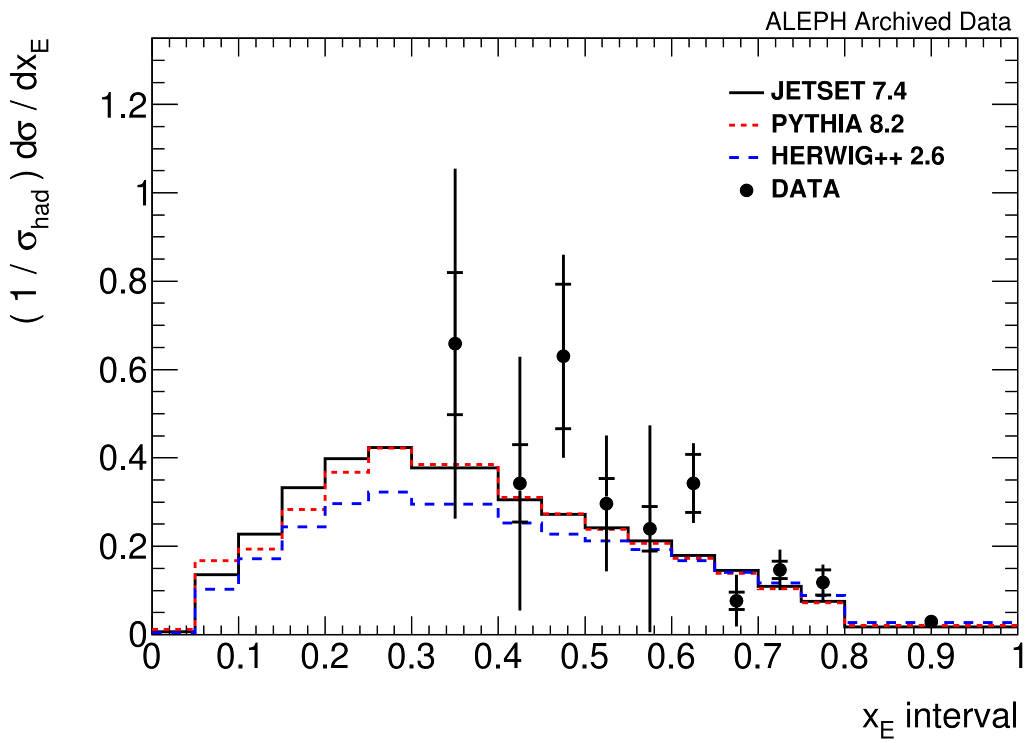

Figure 9.1 Differential cross-sections for D^{*0} meson as a function of x_E in comparison with the Monte Carlo predictions. Quadratic sum of the statistical and systematic errors are shown as error bars. Statistical errors are indicated with a perpendicular line on error bars.

9.1.2 Production Rate Comparison

The production rates of D^{*0} are compared with the rates of $D^{*\pm}$ [7]. Table 9.2 shows the production rates of D^{*0} measured with the recorded data and Monte Carlo simulations and the ratio of the rates, $N(D^{*0})/N(D^{*\pm})$.

Table 9.2 Comparison of the total multiplicity of the D^{*0}, $N(D^{*0})$ and the ratio $N(D^{*0})/N(D^{*\pm})$. Errors are statistical and systematic respectively.

Data set	$N(D^{*0})$	$N(D^{*0})/N(D^{*\pm})$
ALEPH data	$0.289 \pm 0.031 \pm 0.067$	$1.566 \pm 0.207 \pm 0.374$
JETSET 7.4 (ALEPH tuned)	0.195	1.004
PYTHIA 8.2 (Default tuning)	0.191	0.978
HERWIG++ 2.6 (Default tuning)	0.162	1.017

9.2 Summary and Conclusion

The inclusive production of the $D^{*0}(2007)$ meson in 3,239,746 selected hadronic Z decays has been studied. The results obtained from ALEPH data fits are presented and compared with theoretical predictions. D^{*0} mesons are reconstructed from the decay mode $D^{*0} \rightarrow D^0\pi^0$ ($BR \approx 65\%$). The measurement covers an energy interval $x_E \geq 0.3$ where $x_E = E/E_{beam}$; these exclude $\sim 37\%$ of D^{*0} mesons from measurement. It is found that a Boosted Decision Trees method from the TMVA toolkit improves D^{*0} selection purity explicitly.

The measured D^{*0} multiplicities and cross-sections are given in Table 9.1 and the cross-sections as a function of particle energy are compared to theoretical models in Figure 9.1. From this data, average D^{*0} multiplicity per hadronic Z decay is found as:

$$\langle N_{D^{*0}(2007)} \rangle = 0.289 \pm 0.074$$

where the uncertainty is the quadratic sum of statistical, systematical and extrapolation errors.

This study is the first measurement of inclusive production rate and cross-section of D^{*0} mesons in hadronic Z decays. Measured D^{*0} production rates using ALEPH data are found to be consistent with default tuned PYTHIA and HERWIG and also ALEPH tuned JETSET Monte Carlo simulations.

9.3 Outlook

The work presented in this analysis is inclusive production measurement of D^{*0} from the dominant decay channel $D^{*0} \rightarrow D^0\pi^0$. By applying various machine learning algorithms, the other channel, $D^{*0} \rightarrow D^0\gamma$, might be analysed with different and more variables on training in order to observe improvements on signal significance and stability in the fitting procedure are whether or not possible.

REFERENCES

[1] S. Weinberg (1967). A Model of Leptons, *Phys. Rev. Lett.* **19**, 1264.

[2] A. Salam (1969). *Elementary Particle Theory.*

[3] S.L. Glashow et al. (1970). Weak Interactions with Lepton-Hadron Symmetry, *Phys. Rev. Lett. D* **2** 1285.

[4] S. Eidelman et al. (2004). Review of Particle Physics, *Phys. Lett. B* V **592** 1.

[5] G.D. Lafferty et al. (1995). A compilation of inclusive particle production data in e^+e^- annihilation, *J.Phys.G.Nucl.Part.Phys*, **21** A1-A151.

[6] Statement on use of ALEPH data for long-term analyses. `https://hep-project-dphep-portal.web.cern.ch/content/aleph-preservation-policy`, 10.06.2019.

[7] M. Tanabashi et al. (2018 and 2019 update). Particle Data Group, *Phys. Rev. D* **98**, 030001.

[8] T. Sj ostrand (1986). The Lund Monte Carlo for jet fragmentation and e^+e^- physics - jetset version 6.2, *Comp. Phys. Comm.* V **39** 347.

[9] R. D. Field and R. P. Feynman (1978). A Parameterization of the properties of Quark Jets, *Nucl. Phys. B* **136** 1.

[10] T. Meyer (1982). A Monte Carlo model to produce baryons in e^+e^-, *Z. Phys. C* **12** 77.

[11] B. Andersson et al. (1983). Parton fragmentation and string dynamics, *Phys. Rep.* V **97** 31.

[12] C. D. Buchanan and S. B. Chun (1987). Simple predictive model for flavor production in hadronization, *Phys. Rev. Lett.* **59**, 1997.

[13] Yu. L. Dokshitzer, V. A. Khoze, S. I. Troyan, Sov. J. (1988). *Nucl. Phys.* **47** 1384.

[14] Official web site of the CERN, `http://www.cern.ch`, 10.06.2019.

[15] M. Banner et al. (1983), Inclusive charged particle production at the CERN $p\overline{p}$ collider, *Physics Letters B* V **122** 322.

[16] P. Bagnaia et al. (1983), Evidence for $Z^0 \to e^+e^-$ ant the CERN $p\overline{p}$ collider, *Physics Letters B* V **129** 130.

[17] D. Buskulic et al. (ALEPH Collab.) (1995), Inclusive $\pi^{\pm}$, $K^{\pm}$ and $p\overline{p}$ differential cross-sections at the Z resonance, *Z. Phys. C* **66** 355.

[18] D. Decamp et al., (ALEPH Collab.) (1990), ALEPH: A detector for electron-positron annihilations at LEP, *Nucl. Instr. Meth.* A **294** 121.

[19] D. Buskulic et al., (ALEPH Collab.) (1995), Performance of the ALEPH Detector at LEP, *Nucl. Instr. Meth.* A **360** 481.

[20] D. Schlatter (1996), ALEPH in Numbers, *ALEPH reports.*

[21] J. Knobloch and P. Norton, (ALEPH Collab.) (1996), Status of Reconstruction Algorithms for ALEPH, *Draft ALEPH notes.*

[22] D. Buskulic et al. (ALEPH collab.) (1996), First measurement of the quark-to-photon fragmentation function, *Z. Phys. C* **69**, 365-377.

[23] S. Schael (ALEPH Collab.) (1996), Identification of low energetic converted photons in ALEPH, *ALEPH note* 94-104 *SOFTWE* 94-008.

[24] A. Bencheikh, S. Schael (ALEPH Collab.) (1996), B^* production in Z^0 decays, *ALEPH note* 94-105 *PHYSIC* 94-090.

[25] D. Buskulic et al. (ALEPH Collab.) (1995), Inclusive π^0 results, *Contribution to the 1995 International Europhysics Conference on High Energy Physics, Brussels, Belgium,* 27/7 - 2/8.

[26] T. Sjöstrand (1994), High-energy-physics event generation with PYTHIA 5.7 and JETSET 7.4 *Comp. Phys. Com.* V **82**, 74-89.

[27] T. Sjöstrand, ALEPH and OPAL Tuning of generators and models, `http://www.physics.carleton.ca/~ryh/opaltune/opal.html`, 10.06.2019.

[28] T. Sjöstrand, et al. (2006). PYTHIA physics and manual *J. High Energy Phys.* **026**.

[29] G. Corcella, (2001) HERWIG, *JHEP* **0101** 010.

[30] CERN Program Library (2001), *long writeup* W **5013**.

[31] D. Buskulic et al. (ALEPH collab.) (1996), Inclusive production of neutral vector mesons in hadronic Z decays, *Z. Phys. C* **69**, 379-392.

[32] D. Parker. (ALEPH Collab.) (1991), A study of Hadronic Events and the Measurement of α_s at the Z^0 Resonance. *PhD Thesis, University of Sheffield, UK.*

[33] Ahmet Bingül (2012), A non-iterative method for constraining masses in particle decays, *Nuclear Instruments and Methods in Physics Research Section A: Accelerators, Spectrometers, Detectors and Associated Equipment,* V **693(11-15)**, 0168-9002.

[34] Hocker et all, (2007) TMVA - Toolkit for Multivariate Data Analysis with ROOT, *CERN, Geneva*, **135**.

[35] ROOT Reference guide, TMVA::MethodBDT Class Reference, `https://root.cern/doc/v610/classTMVA_1_1MethodBDT.html`, 10.06.2019.

APPENDIX A

D^0, π^0 INVARIANT MASS WINDOW FOR ALL x_E INTERVALS BEFORE TMVA CUT

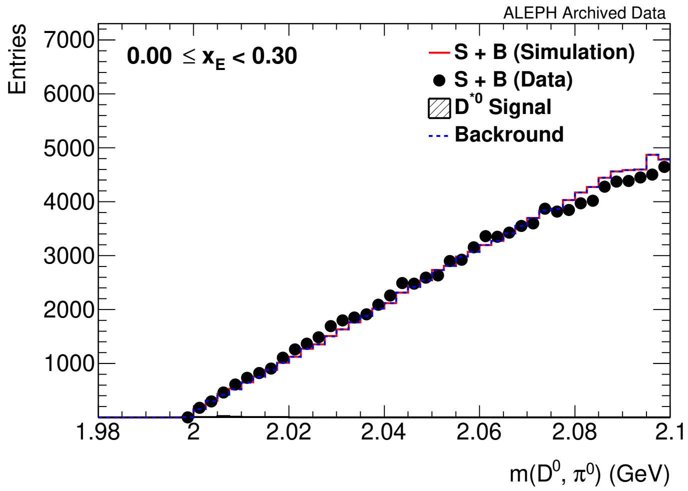

Figure A.1 Invariant mass of D^0, π^0 for the interval 0.

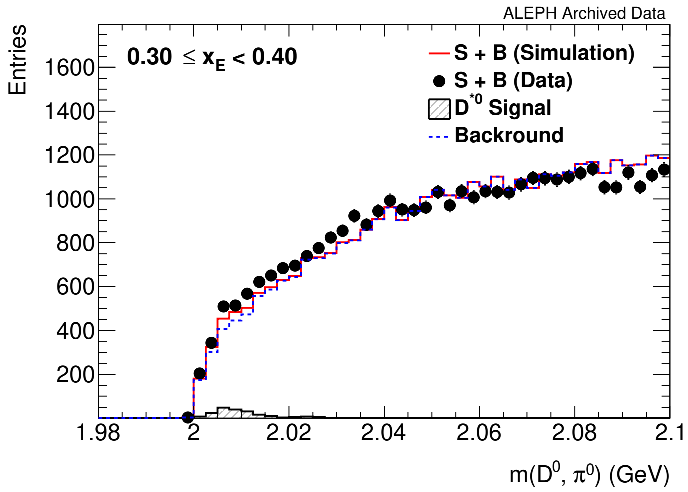

Figure A.2 Invariant mass of D^0, π^0 for the interval 1.

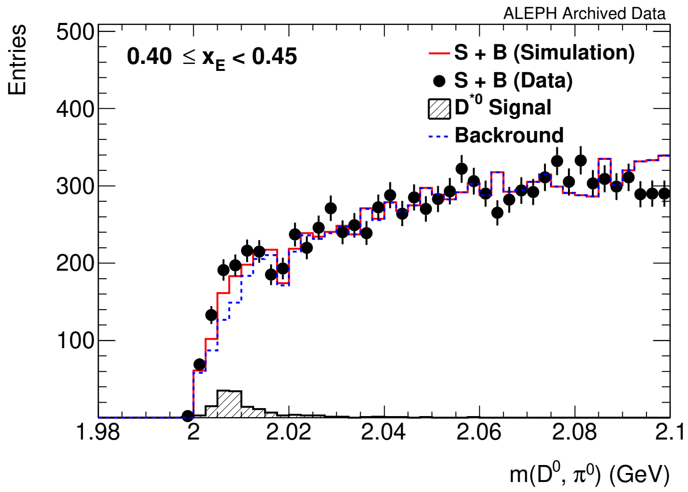

Figure A.3 Invariant mass of D^0, π^0 for the interval 2.

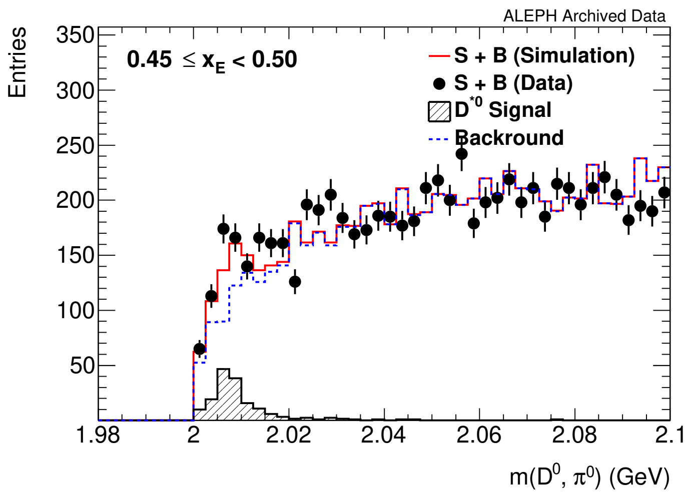

Figure A.4 Invariant mass of D^0, π^0 for the interval 3.

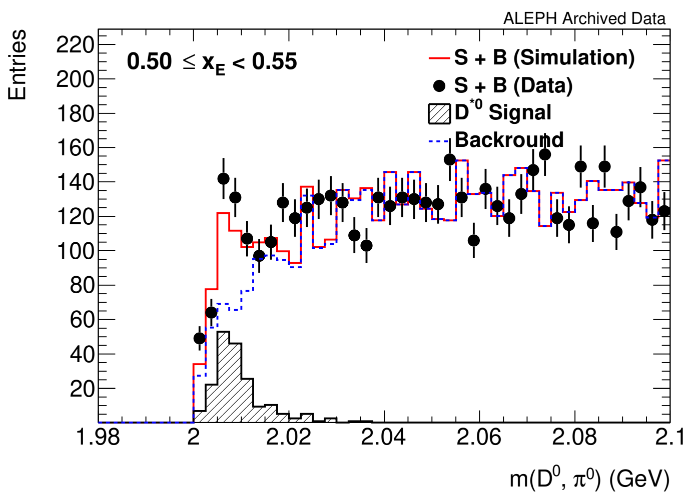

Figure A.5 Invariant mass of D^0, π^0 for the interval 4.

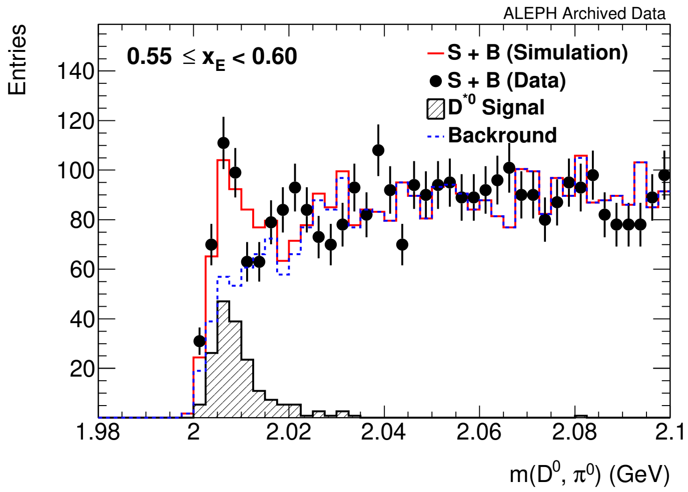

Figure A.6 Invariant mass of D^0, π^0 for the interval 5.

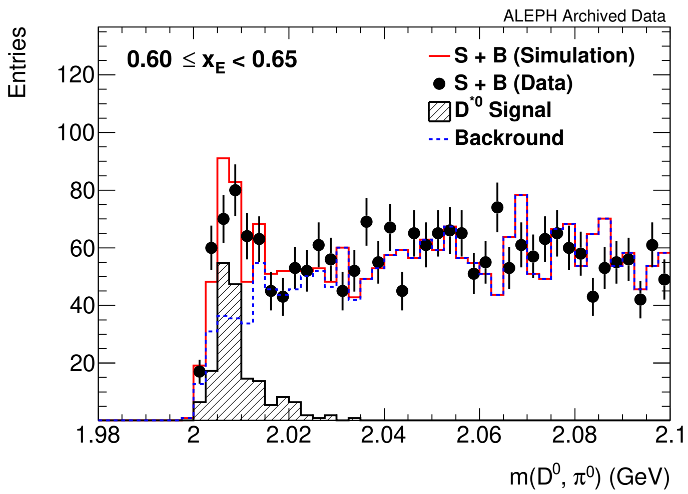

Figure A.7 Invariant mass of D^0, π^0 for the interval 6.

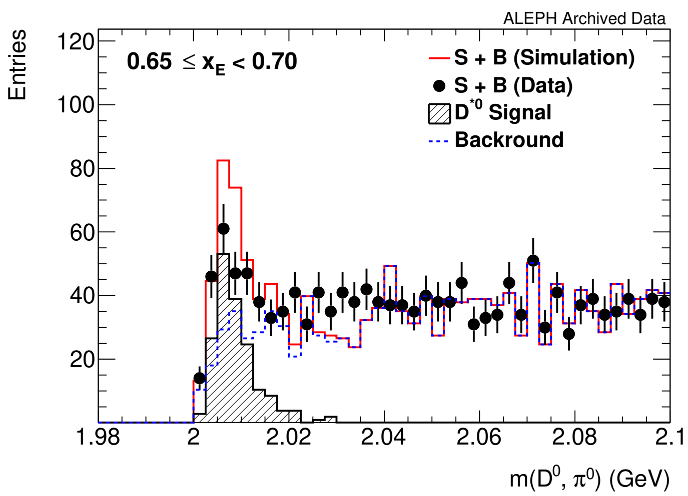

Figure A.8 Invariant mass of D^0, π^0 for the interval 7.

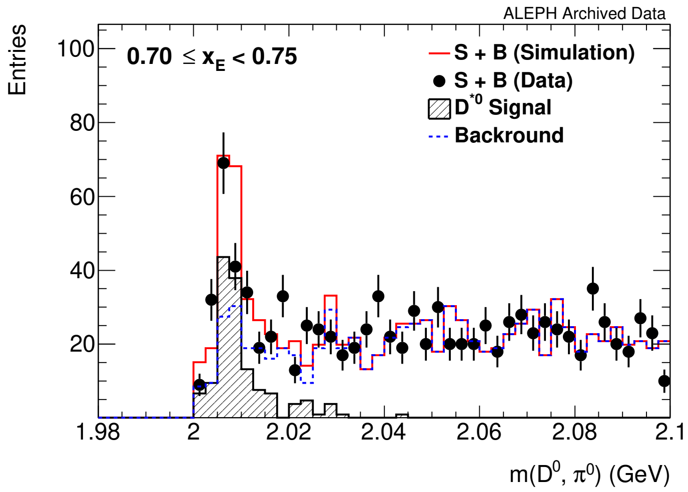

Figure A.9 Invariant mass of D^0, π^0 for the interval 8.

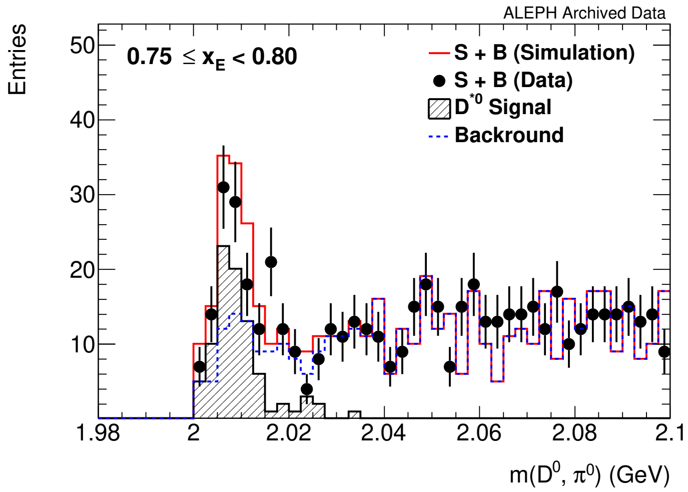

Figure A.10 Invariant mass of D^0, π^0 for the interval 9.

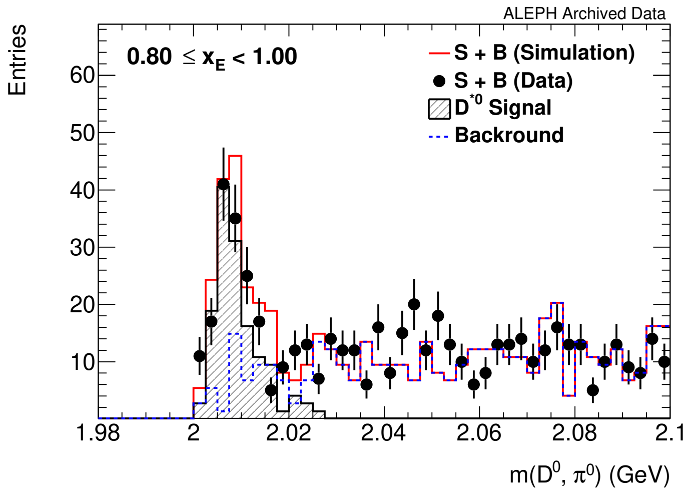

Figure A.11 Invariant mass of D^0, π^0 for the interval 10.

APPENDIX B

D^0, π^0 INVARIANT MASS WINDOW FOR ALL x_E INTERVALS AFTER TMVA CUT

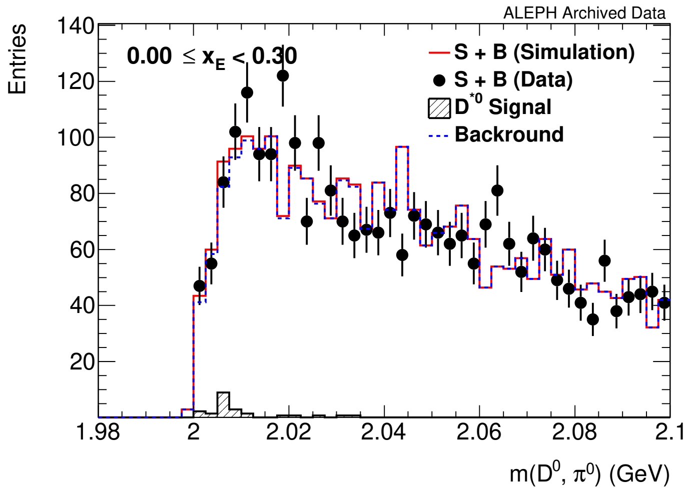

Figure B.1 Invariant mass of D^0, π^0 for the interval 0.

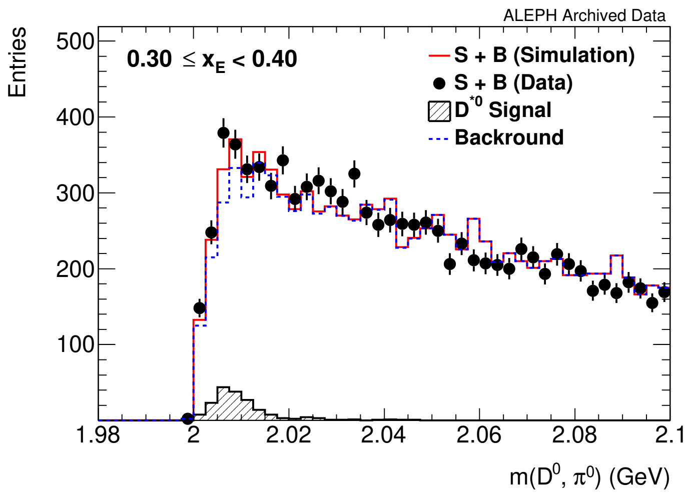

Figure B.2 Invariant mass of D^0, π^0 for the interval 1.

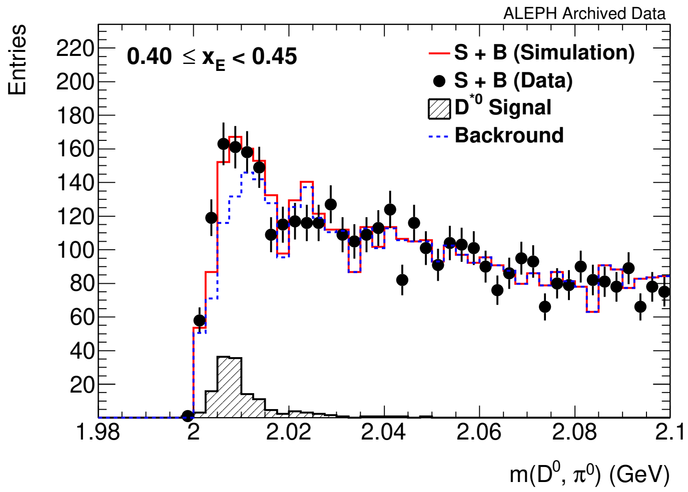

Figure B.3 Invariant mass of D^0, π^0 for the interval 2.

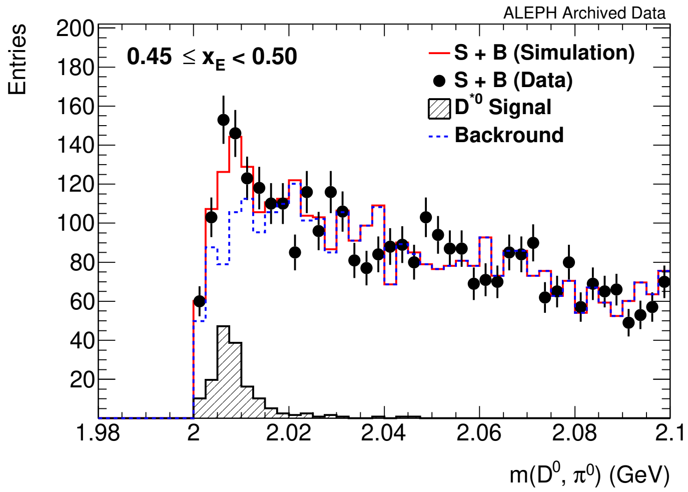

Figure B.4 Invariant mass of D^0, π^0 for the interval 3.

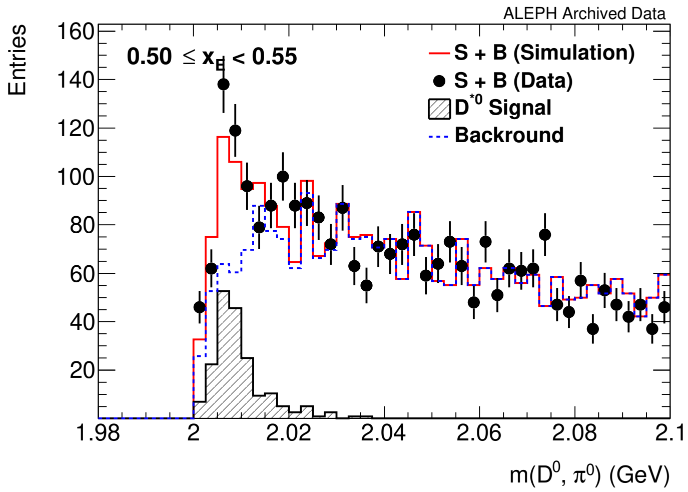

Figure B.5 Invariant mass of D^0, π^0 for the interval 4.

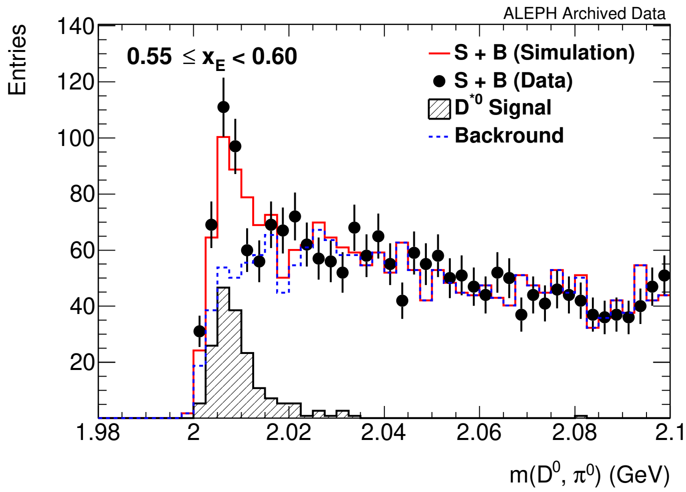

Figure B.6 Invariant mass of D^0, π^0 for the interval 5.

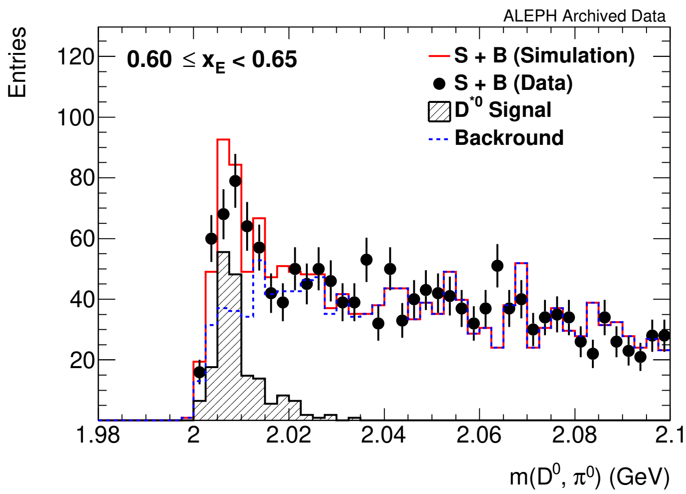

Figure B.7 Invariant mass of D^0, π^0 for the interval 6.

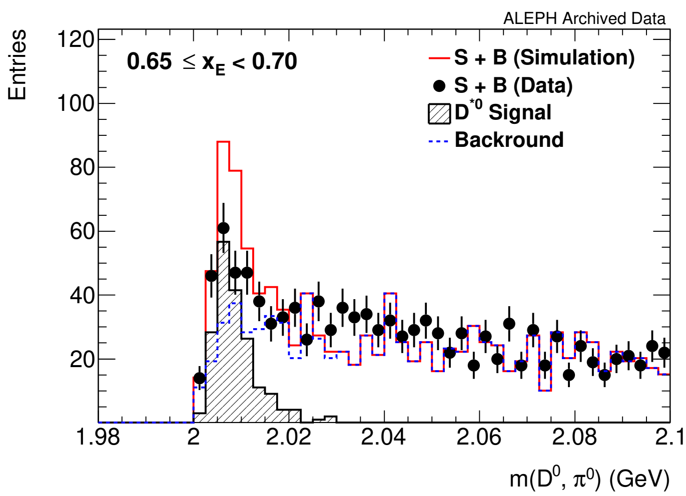

Figure B.8 Invariant mass of D^0, π^0 for the interval 7.

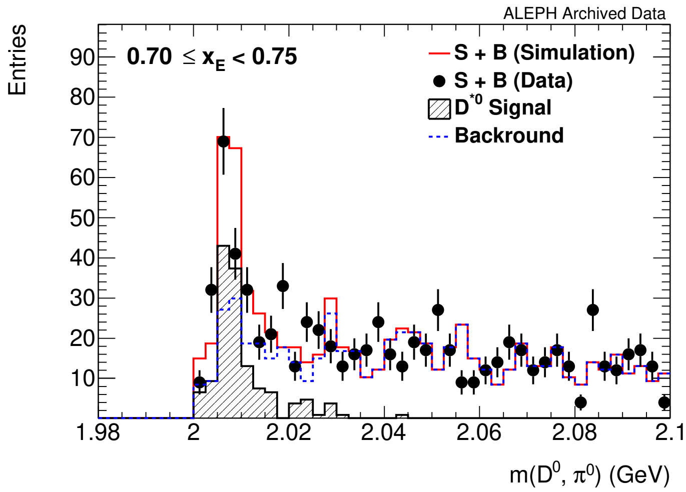

Figure B.9 Invariant mass of D^0, π^0 for the interval 8.

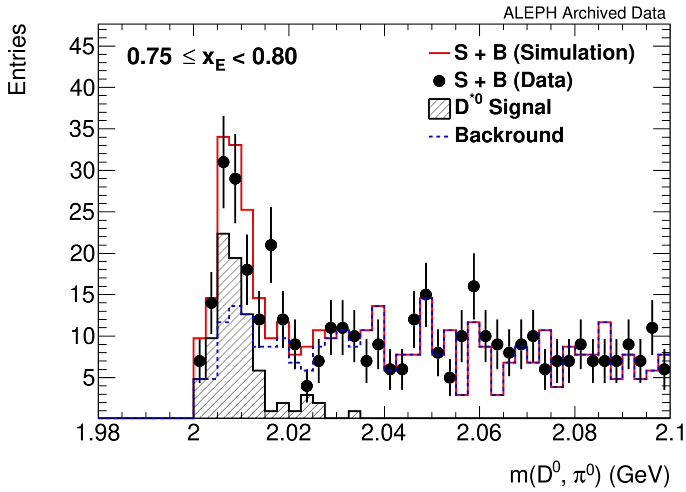

Figure B.10 Invariant mass of D^0, π^0 for the interval 9.

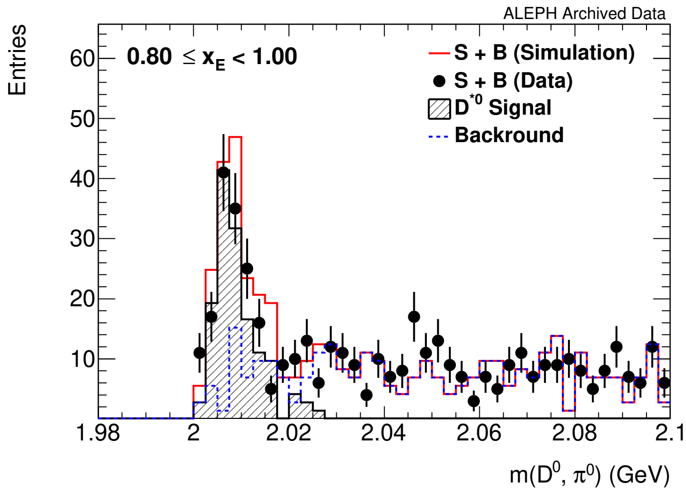

Figure B.11 Invariant mass of D^0, π^0 for the interval 10.

APPENDIX C

FIT RESULTS OF D^0, π^0 INVARIANT MASS FOR ALL x_E INTERVALS ON RECORDED DATA

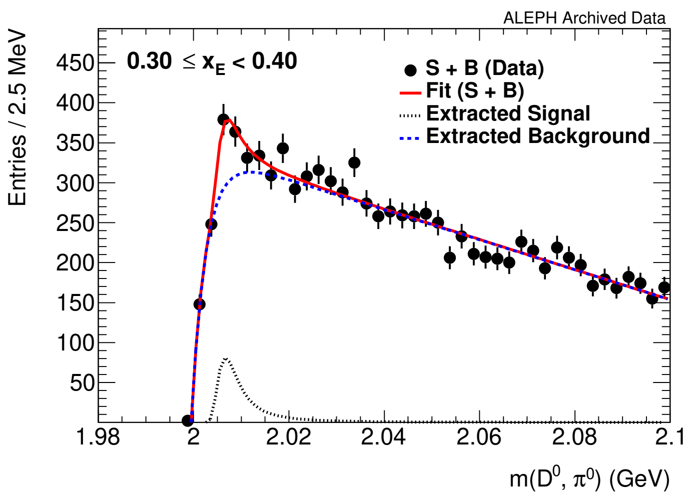

Figure C.1 Fit result for the interval 1.

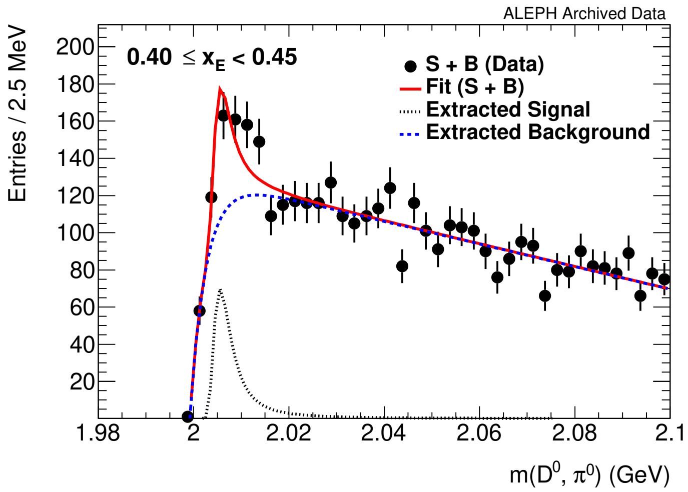

Figure C.2 Fit result for the interval 2.

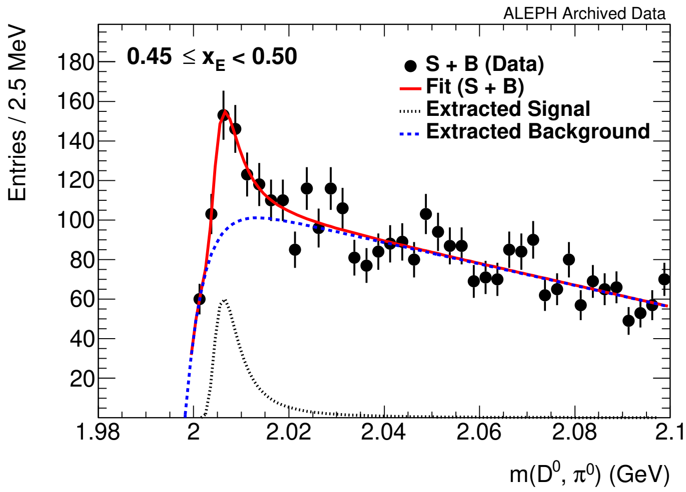

Figure C.3 Fit result for the interval 3.

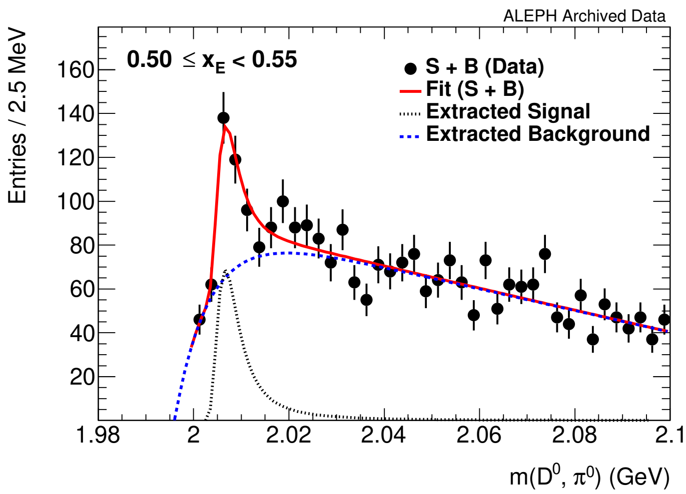

Figure C.4 Fit result for the interval 4.

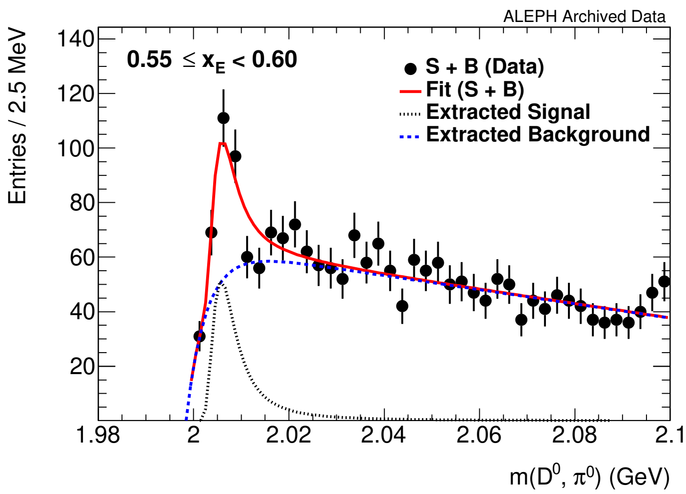

Figure C.5 Fit result for the interval 5.

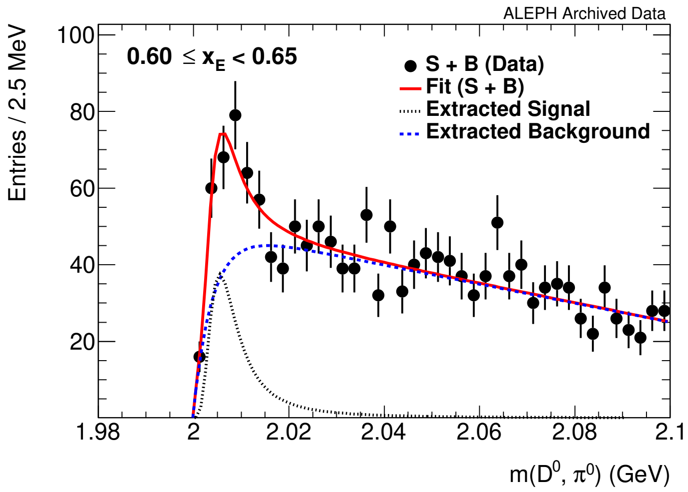

Figure C.6 Fit result for the interval 6.

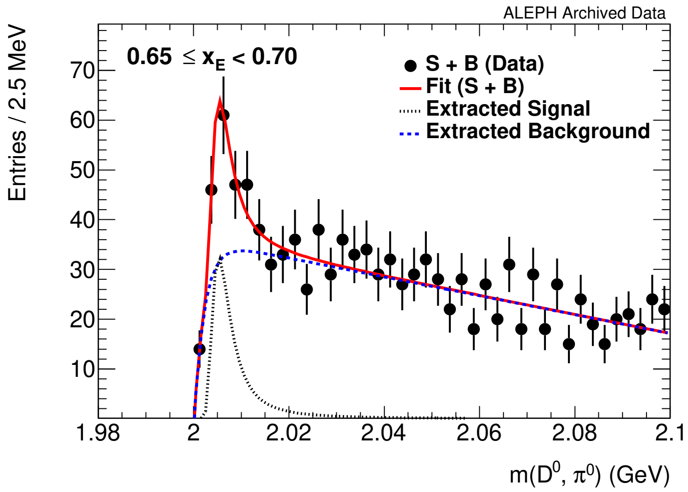

Figure C.7 Fit result for the interval 7.

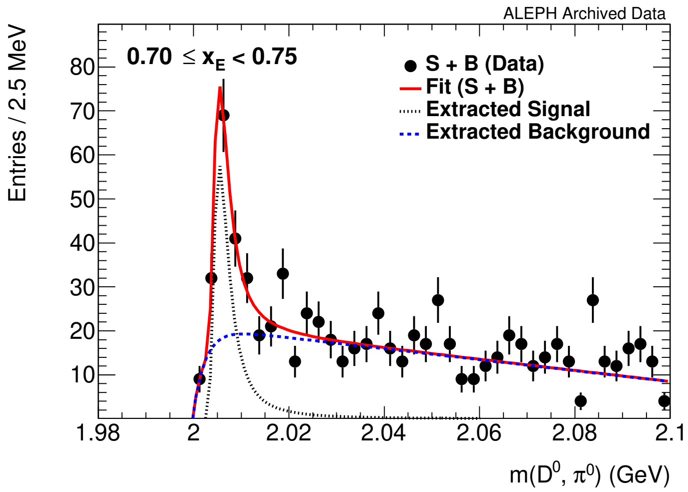

Figure C.8 Fit result for the interval 8.

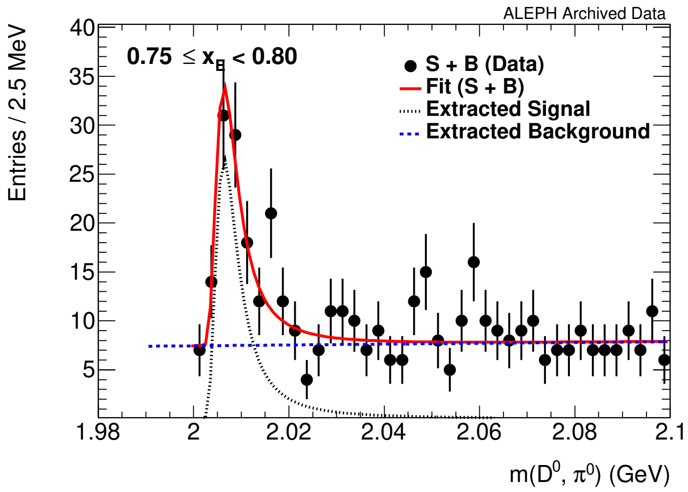

Figure C.9 Fit result for the interval 9.

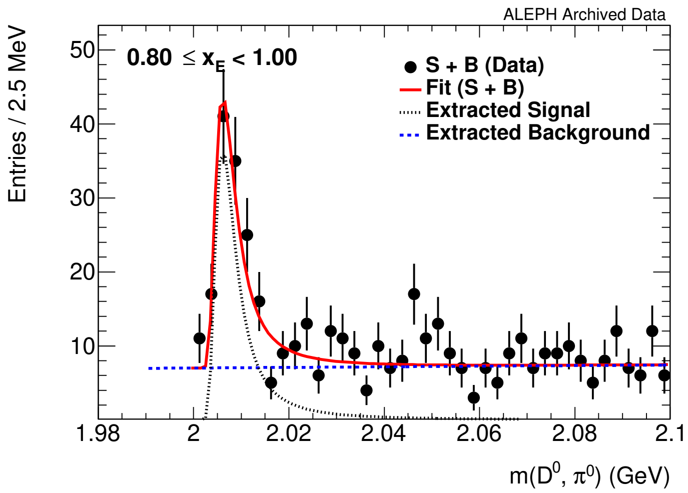

Figure C.10 Fit result for the interval 10.

PUBLICATIONS

(1) A. Bingül, U. Şaşmaz, A.J. Beddall (2018). A Ranking Method for Selection of η Mesons in High Multiplicity Events, *Acta Phys. Pol. B*, **49**, 727.

(2) U. Şaşmaz (2017). A Ranking Method for Selection of η mesons, *International Congress of Turkish Physics Society (TFD)* **33**.

CURRICULUM VITAE

Personal Information

Name: Uygar Şaşmaz

Email: uygar.sasmaz@gantep.edu.tr

Occupation

(2014 - 2020) Member of CERN (European nuclear research center) as a scientific researcher.

(2012 - 2020) Teaching and laboratory experience on computational programming and numerical methods lectures.

Education

(2015) M.Sc. degree in Engineering Physics, High Energy and Plasma Physics in Gaziantep University.

(2012) B.Sc. degree in Engineering Physics in Gaziantep University.

(2012) Bachelor degree in Business Administrations in Anadolu University.

Publications

(2018) A. Bingül, U. Şaşmaz, A.J. Beddall (2018). A Ranking Method for Selection of η Mesons in High Multiplicity Events, *Acta Phys. Pol. B*, **49**, 727.

(2017) U. Şaşmaz (2017). Ranking Method for Selection of η mesons, *International Congress of Turkish Physics Society (TFD)* **33**.

Language

English Fluent (C2)

German Elementary (A1)